MIT Libraries | DSpace@MIT

MIT Open Access Articles

Mixed ionic-electronic conducting (MIEC) membranes for thermochemical reduction of CO2: A review

Massachusetts Institute of Technology

Mixed ionic-electronic conducting (MIEC) membranes for thermochemical reduction of CO_2: A review

Xiao-Yu Wu [†] and Ahmed F. Ghoniem

Department of Mechanical Engineering, Massachusetts Institute of Technology, 77 Massachusetts Avenue, Cambridge, MA 02139, USA
† Email address: xywu@mit.edu

Abstract

Intermediate temperature membrane-supported CO_2 thermochemical reduction using renewable energy is a clean approach for reusing CO_2. To implement this technology at scale, stable catalytic membrane materials with fast kinetics should be developed, and reactor designs and system integrations should be optimized. In this review, we highlight major advancements in experimental and numerical efforts on mixed ionic-electronic conducting (MIEC) membrane-supported CO_2 thermochemical reduction, and discuss the connection among materials, kinetics, membranes and reactor design. First, we discuss the thermodynamics and kinetics of CO_2 reduction and the working principles of membrane reactors. Two methods are compared: chemical looping (redox) and membrane supported CO_2 reduction. Next, we compare CO_2 conversion rates on various membrane materials and their stability. Strontium based perovskites, e.g., Nb_2O_5-doped $SrCo_{0.8}Fe_{0.2}O_{3-\delta}$ (SCoF-82) show the highest CO_2 reduction rates so far, but they suffer degradation mainly from carbonate formation. Mixed-phase membranes are promising, with high reduction rates and good stability. Surface modification can enhance the reduction rates and increase membrane stabilities. In order to accelerate the development in materials and membranes, kinetic parameters, e.g., conductivity and reaction rate constants should be obtained from high throughput benchtop reactors complemented by reduced physical models. The mechanisms and transport models for surface kinetics and bulk diffusion are summarized. Using these results, changes in membrane morphology and surface chemistry are proposed. Finally, we summarize methods and system-scaled analysis to integrate this membrane technology with renewable or waste heat sources for fuel production and energy storage.

Keywords: CO_2 reduction; oxygen permeable; membrane reactor; process intensification; solar-fuel

Contents

Acronyms and Nomenclature

Latin letters

A	Pre-exponential factor, [unit varies]; or area, [m^2]
b	Temperature exponent for Arrhenius reaction rate equation, [dimensionless]
C	Concentration, [mol cm^{-3}]
$C_{receiver}$	Solar concentration level of a receiver, [dimensionless]
$D_{AB,e}$	Effective diffusivity between gas species A and B, [cm^2 s^{-1}]
D_V	Oxygen vacancy diffusivity, [m^2 s^{-1}]
$\dot{E}$	Energy input, [W]
E_a	Activation energy, [J mol^{-1}]
F	Faraday constant, [96485 s A mol^{-1}]
G	Gibbs free energy, [J mol^{-1}]
h_m	Mass transfer coefficient, [m s^{-1}]
H_i^o	Enthalpy at standard conditions, [J kg^{-1}]
I	Irradiation , [W m^{-2}]
J_{O2}	Oxygen flux, [mol m^{-2} s^{-1}]
k	Boltzmann constant, [1.38×10^{-23} m^2 kg s^{-2} K^{-1}]
k_r	Reaction rate constant for reaction r, [unit varies]
L	Length, [m]
$\dot{m}$	Mass flow rate, [kg s^{-1}]
n	Charged carrier density, [m^{-3}]
$\dot{n}$	Molar flow rate, [mol s^{-1}]
P	Pressure, [Pa]
q	Charge, [C]
$\dot{Q}$	Thermal energy power, [W]
r	Reaction rate, [mol cm^{-2} s^{-1}]; or radius, [m]
R	Universal gas constant, [8.314 J mol^{-1} K^{-1}]
t	Thickness, [m]
t_j	Transference number of charged species j, [dimensionless]
T	Temperature, [K]
v	Velocity, [m s^{-1}]
V_m	Molar volume, [m^3 mol^{-1}]
$\dot{W}$	Power, [W]
Z	Number of charges, [dimensionless]

Greek letters

δ	Oxygen nonstoichiometry, [dimensionless]

ε	Permitivity, [F m^{-1}]
η	Efficiency, [dimensionless]
μ	Chemical potential, [J mol^{-1}]; or mobility of charge species, [m^2 V^{-1} s^{-1}]
ρ	Charge density, [C m^{-3}]
σ	Conductivity, [S m^{-1}]; or Stefan-Boltzmann constant, [5.670367×10^{-8} kg s^{-3} K^{-4}]
φ	Electric field, [V]
ϕ	Thiele Modulus, [dimensionless]

Superscript

o	Standard condition

Subscript

Ads	Adsorbed species
b	Bulk
c	Characteristic length
f	Formation energy; or feed side
s	Surface; or sweep side

Acronym

CCS	Carbon capture and sequestration
CFD	Computational fluid dynamics
DFT	Density functional theory
DOM	Figures of merit
HHV	Higher heating value
IR	Infrared
LEIS	Low-energy ion scattering
LHV	Lower heating value
MD	Molecular dynamics
MIEC	Mixed ionic and electronic conducting
OC	Oxygen carrier
PEMEC	Proton exchange membrane electrolysis cell
POM	Partial oxidation of methane
PV	Photovoltaic
SOEC	Solid oxide electrolysis cell
TPD	Temperature programmed desorption
TPR	Temperature programmed reduction
XPS	X-ray photoelectron spectroscopy
XRD	X-ray powder diffraction

Material related symbols

ABO_3	Perovskite general chemical formula, A and B are different cations
BCoFZ	Barium iron zirconium cobalt oxide, $BaCo_xFe_yZr_{1-x-y}O_{3-\delta}$
BFZ	Barium zirconium iron oxide, $BaFe_{0.9}Zr_{0.1}O_{3-\delta}$
BCoFNb	Barium niobium iron cobalt oxide, $BaCo_xFe_yNb_{1-x-y}O_{3-\delta}$
BSCoF-5582	Barium strontium iron cobalt oxide, $Ba_{0.5}Sr_{0.5}Co_{0.8}Fe_{0.2}O_{3-\delta}$
CGO	Gadolinium-doped ceria, $Ce_{1-x}Gd_xO_{2-\delta}$
CZO	Zirconium-doped ceria, $Ce_{1-x}Zr_xO_{2-\delta}$
e' (or n)	Electron
GSTA	Gadolinium strontium aluminum titanium oxide, $Gd_{0.08}Sr_{0.88}Ti_{0.95}Al_{0.05}O_{3\pm\delta}$
$h^\bullet$ (or p)	Electron hole
LCaF-91	Lanthanum calcium iron oxide, $La_{0.9}Ca_{0.1}FeO_{3-\delta}$
LCuF-28	Lanthanum copper iron oxide, $LaCu_{0.2}Fe_{0.8}O_{3-\delta}$
LNO	Lanthanum nickel oxide, $LaNiO_{4+\delta}$
LSCoF-6428	Lanthanum strontium cobalt iron oxide, $La_{0.6}Sr_{0.4}Co_{0.2}Fe_{0.8}O_{3-\delta}$
LSCuF-7328	Lanthanum strontium copper iron oxide, $La_{0.7}Sr_{0.3}Cu_{0.2}Fe_{0.8}O_{3-\delta}$
LSF-37	Lanthanum strontium iron oxide, $La_{0.3}Sr_{0.7}FeO_{3-\delta}$
LSM-55	Lanthanum strontium magnesium oxide, $La_{0.5}Sr_{0.5}MnO_{3-\delta}$
LSMCo-5555	Lanthanum strontium magnesium cobalt oxide, $La_{0.5}Sr_{0.5}Mn_{0.5}Co_{0.5}O_{3-\delta}$
MeO_x	Metal oxide
$O_O^\times$	Lattice oxygen
PLNCG	Praseodymium lanthanum gadolinium copper nickel oxide, $(Pr_{0.9}La_{0.1})_2(Ni_{0.74}Cu_{0.21}Ga_{0.05})O_{4+\delta}$
SBFMo-7391	Strontium barium molybdenum iron oxide, $Sr_{0.7}Ba_{0.3}Fe_{0.9}Mo_{0.1}O_{3-\delta}$
SCoF-82	Strontium iron cobalt oxide, $SrCo_{0.8}Fe_{0.2}O_3$
SCoFNb	Nb_2O_5 doped SCoF-82
SCoFZ-451	Strontium iron zirconium cobalt oxide, $SrCo_{0.4}Fe_{0.5}Zr_{0.1}O_{3-\delta}$
SDC	samarium-doped ceria, $Sm_{1-x}Ce_xO_{2-\delta}$
SFC2	Strontium iron cobalt oxide, $SrFeCo_{0.5}O_{3-\delta}$
$V_O^{\bullet\bullet}$	Oxygen vacancy
YSZ	Yttria-stabilized zirconia, ZrO_2/Y_2O_3

1. Introduction

The global temperature has been rising over the past few decades, and 2015 – 2017 have been the hottest years on record [1]. Even though global energy-related CO_2 emissions have leveled off for three years, 2014 – 2016, the annual emission in 2017 increased by 1.4%, reaching 32.5 gigatonnes, [2] with the global average atmospheric CO_2 concentration climbing above 408 ppm [3]. To counter these trends, the first universal climate agreement was adopted by 195 countries in the 2015 Paris Climate Conference [4]. Concerted efforts from various countries and sectors are being focused on keeping global warming well below 2°C compared with pre-industrial levels (e.g., China [5] and European Union [6, 7]). CO_2 capture and utilization, e.g., converting CO_2 to value-added chemicals such as CO, urea, salicylic acid and polyurethanes, has environmental and economic benefits and can accelerate the transition to low-carbon economy [8-12].

Carbon dioxide is a very stable molecule; the average C=O bond energy is 805 kJ mol^{-1} [13]. The dissociation of CO_2 is highly endothermic:

$$CO_2 \rightarrow CO + \frac{1}{2}O_2 \qquad \Delta H^o_{298K} = 282.9 \text{ kJ/mol} \qquad (1)$$

$$CO_2 \rightarrow C + O_2 \qquad \Delta H^o_{298K} = 393.5 \text{ kJ/mol} \qquad (2)$$
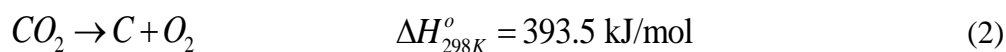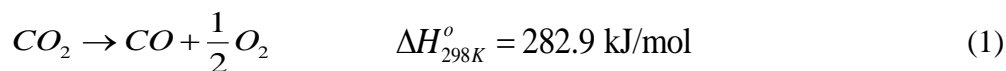
If intermittent renewable energy sources are used for CO_2 reduction to CO and C, the process can be viewed as an energy storage technology. There are four promising methods for doing that: electrochemical, photochemical, thermochemical and biochemical, shown schematically in Figure 1 and Table 1. They are categorized by the energy to activate the CO_2 reduction, i.e., electricity, photon, thermal energy and biology cultivation, respectively. Combinations of any two of these technologies have also been proposed, such as photo-electro-chemical (PEC) [14], photo-bioreactor [15] and electro-bioreactor [16]. These have all been demonstrated at lab-scale, but breakthroughs such as efficiency improvement and cost reduction are required before large-scale application becomes possible. Examining the kinetic and transport phenomena in these processes can reveal the rate-limiting steps and guide the design and optimization of materials, reactors and systems. It is important to develop frameworks of extracting valuable information such as reaction rate constants from high throughput benchtop setups and building physical models to simulate the processes.

Here we review the process of CO_2 thermochemical reduction to CO, which has drawn much attention in recent years thanks to the interest of solar fuel production for storage of renewable energy and reusing CO_2. We focus on the membrane-supported CO_2 reduction and discuss the kinetics and transport models to describe processes. Readers who are interested in other CO_2-to-chemical technologies in Figure 1 can find relevant reviews in Table 1.

Table 1 Summary of CO_2 reduction technologies

	Electrochemical	Photochemical	Thermochemical	Biochemical
Energy input	Electricity	Photon	Heat	Solar radiation, cultivation
Products	CO, formate, C_2, etc.[17]	CO, CH_4, etc.	CO, CH_4	Microalgae, etc.
Operating Temperature	PEMEC: 20 – 90ºC SOEC: 500 – 1000ºC	~25ºC	500 - 1000ºC	~25ºC
Recent reviews	[17], [18]	[19], [20]	[21], [22]	[15], [23]
Challenges (summarized from [24])	1. High overpotential due to non-optimal catalysts and cell structure, low selectivity towards desired product and instability of materials; 2. Low Faradaic efficiencies and high energy consumption; 3. Expensive catalysts.	1. Low product selectivity; 2. Low photon efficiency, (efficiency improvement of at least 3 orders of magnitude is required [25]); 3. Expensive catalysts.	1. Little understanding of oxygen transport, surface chemistry, morphology, structural and chemical changes under cycles at high temperatures; 2. High thermal losses; 3. High initial cost of high-temperature reactor and solar concentrator.	1. Little understanding of the dependence of microalgae growth on factors such as mixing, gas exchange, mass transfer, water quality; 2. High consumption of water and fertilizer; 3. Expensive cultivation and harvesting cost.
PEMEC: proton exchange membrane electrolysis cell SOEC: solid oxide electrolysis cell				

Figure 1 Schematic of four CO_2 reduction technologies: (a) electrochemical, using electricity in an electrolyzer; (b) photochemical, using photons in a photochemical reactor; (c) thermochemical, using heat; and, (d) biochemical CO_2 reduction. For the first three technologies, CO_2 reduction to CO is used as an example. The thicknesses of different layers are not to the scale.

Oxygen permeable membrane supported CO_2 thermochemical reduction was proposed in 1980s as a clean way to utilize renewable or waste heat to produce useful chemicals [26]. Membranes operate in the temperature range of 700-1000ºC with oxygen fluxes in the orders of $0.01 – 10$ µmol cm^{-2} s^{-1} [22]. By incorporating a perm-selective membrane in the CO_2 reduction process, thermodynamics equilibrium on the feed side can be shifted by separating one of the products, that's oxygen, and hence, lowering the temperature required to achieve similar yields as that achieved by direct thermolysis in the pure gas phase operation at temperatures in the range 1200-2000ºC. Oxygen permeation is driven by its partial pressure gradient across the membrane (or its chemical potential in the general case). In order to maintain low oxygen partial pressure on the sweep side, different methods can be applied as shown in Figure 2(a): (1) using inert gas to sweep away the produced oxygen; (2) using vacuum to maintain a low total pressure; (3) using fuels to consume oxygen by full or partial oxidation. CO_2 reduction on the feed side is impacted by

the oxygen partial pressure gradient, as shown in Figure 2(b). Different applications have been proposed in which CO_2 reduction in an oxygen permeable membrane is integrated with other synergistic processes. One option is using renewable energy to convert CO_2 in the combustion products of fossil fuel power plants back into fuels, which is schematically shown in Figure 2(c).

In this review, we first discuss the thermodynamics and kinetics of CO_2 thermolysis in the gas phase or using metal oxides at elevated temperatures. We compare two thermochemical CO_2 reduction technologies: chemical looping (redox) and membrane-supported CO_2 reduction. Next, we focus on the latter technology, and summarize membrane materials, categorized into single phase (fluorite or perovskite) and mixed phase materials. Material synthesis, membrane fabrication and surface modifications are discussed as they can impact conversion rates and stability. Kinetics including charged species diffusion, reaction mechanisms and rate constants are reviewed. System integration for solar-fuel production, and system analysis are summarized. In order to accelerate technology development, attention should be focused on extracting material and membrane characteristics, e.g., surface reaction rates and bulk diffusivity, from high throughput experiments and physical models. The selection of transport models will also be discussed, which depends on the operating conditions and the rate-limiting steps.
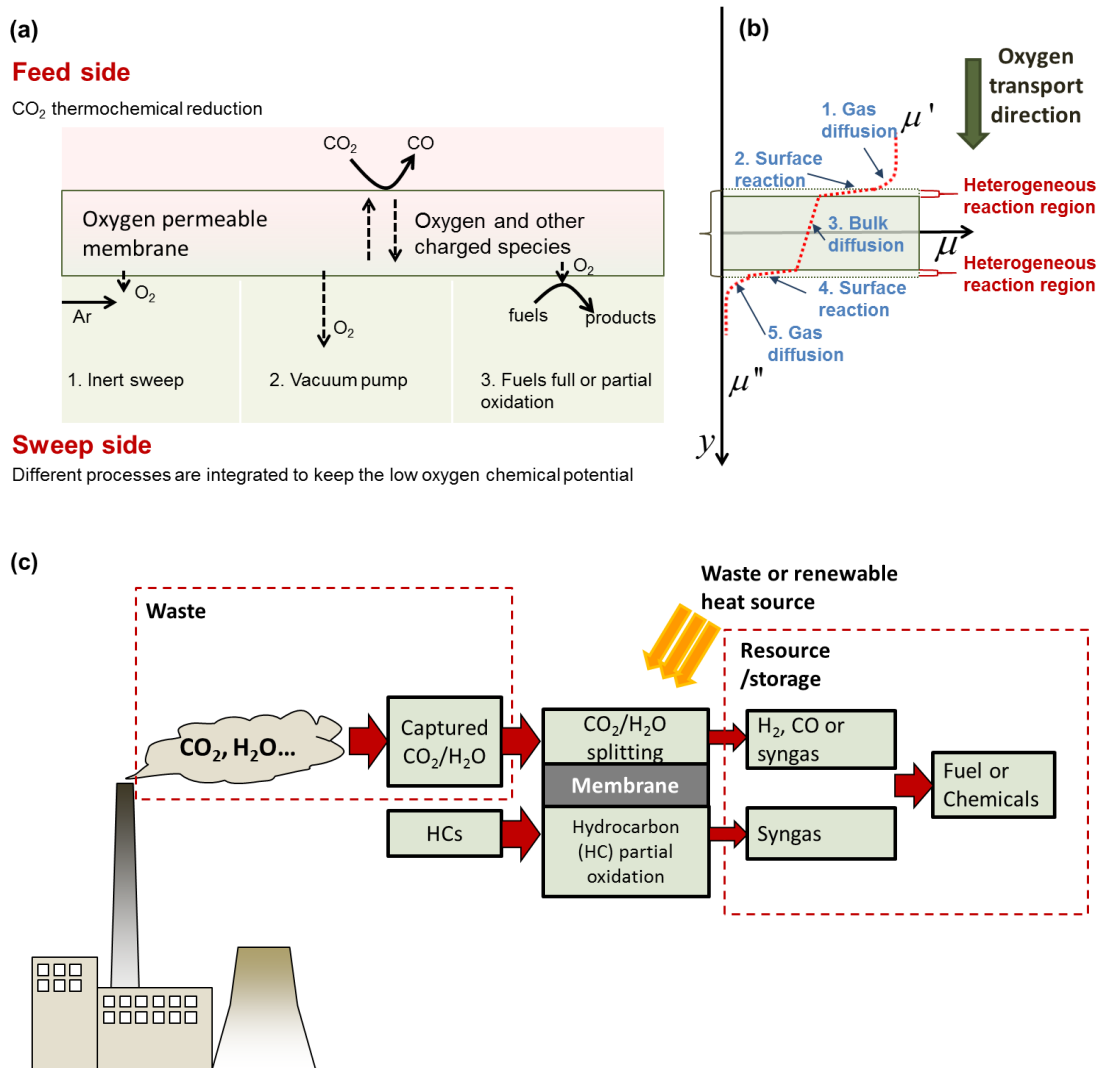
Figure 2 (a) A schematic diagram showing the different processes in an oxygen permeable membrane reactor with CO_2 thermochemical reduction on the feed side and various processes on the sweep side to maintain the low oxygen chemical potential; (b) The five steps of oxygen permeation in the membrane supported CO_2 reduction process. The feed and sweep sides have high and low chemical potential, μ' and μ'', respectively. The thickness of the heterogeneous reaction regions on either side of the membrane is not to the scale. (c) Flow diagram of capturing and reusing combustion products from a fossil fuel power plant for CO_2 to value-added chemicals

2. Working principles and thermochemical reduction methods

2.1 Thermodynamics of CO_2 dissociation

Homogeneous gas-phase CO_2 thermal dissociation, or thermolysis, operates at temperatures much higher than 1200°C, constrained by thermodynamic equilibrium [27]. Figure 3 shows the gas composition at equilibrium at 1 bar. CO_2 conversion yield is as low as 0.1% - 0.2% at 1300 - 1400°C. Even at 2000°C, the CO_2 conversion is as low as 5%.

Heat at these temperatures could be supplied by concentrated solar field with high concentration ratios (parabolic, tower or dish collectors) [28]. Traynor and Jensen [29] proposed a prototype of direct solar CO_2 reduction, without product separation, followed by fast quenching to reduce or avoid product recombination, as shown in Figure 4. The solar-to-fuel efficiency, defined as,

$$\eta_{solar-fuel} = \frac{\sum\left(\dot{m}_{products}H^o_{products}\right) - \sum\left(\dot{m}_{reactants}H^o_{reactants}\right)}{\dot{E}_{solar}} \quad (3)$$

was as low as 5%, where $\dot{m}_i$ is the mass flow, [kg s^{-1}], H^o_i is the enthalpy at standard condition, [J kg^{-1}], and $\dot{E}$ is the solar energy input, [W]. While the measured efficiency was low, an ideal system can operate with values as high as 20% [29]. The lower efficiency could be due to product recombination and lower CO production in the reaction zone of 2350°C (12% instead of the ideal 19%), showing the thermodynamics and kinetics limitations of the splitting process. Moreover, heat loss and performance degradation are among the major concerns of high temperature concentrated solar plants. And the cost of the solar concentrator increases with the operating temperature and solar concentration ratio [28].
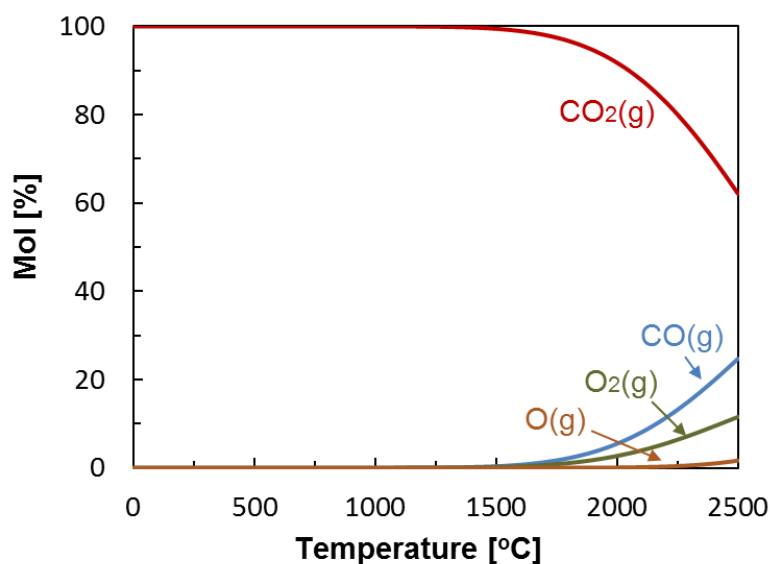
Figure 3 Plot of mole fractions of relevant species versus temperature for CO_2 thermolysis in gas phase at thermodynamic equilibrium at 1 bar (calculated used Cantera [30] and GRI-Mech 3.0 [31])
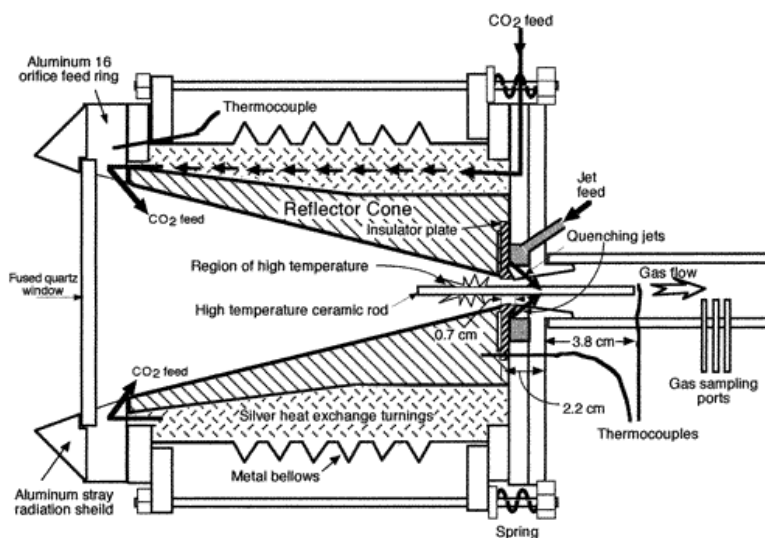
Figure 4 Schematic of the reactor: CO_2 thermolysis with solar input (Reprinted from [29] with permission of the American Chemical Society)

Regarding the kinetics, three reversible reactions were proposed for modeling CO_2 gas-phase thermolysis reactions [32]:

$$CO_2 + M \leftrightarrow CO + O + M \qquad \text{(R1)}$$

$$CO_2 + O \leftrightarrow CO + O_2 \qquad \text{(R2)}$$

$$O_2 + M \leftrightarrow O + O + M \tag{R3}$$
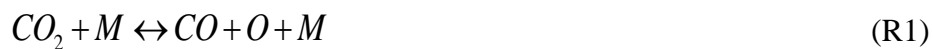
Here M is a third body. The reaction rate constant is expressed in the usual Arrhenius form:

$$k_i = AT^b \exp\left(-E_a / RT\right) \tag{4}$$

where A is the pre-exponential factor, [unit varies], b is the temperature exponent, [dimensionless], E_a is the activation energy, [J mol^{-1}], R is universal gas constant, [8.314 J mol^{-1} K^{-1}], and T is the temperature, [K]. The activation energy of the forward reactions are high (shown in Table 2), and the system can be limited by kinetics [29].

Table 2 Kinetic parameters for the CO_2 thermolysis steps (Reprinted with permission from [32]. Copyright (2004) American Chemical Society.)

Reaction	A	b	E_a/R
R1 forward	6.445×10^{10} m^3 mol^{-1} s^{-1}	0	62600 K
R1 backward	6.167×10^2 m^6 mol^{-2} s^{-1}	0	1510 K
R2 forward	1.686×10^7 m^3 mol^{-1} s^{-1}	0	26500 K
R2 backward	2.530×10^6 m^3 mol^{-1} s^{-1}	0	24000K
R3 forward	1.807×10^{12} m^3 mol^{-1} s^{-1}	-1	59380 K
R3 backward	1.886×10^1 m^6 mol^{-2} s^{-1}	0	-900 K

To overcome the equilibrium limitations in the homogeneous gas phase, methods to shift the equilibrium, prevent products recombination and accelerate the kinetics were proposed, e.g., quenching [33, 34], heat-exchanger loop [35], perm-selective membranes [33-36] and oxide catalysts [27]. Quenching and heat-exchanger loops have lower process efficiency. To accelerate the kinetics, oxide catalysts including perovskites and fluorites, such as LaFe$_{0.7}$Co$_{0.3}$O$_3$, LaFeO$_3$, Ce$_{0.75}$Zr$_{0.25}$O$_2$ and CeO$_2$, were used in fixed bed reactors [27]. For example, CO_2 reduction rates catalyzed by Ce$_{0.75}$Zr$_{0.25}$O$_2$ and CeO$_2$ (fixed bed) were higher by a factor of 1.89 and 1.57 times of the rate without catalysts at 1300°C, respectively [27]. Alternatively, CO_2 reduction can be done using the reduced metals or oxides in one reactor, while the reduction of the metal oxides is done in a different reactor. On the other hand, high-temperature perm-selective membranes can separate the products *in situ*, and hence, shift the equilibrium on the feed side. In this case, the CO_2 reduction process is done on the feed side of the membrane which oxygen is collected on the permeate side (sweep side). These last two processes are described in more detail next.

2.2 CO_2 thermochemical reduction

In the two thermochemical processes, that is chemical looping and membrane supported reduction, mentioned above and in Figure 5, CO_2 reduction occurs heterogeneously at the solid-gas interface at $700 - 1000\,^{\circ}C$, facilitated by oxygen vacancies, electron holes or electrons. In this section, we compare these two approaches (summarized in Table 3).

(a)

$$CO_2(g) + V_O^{\bullet\bullet} \leftrightarrow CO(g) + O_O^x + 2h^{\bullet}$$

Oxidation side

$CO_2 \quad CO$

Reduced oxides

Redox reactor

Oxidized oxides

Reduction side

$$2O_O^x + 4h^{\bullet} \leftrightarrow 2V_O^{\bullet\bullet} + O_2$$

O_2

(b)

Feed side

$$CO_2(g) + V_O^{\bullet\bullet} \leftrightarrow CO(g) + O_O^x + 2h^{\bullet}$$

$CO_2 \quad CO$

$V_O^{\bullet\bullet} \quad O_O^x, 2h^{\bullet}$

Oxygen permeable membrane

$V_O^{\bullet\bullet} \quad O_O^x, 2h^{\bullet}$

$$2O_O^x + 4h^{\bullet} \leftrightarrow 2V_O^{\bullet\bullet} + O_2$$

O_2

Sweep side
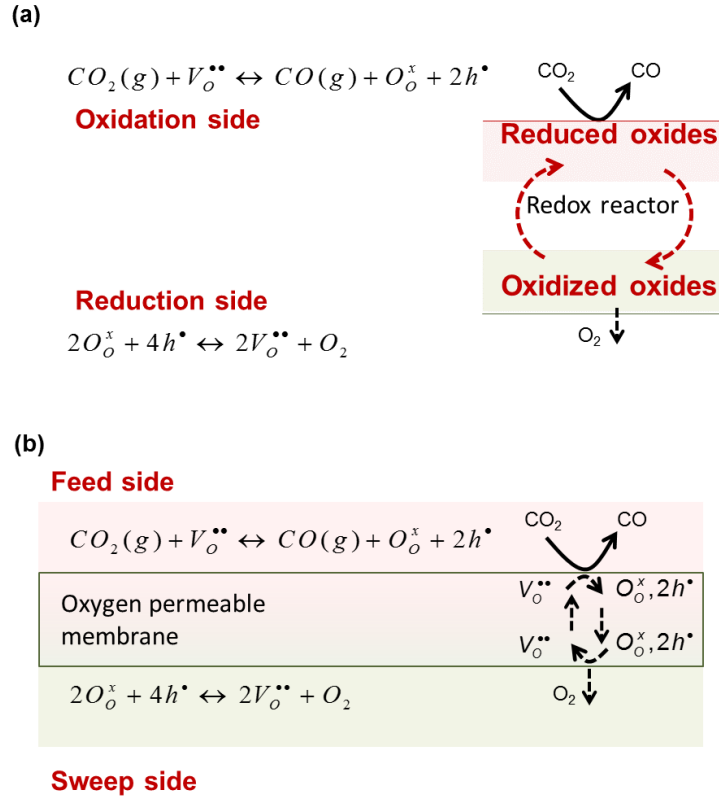
Figure 5 Schematic graphs of (a) chemical looping (redox) and (b) membrane-supported CO_2 thermochemical reduction. In both approaches, O_2 production is integrated as an example

2.2.1 Chemical looping (redox)

Redox CO_2 splitting is shown schematically in Figure 5 (a). In a typical redox cycle, the concentration of oxygen in the metal oxide increases (oxidation) or decreases (reduction) by changing the oxygen nonstoichiometry, δ, in $MeO_{x-\delta}$. In the (metal) oxidation reaction, the nonstoichiometry increases from $(x - \delta_1)$ to $(x - \delta_2)$ according to the reaction, where $\delta = 0$ corresponds to the fully oxidized metal,

Oxidation:
$$\left(\delta_1 - \delta_2\right)CO_2 + MeO_{x-\delta_1} \leftrightarrow \left(\delta_1 - \delta_2\right)CO + MeO_{x-\delta_2} \quad (5)$$
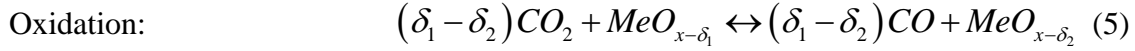
Typical values of δ is O(0.1). Metal oxidation is generally exothermic. On the other hand, metal reduction can occur either by heating the oxide or reacting with fuels, to restore the oxygen concentration to its reduction state and be ready for the oxidation reaction.

Reduction (thermal):
$$MeO_{x-\delta_2} \leftrightarrow MeO_{x-\delta_1} + \frac{\delta_1 - \delta_2}{2}O_2 \quad (6)$$

Reduction (fuel assisted):
$$MeO_{x-\delta_2} + Fuel \leftrightarrow MeO_{x-\delta_1} + Products \quad (7)$$
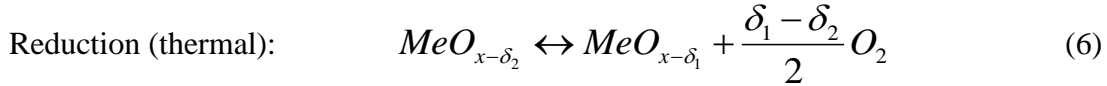
Here, $MeO_{x-\delta}$ is metal oxide with nonstoichiometry δ, also known as the oxygen carrier (OC). For the case of thermal reduction, pure ceria, $CeO_{2-\delta}$, or doped ceria, such as $Ce_{0.5}Zr_{0.5}O_{2-\delta}$ (CZO), are often used as the OC, and the operating temperatures for the oxidation and reduction reactors can be different. Chueh et al. [37] investigated CeO_2 at 800/1500 °C for oxidation/reduction, respectively; the total CO production rate was 280 μmol g^{-1} with 50% CO_2 in the oxidation gas. When using fuel to reduce the OC, the reduction temperature can be greatly reduced to be close or the same as the oxidation temperature, which reduces particle sintering and agglomeration. Venstrom et al. [38] investigated CO_2 reduction on $CeO_{2-\delta}$ using hydrogen to reduce the metal oxide; CO production was as high as 934 μmol g^{-1} with 4% CO_2 at 900°C. Lower operating temperature was achieved by doping Zr into $CeO_{2-\delta}$ [39]. Other materials such as Zn/ZnO, FeO/Fe$_3$O$_4$ [40, 41], various perovskites such as $SrFeO_{3-\delta}$ and $La_{0.6}Sr_{0.4}Cr_{1-x}Co_xO_{3-\delta}$ [42, 43], and poly-cation oxides such as (FeMgCoNi)O$_x$ ($x \approx 1.2$) [44] are also potential oxygen carrier candidates.

The Ellingham diagram has been used to determine thermodynamically favorable operating conditions when using complex oxides as oxygen carriers. Figure 6 shows the standard partial molar Gibbs free energy changes, $\Delta G_{ox}^{\prime 0}(T)$ for the oxidation reactions of $CeO_{2-\delta}$ and $La_{0.6}Sr_{0.4}Mn_{0.6}Al_{0.4}O_{3-\delta}$ at a certain δ value, and the $\Delta G_{CO}^0(T)$ for the CO oxidation reaction at the standard pressure $P^0 = 1$ bar [45]. The $\Delta G_{ox}^{\prime 0}(T)$ is defined as,

$$\Delta G_{ox}^{\prime 0}(T) = \lim_{\Delta\delta \to 0} \frac{\Delta_f G_{ABO_{3-\delta+\Delta\delta}} - \Delta_f G_{ABO_{3-\delta}}}{\Delta\delta}, \quad (8)$$

where $\Delta_f G$ is the formation Gibbs free energy. The general perovskite formula ABO$_{3-\delta}$ is used as an example:

$$\frac{1}{\Delta\delta} ABO_{3-\delta} + \frac{1}{2} O_2 = \frac{1}{\Delta\delta} ABO_{3-\delta+\Delta\delta}. \tag{9}$$

Both the enthalpy and entropy of the oxides change with oxygen non-stoichiometry, δ, and hence, $\Delta G^{\prime 0}_{ox}(T)$ of two typical δ values are shown. For the CO_2 reduction reaction (5) to be thermodynamically favorable, the $\Delta G^{\prime 0}_{ox}(T)$ should be smaller than the $\Delta G_{CO}(T,P)$. Therefore, favorable oxidation temperature should be lower than the temperature at the intersection of the $\Delta G^{\prime 0}_{ox}(T)$ and $\Delta G_{CO}(T,P)$ lines. The $\Delta G_{CO}(T,P)$ line for $p = 1$ bar is shown in Figure 6, while the lines for other pressures can be determined graphically by connecting the point marked 'C' and the CO_2 partial pressure in the axis. On the other hand, for the reduction reaction (thermal) (6) to be favorable,

$$\Delta G(T,P) = \frac{1}{2} G_{O_2}(T,P) - \Delta G^{\prime 0}_{ox}(T) < 0. \tag{10}$$

This means the favorable thermal reduction temperature should be higher than the corresponding temperature at the intersection of the $\Delta G^{\prime 0}_{ox}(T)$ and $\frac{1}{2} G_{O_2}(T,P)$ lines. The latter can be determined graphically in Figure 6 by connecting the point marked 'O' and the oxygen partial pressure on the pO_2 axis. Additionally, the favorable operating temperature for the fuel-assisted reduction (7) can be obtained in similar manners in an Ellingham diagram showing the $\Delta G_{Fuel}(T,P)$ of the corresponding fuel oxidation reaction by oxygen gas.

Both experimental and numerical methods can be used to obtain the $\Delta G^{\prime 0}_{ox}(T)$ for different complex oxides. Recently, high-throughput *ab initio* computations, e.g., the density functional theory (DFT) [46, 47] have been used to evaluate ΔG of oxidation reactions of fluorites, perovskites and spinels. By comparing the Gibbs free energy values in the Ellingham diagram, the favorable operating temperatures for these compounds can be determined.
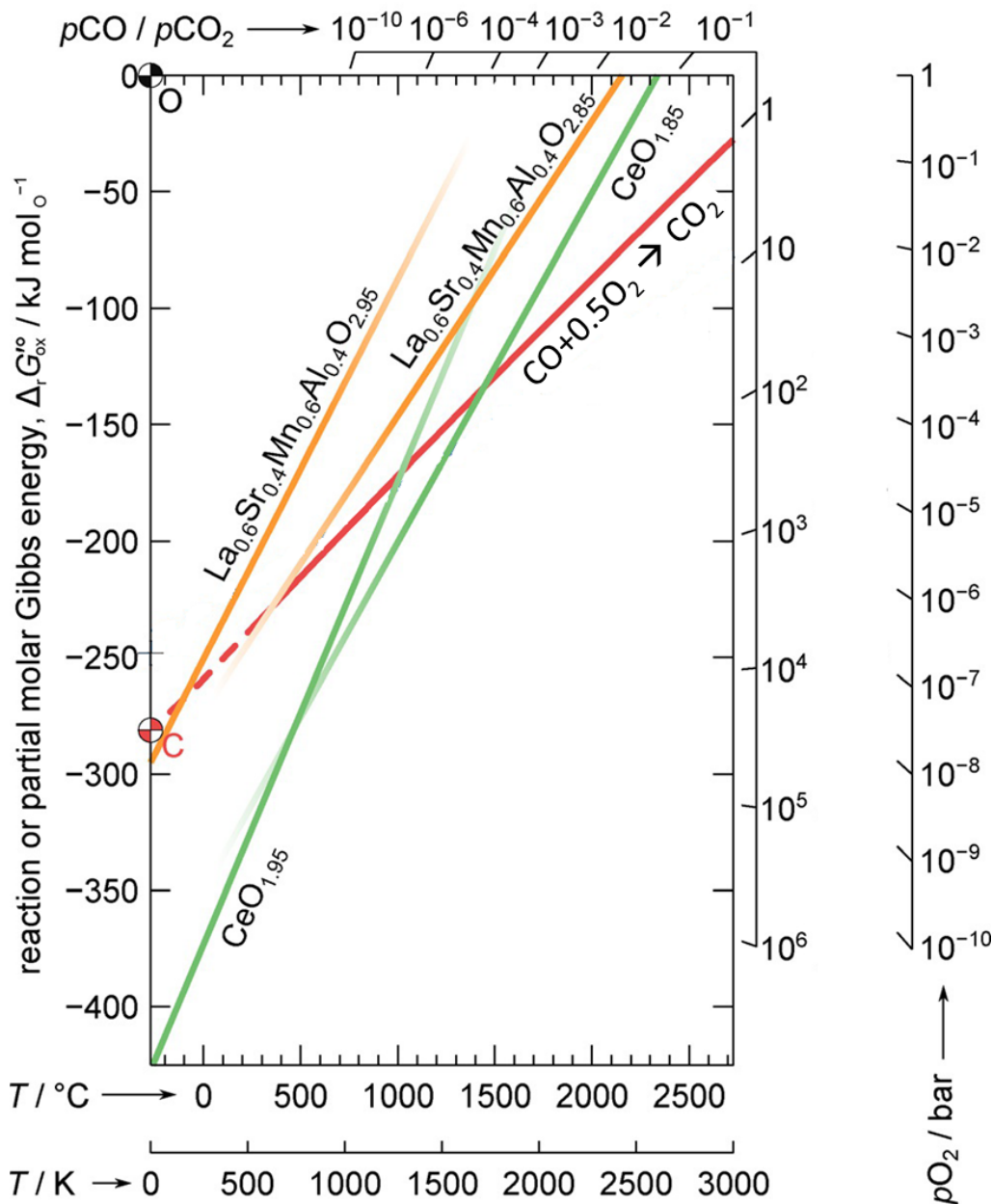
Figure 6 Ellingham diagram compares the standard partial molar Gibbs free energy changes, $\Delta G'^0_{ox}(T)$ for the oxidation reactions of $CeO_{2-\delta}$ and $La_{0.6}Sr_{0.4}Mn_{0.6}Al_{0.4}O_{3-\delta}$ at certain typical δ values, and the $\Delta G^0(T)$ for the CO oxidation reaction at standard pressure $p^0 = 1$ bar. When operating at different partial pressures, the lines for $\frac{1}{2}G_{O_2}(T,P)$ and $\Delta G_{CO}(T,P)$ can be graphically determined by connecting the points marked as 'O' or 'C' to the partial pressures in the axes, respectively. (Adapted from [45] with permission of John Wiley and Sons)

Experiments are performed to evaluate the kinetics of redox processes, which determines the reactor dimensions and system designs. In redox cycles at elevated temperatures, particle properties such as sizes and surface area evolve, and these structural changes affect the apparent kinetic parameters [48]. Furthermore, the desired shapes and sizes of the particle depend on the reactor design, e.g., fluidized bed [49] or rotary [50, 51]. Intrinsic kinetics models involve oxygen transport between the gas phase and the solid surface, and between the surfaces and the bulk. Zhao et al. [39, 52, 53] developed a kinetic model for CO_2 splitting on ceria and zirconia doped ceria using three reaction steps:

CO_2 adsorption: $\quad CO_2(g) + V_O^{\bullet\bullet}(s) + O_O^{\times}(s) \leftrightarrow \left(CO_3\right)_O^{\bullet\bullet}(s)$ $\qquad$ (11)

Charge transfer: $\quad \left(CO_3\right)_O^{\bullet\bullet}(s) + 2\,Ce_{Ce}^{'}(s) \leftrightarrow CO(g) + 2\,Ce_{Ce}^{\times}(s) + 2O_O^{\times}(s)$ $\qquad$ (12)

Oxygen transport: $\quad \begin{aligned} &V_O^{\bullet\bullet}(b) - O_O^{\times}(b) + 2\,Ce_{Ce}^{'}(b) - 2\,Ce_{Ce}^{\times}(b) \\ &\leftrightarrow V_O^{\bullet\bullet}(s) - O_O^{\times}(s) + 2\,Ce_{Ce}^{'}(s) - 2\,Ce_{Ce}^{\times}(s) \end{aligned}$ $\qquad$ (13)
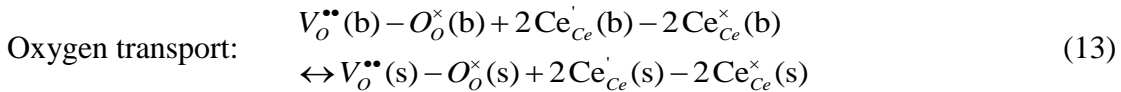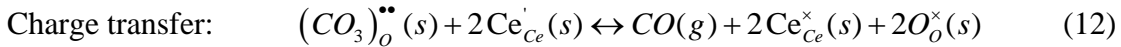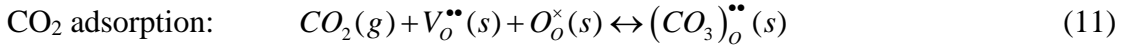
Here Kröger–Vink notation is used, and the (g), (s) and (b) indicate species in the gas phase, solid surface and bulk of solid, respectively. $V_O^{\bullet\bullet}$ is the oxygen vacancy, $O_O^{\times}$ is the lattice oxygen, $\left(CO_3\right)_O^{\bullet\bullet}$ or equivalently CO_3^{2-} is a surface carbonate group formed near the oxygen vacancy that occupies two oxygen sites. $Ce_{Ce}^{'}$ and $Ce_{Ce}^{\times}$ are Ce^{3+} and Ce^{4+}, respectively. The kinetics parameters were obtained by fitting the measured overall redox rate to this model, and the charge transfer reaction (12) was found to be the rate-limiting step for CO_2 splitting on CeO_2 and CZO [39]. The model also shows that the splitting rate is impacted by the interactions between the surface defects and the adsorbates.

2.2.2 Membrane supported CO_2 reduction

In the case of a membrane, the redox pair takes place on the feed and sweep sides, as shown in Figure 5 (b), while lattice oxygen diffuses across without imposing an external electric potential. The separation of oxygen from CO shifts the equilibrium of the splitting reaction by preventing product recombination, and hence, further CO_2 reduction can be achieved. The membranes are often very thin and highly thermally conductive and the temperature is almost the same on both sides. Oxygen separation membranes have been used for air separation under nonreactive conditions, when the sweep gas is nonreactive with oxygen, and reactive conditions, when using a fuel on the sweep side [54]. They have also been proposed for water splitting [55, 56].

The first proof-of-concept study on membrane-supported CO_2 reduction dates back to 1986, when a Japanese team reported using tubular calcium stabilized zirconia,

$(ZrO_2)_{0.9}(CaO)_{0.1}$ at 1427–1727°C [26]. This membrane was also used for water splitting at 1800°C with concentrated solar energy [34, 57]. The high operating temperature requires high solar concentration ratios, and the efficiency can drop at high temperatures as a result of the heat loss. Since then, membrane materials that work at lower temperatures, around 900°C, have been developed. The figures of merit (FOM) of these membranes are summarized as follows:

(1) Oxygen permeability: CO_2 reduction rate is proportional to oxygen flux, and oxygen permeation depends on the surface reactions on both sides, i.e., oxygen adsorption/incorporation on the CO_2 side and its desorption on the sweep/permeate side, and the ambipolar diffusion of oxygen ions/vacancies and electrons/holes across the membrane, as well as the oxygen potential gradient across the membrane [56];

(2) Active surface area: Surface reactions on both sides can, in some cases, be the limiting steps for oxygen permeation [58-60]. CO_2 reduction depends on surface reactions such as adsorption, desorption and oxygen incorporation reaction;

(3) Chemical, thermal and mechanical stabilities: As the membrane operates at elevated temperatures, material stability during heating/cooling and under long term operations is of great importance for industrial applications. The reducing environment on both feed and sweep sides (P_{O2} can be as low as 10^{-20} to 10^{-15} bar under equilibrium conditions) can also induce membrane material reduction or cation segregations, which can lead to membrane failures. Moreover, since a total pressure gradient can be used to enhance the permeation flux subjecting the membrane to stresses, mechanical stability is also important;

(4) Cost: Large membrane surface areas are required, typical oxygen permeation fluxes are $O(0.1\text{-}1 \ \mu mol \ cm^{-2} \ s^{-1})$. Expensive materials such as cobalt should be avoided and Earth abundant elements are favorable. The cost of fabrication and assembly must be competitively low;

(5) Operating temperature: High operating temperature leads to higher surface reaction kinetics and better oxygen permeability. But it also means higher maintenance and operational costs, and more expensive insulation materials are required to decrease the heat lost and gas leak. Optimization is required to have the reactor operate at appropriate temperatures to achieve the best performances.

2.2.3 Comparison between these two processes

Both chemical looping (redox) and membrane-supported CO_2 reduction processes involve oxidation and reduction reactions. In the first case, redox reactions take place sequentially by transporting the oxygen carriers between different reactors or changing the stream inputs into the same reactor, and the reaction rates can be time dependent due to the consumption and production of oxygen vacancies in the oxidation and reduction reactions, respectively. On the other hand, in a membrane reactor, redox reactions occur simultaneously on the two sides of the membrane. Under steady state operation, the oxygen vacancy concentrations on the feed or sweep sides are constant, but different.

In chemical looping, oxygen transport occurs at different scales, depending on the reactor design. If the OC is transported between different reactors, e.g., rotary reactors [50, 51] and fluidized bed reactors [49], oxygen is transported with the OCs at the macro scale and between the surface and the bulk of the particles at the micro scale. If the oxygen carriers are fixed, e.g., in fixed bed reactors [37], redox is achieved by switching the oxidizing and reducing gas streams, and only diffusion between the surface and the bulk of the particles should be considered. On the other hand, in a membrane reactor, oxygen diffuses from the feed to the sweep side, driven by the chemical potential gradient, not requiring moving the particles or switching the gas streams.

Additionally, the operating temperatures for the two reactors in redox CO_2 splitting can be different to favor the thermodynamics and kinetics of reduction or oxidation. However, operating the two reactors at different temperatures may not be optimal for the efficiency of the overall system. For instance, analysis of a system incorporating a rotary reactor (for oxy combustion) shows that isothermal operation can lead to better exergy efficiency [61]. The operating pressures for the two reactors are usually the same. On the other hand, the membrane reactor mostly operates under isothermal condition across the feed and sweep sides, and there can be a temperature-gradient from the inlet to outlet of the membrane reactor depending on the heat integration methods. Yet the pressures on both sides can be different. Having the feed side pressure higher than the sweep side pressure can improve the permeation by increasing the driving force for oxygen permeation across the membrane. Consideration of the dependence of kinetics and product selectivity on pressure should also be given when selecting different operating pressures on the two sides in the membrane.

Both processes have been identified as potential technologies for the solar-fuel production that is using solar energy in the form of heat (or electricity) to reduce water or carbon dioxide back into fuels, i.e., hydrogen or carbon monoxide, respectively. This

review focuses on the membrane supported reduction technology, and we will discuss the materials and kinetics in the membrane reactors in details in the following sections.

Table 3 Comparison between the two thermochemical processes for CO_2 reduction

	Chemical looping (redox) CO_2 splitting	Membrane supported CO_2 reduction
Oxidation reaction (location)	$CO_2 + V_O^{\bullet\bullet} \leftrightarrow CO + O_O^{\times} + 2h^{\bullet *}$	
	Oxidation reactor	Feed side of the membrane
Reduction reaction (location)	$O_O^{\times} + 2h^{\bullet} \leftrightarrow O_2 + V_O^{\bullet\bullet}$ or $O_O^{\times} + 2h^{\bullet} + Fuel \leftrightarrow O_2 + V_O^{\bullet\bullet} + Products$ depending on the integrated reduction processes	
	Reduction reactor	Sweep side of the membrane
Oxygen vacancy concentration	**Time-dependent**: As reaction goes on, the oxygen vacancies concentration in the solid particle decreases in the oxidation reactor and increases in the reduction reactor (see Fig. 2 in [39])	**Location dependent**: the oxygen vacancy concentrations vary across the membrane, being minimum on the feed side and maximum on the sweep side (see Fig. 6 in [62])
Oxygen species transport	1. **Micro scale**: Bulk $\leftrightarrow$ surface 2. **Macro scale**: Physically with the movement of the oxygen carriers (this occurs only in the fluidized beds or rotary reactors)	**Micro scale**: oxygen transport across the membrane from feed to the sweep side (feed side is the side with high oxygen potential)
Operating temperature	Oxidation and reduction can operate at different temperatures, and spatial gradient exists in the reactors (see Fig. 2 in [63])	The temperature is locally the same but can vary along the membrane laterally from inlet to outlet (see Fig. 2 in [64])
Operating pressure	1. Thermal reduction: the reduction reactor can operate at vacuum or under inert sweep at atmospheric pressure, while the oxidation reactor can operate at atmospheric pressure; 2. Fuel reduction: The two reactors can operate at the same or different absolute pressures.	Feed and sweep sides can operate at different pressures, which can impact the driving force, i.e., oxygen potential gradient, for oxygen diffusion
Reactor type	Fluidized beds [49], rotary [50], fixed beds with alternating reactant streams [63]	Planar [58], tubular [65] or monolith [64] membranes

* $V_O^{\bullet\bullet}$, O_0^x and $h^\bullet$ are oxygen vacancy, lattice oxygen and electron holes, written in Kröger–Vink notation. In these two reactions, electron holes are used for the electronic charged species as an example. In some cases of *n* type conductor, electrons can be the dominant electronic charged species.

3. Current state of membrane-supported CO₂ reduction

Oxygen permeable membranes are built from mixed ionic and electronic conducting (MIEC) materials, which can be either single-phase or mixed-phase. An MIEC material exhibits both ionic and electronic conductivity; for practical applications, the conductivities should be higher than 10^{-4} to 10^{-3} S cm^{-1} [66]. A general discussion on these membrane materials and applications, mainly for oxygen separation, can be found in [67]. In this section we will discuss these materials for CO₂ reduction, which are categorized as fluorite (chemical formula: $AO_{2-\delta}$), perovskite ($ABO_{3-\delta}$) and mixed-phase. Here, A and B are different metal cations in the fluorites or perovskite structures. Membrane separation can operate in two modes: non-reactive or reactive sweep. In the first, inert gases, such as argon and nitrogen are used to sweep the membrane surface and decrease the oxygen partial pressure. In some cases, vacuum is used to decrease the sweep side total pressure as well. The outcome of the non-reactive mode is a co-production of CO and O₂ in two separate streams (see Figure 2(a)). In the second, fuels such as hydrogen or methane are used to react with the permeated oxygen, further decreasing the oxygen potential on that side. In this case, the overall reactions are reverse water gas shift and methane dry reforming, respectively, but with the production of separate streams of CO on the feed side and water/syngas on the sweep side. While hydrogen is used as a surrogate fuel in some experimental studies, in practice and unless renewable hydrogen is available at low cost, other fuels should be used. In both hydrogen or methane sweep cases, the overall reaction in the membrane reactor is endothermic, and CO₂ reduction can be thought of as an energy storage technology converting excess heat into storable chemical energy.

Oxygen permeable membrane materials that have been tested for CO₂ thermochemical reduction are summarized in Table 5. The Arrhenius plots of the performances of some membranes are shown in Figure 7, where all the cases correspond to reactive sweep and parameters such as the membrane thickness, sweep conditions and catalysts are shown. Material synthesis and membrane fabrication techniques for these oxygen permeable membranes, and their stability are also summarized. The chemical kinetics in the processes, e.g., reaction mechanisms, defect chemistry and charged species diffusion will be discussed in the next section.
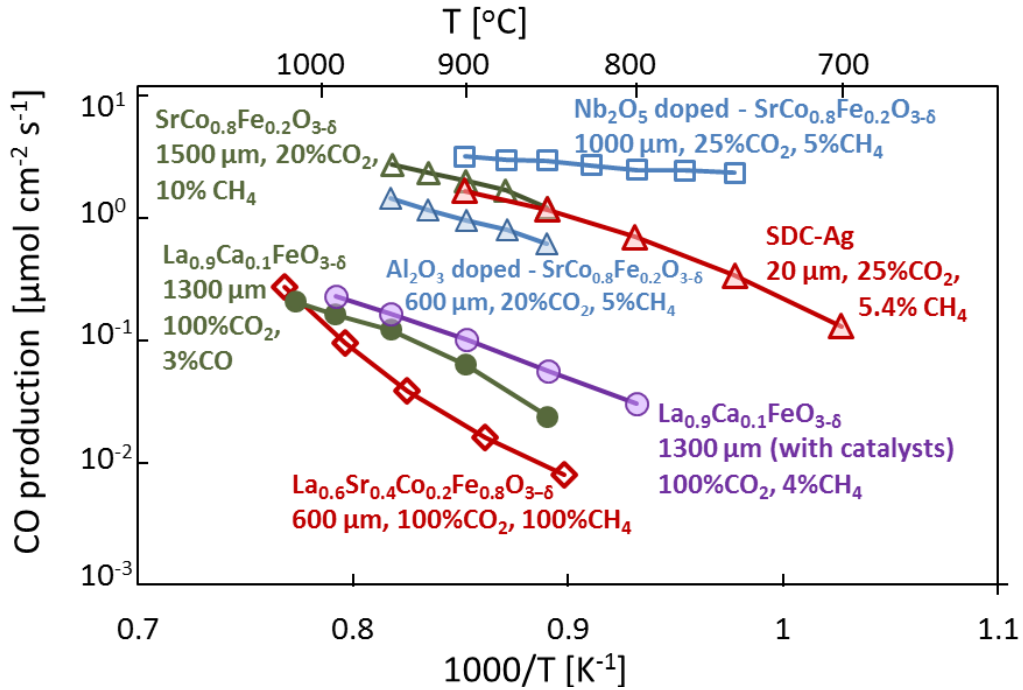
Figure 7 The Arrhenius plot of CO production rate on different oxygen permeable membranes. Solid: CO as sweep gas; hollow: CH_4 as sweep gas. The operating conditions can be found in Table 5. The number next to the label is the thickness of the dense membrane, the concentrations of the feed CO_2 and sweep fuels reported in the following literature: Nb_2O_5 doped - $SrCo_{0.8}Fe_{0.2}O_{3-\delta}$ [68], $SrCo_{0.8}Fe_{0.2}O_{3-\delta}$ [69], Al_2O_3 doped - $SrCo_{0.8}Fe_{0.2}O_{3-\delta}$ [70], $La_{0.9}Ca_{0.1}FeO_{3-\delta}$ (no catalysts) [58], $La_{0.9}Ca_{0.1}FeO_{3-\delta}$(with catalysts) [71], $Sm_{0.2}Ce_{0.8}O_{1.9}$ (SDC)-Ag [72], $La_{0.6}Sr_{0.4}Co_{0.2}Fe_{0.8}O_{3-\delta}$ [73],

3.1 Materials and membrane performance

As mentioned above, oxygen permeable materials can be categorized as fluorite, perovskite and mixed-phase materials. Fluorite-type AO_2 (A = Ce^{4+}, Ze^{4+}, etc.) oxides are good ionic conductors used extensively in oxygen sensors and fuel cells [74]. Yet they are mainly ionic conductors and their electronic conductivity is very low, so they are usually mixed with other conductors to form mixed-phase materials to enhance the oxygen permeability [75]. Perovskite-type ABO_3 (A = La^{3+}, Ba^{2+}, Sr^{2+}, etc., B = Co^{3+}, Fe^{3+}, Cr^{3+}, Mn^{3+}, etc.) materials usually exhibit high electronic conductivity compared to their ionic conductivity [76]. Both conductivities depend on the charged species concentration and mobility, which are impacted by the operating conditions such as oxygen partial pressures and operating temperatures. More about the charged species and conductivity will be discussed later in this paper. Other Ruddlesden–Popper phase materials such as $(La,Sr)_2(Ni,Fe)O_4$ [77] and $(Pr_{0.9}La_{0.1})_{2.0}(Ni_{0.74}Cu_{0.21}Ga_{0.05})O_{4+\delta}Cl_{0.1}$ (PLNCG) [78] have been studied recently for oxygen permeation due to their high structure stability at elevated temperatures. However, there is so far no literature on using these materials for supporting CO_2 thermochemical reduction. Mixed-phase materials contain more than one phase, with

each phase exhibiting a dominant conductivity. For these, the dominant conductivity of different phases can be optimized separately.

3.1.1 Fluorite-based single-phase membranes

Fluorites usually exhibit high ionic yet low electronic conductivity. Adding dopants can modify their conductivity and stability. Taking zirconia as an example, dopants such as CeO_2 and TiO_2 can enhance their electronic conductivity, while other dopants such as CaO and Y_2O_3 are essential for the stability of its cubic phase [54]. Additionally, the operating temperature and oxygen partial pressure also affect the electronic conductivity. For example, pure CeO_2 exhibits higher electronic conductivity at higher temperatures; with decreasing oxygen partial pressure from 0.21 atm to as low as 10^{-20} atm, the electronic conductivity first remains constant and then increases after a threshold partial pressure, which depends on the operating temperature [79].

Doped fluorite membranes were initially proposed to support H_2O splitting [57], and then used in CO_2 reduction. Two of the earliest experimental studies were on fluorite-based single phase membranes with either reactive or non-reactive sweep [26, 80]. Nigara and Cales [26] tested 2-mm thick tubular calcia-stabilized zirconia (10mol% CaO_2) membranes at 1427–1727ºC with CO as the sweep gas. They found that CO_2 reduction rate increased with respect to temperature and fuel concentration. The highest rate was 0.62 µmol cm^{-2} s^{-1} at 1727ºC with 99% CO. For the non-reactive sweep case, Itoh et al. [80] tested a 2 mm thick yttria-stabilized zirconia (YSZ, 6mol% Y_2O_3) tube with maximum temperature at 1509ºC and measured the maximum CO production rate with Ar sweep to be 0.488 µmol cm^{-2} s^{-1}. Recently, Tou et al. [65] tested a ceria membrane reactor with inert sweep gas in a solar simulator. The maximum CO production rate was 0.024 µmol cm^{-2} s^{-1} at 1600ºC with 3500 suns radiation. In most cases, the measured CO production rates were around 10 times lower than the theoretical limits that are calculated by equilibrating the feed side CO_2 concentration and the oxygen partial pressure on the sweep side at the corresponding operating temperature. The difference between the actual and ideal performance means that reactor optimization with the solar concentrator is necessary.

Factors such as flow rates and temperature can affect CO_2 conversion, and should be optimized to achieve best performance. For the 2-mm thick YSZ (6mol% Y_2O_3) tube, it was found that with increasing CO_2 flow rate, its conversion first decreases, increases then decreases again. In the first and third regimes, the reason is mainly due to the drop in the residence time, while in the middle regime, the drop of temperature near the outlet of the tubular membrane reduces recombination and hence, increases CO_2 conversion [80].

The electronic conductivity of fluorites is generally lower than their ionic conductivity, which can be the rate-limiting step. Nigara and Cales [26] compared a calcia-

stabilized zirconia membrane and a 20mol% CeO_2-doped YSZ membrane. The latter was found to have higher CO production rates (under CO sweep condition), mainly due to its higher electronic conductivity [26].

3.1.2 Perovskite-based single-phase membranes

Perovskite membranes have been tested for oxygen permeation, hydrogen production from water splitting and chemicals production [81]. For CO_2 reduction, Sr- and Ca-based perovskite membranes, (e.g., $SrCo_{0.4}Fe_{0.5}Zr_{0.1}O_{3-\delta}$ (SCoFZ-451) [69, 82, 83], $SrCo_{0.8}Fe_{0.2}O_3$ (SCoF-82) [68, 70] and $La_{0.6}Sr_{0.4}Co_{0.2}Fe_{0.8}O_{3-\delta}$ (LSCoF-6428) [73], $La_{0.9}Ca_{0.1}FeO_3$ (LCaF-91)[58, 71]) have been tested. Ba-based membranes perform well in supporting water splitting, and hydrogen production rate was measured as high as 3.4 µmol $cm^{-2} s^{-1}$ on a 0.1 mm thick $BaCo_xFe_yZr_{1-x-y}O_{3-\delta}$ (BCoFZ, Ni/Al_2O_3 catalysts on the sweep side) at 950°C with 10% CH_4 sweep [84], which is among the highest reported values. However, Ba-containing perovskites tend to form stable and inactive barium carbonate in CO_2 environments, as shown in the Ellingham diagram in Figure 8 [85]. In this diagram, the dotted lines show the chemical potential difference of CO_2 at arbitrary (T,P) and at $P^o=1$ bar, $\Delta\mu_{CO_2,T,P} = \mu_{CO_2,T,P} - \mu_{CO_2,T,P^o}$. The solid lines show the negative value of the Gibbs free energy of the decomposition reaction, e.g., $BaCO_3 \rightarrow BaO + CO_2$, at reference pressure P^o,

$$-\Delta G_{P^o} = -\left(G_{CO_2,T,P^o} + G_{oxide} - G_{carbonate}\right).$$ (14)

In order to make the decomposition reaction favorable, the Gibbs free energy change must be negative,

$$\begin{aligned}\Delta G_{T,P} &= G_{CO_2,T,P} + G_{oxide} - G_{carbonate} \\ &= G_{CO_2,T,P} - G_{CO_2,T,P^o} + G_{CO_2,T,P^o} + G_{oxide} - G_{carbonate} \\ &= \Delta\mu_{CO_2,T,P} - \left(-\Delta G_{P^o}\right) < 0\end{aligned}$$ (15)

Hence, in the Ellingham diagram, at the conditions where the dotted line ($\Delta\mu_{CO_2,T,P}$) is below the solid line ($-\Delta G_{P^o}$ of the decomposition of a certain carbonate), the carbonate decomposition is thermodynamically favorable. We will discuss the material stability and reaction mechanisms in details in the corresponding sections later.
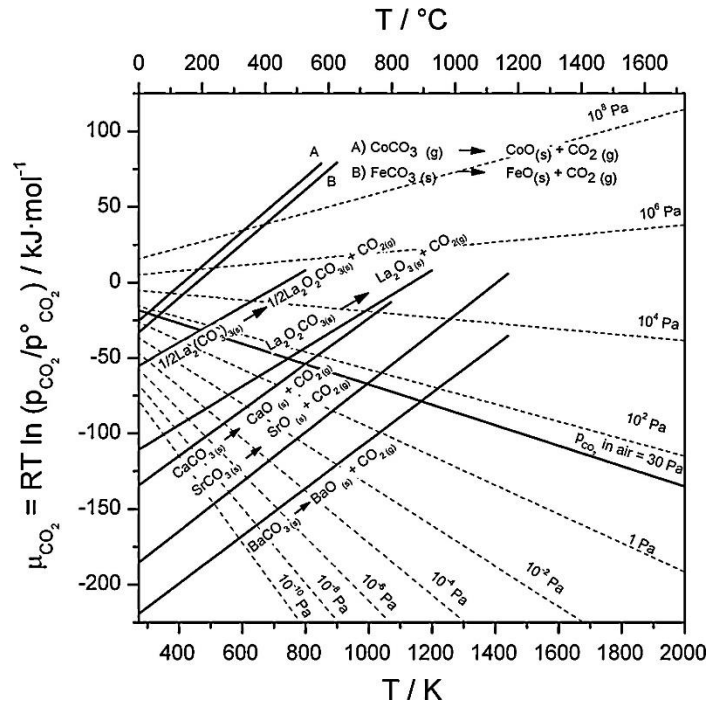
Figure 8 Ellingham diagram for the decomposition of carbonates under diffferent partial pressures and temperatures (Reprinted from [85] with permission of Elsevier)

Zhang et al. [83] studied a 1.5 mm thick SCoFZ-451 perovskite membranes for CO_2 reduction and partial oxidation of methane (POM); the highest CO production rate was around 1.56 μmol $cm^{-2} s^{-1}$ with 20% CO_2 feed and 5% CH_4 sweep at 950°C. By adding 4.77wt% Ni/Al_2O_3 catalysts on the sweep side, Jin et al. [82] found that the CO_2 reduction rate on this membrane increased, and the maximum CO production rate measured was 2.68 μmol $cm^{-2} s^{-1}$ at 950°C (20% CO_2 feed and 15% CH_4 sweep). This shows that the sweep side methane oxidation was the rate-limiting step in their setup. By adding catalysts on both sides, (i.e., Pd/SCoFZ-451 on the feed side and Ni/Al_2O_3 on the sweep side), CO_2 thermochemical reduction on a 1.5 mm thick SCoFZ-451 membrane was further enhanced at 850-950°C, and the highest CO production rate reported was 2.72 μmol $cm^{-2} s^{-1}$ at 950°C (20% CO_2 feed and 10% CH_4 sweep)[69]. However, the SCoFZ-451 perovskite membranes with 4.77wt% Ni/Al_2O_3 catalysts on the sweep side broke after 33 hours of operating (20% CO_2 feed and 5% CH_4 sweep at 900°C)[82], showing thermochemical instability.

Dopants such as Al and La which are less prone to forming carbonates have been added to increase the stability of strontium-based perovskites. A 0.6 mm thick Al-doped SCoF-82 tubular membrane was tested at 900°C with 20mol% CO_2 feed and 5mol% CH_4 sweep, and the membrane maintained stable performance for 62 hours before it broke [70]. LSCoF-6428 membranes also exhibit high stability towards carbonate formation, but its performance was much lower compared with the SCoFZ-451. A 0.6 mm thick LSCoF-

6428 membrane exhibited a maximum CO production rate of 0.28 μmol cm^{-2} s^{-1} at 1030ºC with 10% CH$_4$ in the sweep gas [73]. Higher temperature raised the CO$_2$ splitting rate on the feed side and the CH$_4$ conversion ratio on the sweep side. Yet amorphous graphite was detected on the LSCoF-6428 membrane by XRD after experiments, as a result of methane cracking [73].

Calcium-based perovskites can also be used because of the relatively unstable calcium carbonates at high temperatures (shown in the Ellingham diagram in Figure 8). Wu and Ghoniem tested 1.3mm thick LCaF-91 membranes for the CO$_2$ thermochemical reduction with fuel sweep, and the membrane showed more than 100 hours of stable performance [58, 71]. The maximum CO production rates reported were 0.38 and 0.32 μmol cm^{-2} s^{-1} with 9.5 mol% H$_2$ and 11.6 mol% CO sweep at 990ºC, respectively [58].

Another method to improve the stability of the membrane is by adding porous layers on its surfaces, which can protect the dense membrane against corrosive gases by physically decreasing the contacts. For example, the bare 0.5 wt% Nb$_2$O$_5$ doped SCoF-82 (SCoFNb) membrane without porous layers maintained high performances for 35 hours (16.7mol% CO$_2$ feed, 4.8mol% CH$_4$ sweep at 900ºC); carbonates were found on the CO$_2$ feed side, and unidentified materials on the CH$_4$ sweep side (by XRD) [68]. By adding La$_{0.8}$Sr$_{0.2}$MnO$_{3-\delta}$(LSM-82)/YSZ+Pd on the CO$_2$ side and Sr$_{0.7}$Ba$_{0.3}$Fe$_{0.9}$Mo$_{0.1}$O$_{3-\delta}$ (SBFMo-7391)+Ni on the sweep side, a 1.0 mm thick SCoFNb membrane showed stable performance for 500 hours (16.7mol% CO$_2$ feed, 4.8mol% CH$_4$ sweep at 900ºC) [68]. Another example is that Zhang et al. [83] studied how a SCoFZ-451 porous layer impacted the stability of the SCoFZ-451 membrane. They found that when the layer was added to the feed or sweep sides, the membrane lasted for ~3.2 and 1.7 times longer, respectively, than the unmodified membrane under the same operating conditions (20% CO$_2$ feed and 5% CH$_4$ sweep at 900ºC)[83].

Apart from protecting the dense membrane, a porous layer can also increase the number of active sites and/or catalyze the surface reactions, and can improve the performance if surface reactions are the rate limiting steps. Zhang et al. [83] applied porous SCoFZ-451 layers onto different sides of a dense SCoFZ-451 membrane, and found that the porous layer on either side can slightly enhance the CO$_2$ reduction rate, especially at low temperatures around 800ºC. Adding the porous layer onto the feed side led to a better performance than adding it onto the sweep side, and the difference was more obvious at higher temperatures [83]. For the 1.3 mm thick LCaF-91 membrane, the CO production rate was enhanced by 1.4 times by putting porous LCaF-91 layers on both sides of the membrane at 990ºC (100% CO$_2$ feed, 1-8% CO sweep) [71]. The performance was further improved by adding 20mol% CZO/LCaF-91 and 20mol%

$(La_{0.6}Sr_{0.4})_{0.95}Co_{0.2}Fe_{0.8}O_3$/LCaF-91 porous layers on the feed and sweep sides, respectively, with one order of magnitude improvements at lower temperatures around 850ºC [71].

It was found that for the 1.5 mm thick SCoFZ-451 perovskite membranes with methane sweep and 4.77wt% Ni/Al_2O_3 catalysts on the sweep side, the oxygen fluxes, methane and CO_2 conversion ratios, and CO selectivity from methane oxidation all increased with temperature [82]. Additionally, higher methane concentration at the inlet leads to lower CH_4 conversion ratio but higher CO selectivity on the same membrane. And increasing CO_2 concentrations on the feed side leads to higher oxygen fluxes and methane conversion, but the CO_2 conversion ratio and CO selectivity from POM both drop.

3.1.3 Mixed-phase membranes

Mixed-phase MIEC materials contain two and more phases with similar thermal expansion coefficients and chemical compatibility. Four types of mixed-phase membranes have been used as oxygen permeable membranes, as shown in Figure 9 [86]. Among them, two types were reported for supporting CO_2 reduction: $SrFeCo_{0.5}O_{3-\delta}$ (SFC2), which is a mixture of intergrowth $(Sr_4Fe_{6-x}Co_xO_{13\pm\delta})$, perovskite $(SrFe_{1-x}Co_xO_{3-\delta})$ and spinel $(Co_{3-x}Fe_xO_4)$ phases (Figure 9a) [87]; and samarium-doped ceria (SDC) with Ag or Pt circuits at the edge to enhance the electronic conductivity [72] (Figure 9c). Other mixed-phase membranes were tested for air separation (e.g., $Ce_{0.8}Sm_{0.2}O_{2-\delta}$ with fiber shaped $PrBaCo_2O_{5+\delta}$ dual phase membrane [88] (Figure 9b), and short-circuit $Ce_{0.9}Gd_{0.1}O_{2-\delta}$ with dual-phase decoration of $Ce_{0.9}Gd_{0.1}O_{2-\delta}$ – Ag [86] (Figure 9d), but not yet tested for CO_2 reduction. Mixed-phase membranes show potentials for high performance and stability for CO_2 reduction, as shown in Figure 7 and Table 5.
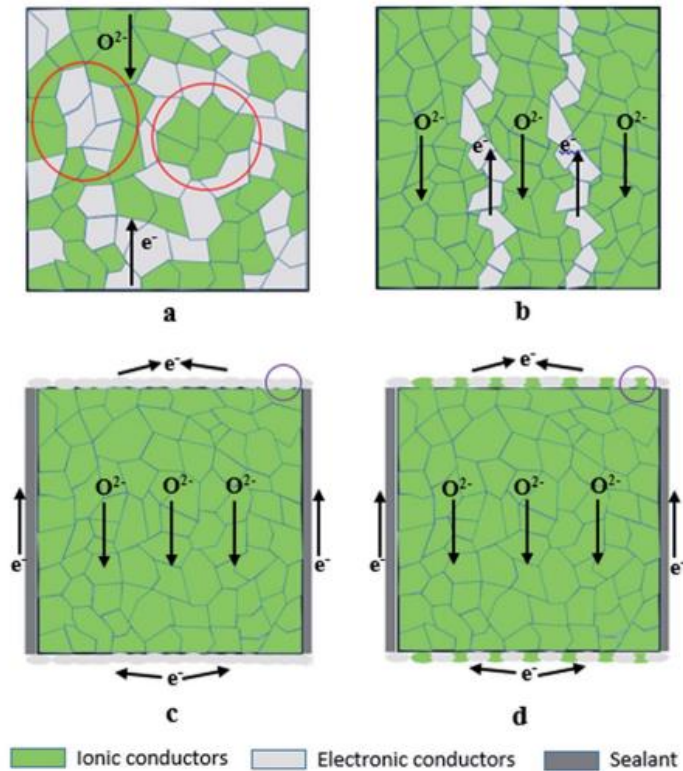
Figure 9 Cross-section schematic diagram of (a) dual-phase membrane, (b) dual-phase membrane with a minimum electronic conducting phase, (c) membrane with external short-circuit decoration and (d) membrane with dual-phase external short-circuit decoration (Reproduced from [86] with permission of the Royal Society of Chemistry)

Strontium iron cobalt oxide (SFC2) membranes have been tested for oxygen separation and water splitting [89, 90]. Oxygen fluxes as high as 6 μmol cm^{-2} s^{-1} were measured at 900 $^{\circ}$C on a 0.02 mm SFC2 thin film with SFC2 porous substrate on the sweep side when 80% H$_2$ was added on the sweep side and 49% H$_2$O on the feed side [89]. For CO$_2$ reduction, Fan et al. [91] studied a 2 mm thick SFC2 disk membrane and measured CO production rate as high as 0.25 μmol cm^{-2} s^{-1} at 940°C. They also found that increasing the temperature and CO$_2$ concentration raised the oxygen flux, and the CO$_2$ splitting rate [91].

For the Sm$_{0.2}$Ce$_{0.8}$O$_{1.9}$ (SDC) membrane with Ag or Pt circuits at the edge, Zhang et al. [72] applied different catalysts on the two sides: Ag or Pt catalysts for CO$_2$ reduction and GdNi/Al$_2$O$_3$ for partial oxidation of methane. Two different thicknesses were tested, and they found that at low temperatures (750–850°C), the 20 μm thin film membrane (on SDC porous support) performed slightly better than the 1 mm thick dense membrane, and the former showed CO production rate as high as 1.819 μmol cm^{-2} s^{-1} at 900 $^{\circ}$C (25% CO$_2$ feed and 5.4%CH$_4$ sweep) [72]. In addition, both Pt and Ag metal circuits improved CO$_2$

reduction rates by an order of magnitude compared to the cases without, and Pt circuits had the superior performance [72]. Higher temperature increased the reduction rate, the oxygen flux, CO selectivity and CH_4 conversion, while higher CO_2 flow rates on the feed side raised the oxygen flux and methane conversion but dropped the CO selectivity from POM [72]. Moreover, higher CH_4 flow rates increased the oxygen flux, CO selectivity on the sweep side and CO_2 conversion on the feed side, but significantly decreased methane conversion [72].

3.2 Discussions on experiments

As summarized above and in Table 5, various membrane materials were tested in lab-scale reactors across a range of operating conditions. In order to compare their performance, information regarding material synthesis and membrane fabrication techniques, and performance measurements such as the reactor setup, measurement uncertainties, and sampling locations should be reported in details. In this section, we will discuss how these factors can impact the membrane performance measurements, and hence can lead to uncertainties when evaluating the materials, catalysts and membrane configurations.

3.2.1 Material synthesis

Material preparation methods result in unique microstructures, e.g., grain sizes and grain boundary length that impact their electronic and ionic conductivities. Generally, there are five methods to synthesis the oxide powders [92]: solid state reaction, co-precipitation, sol-gel, hydrothermal synthesis, and spray/freeze drying. New methods such as flame synthesis of functional particles are under development [93]. Kharton and Marques [94] reviewed the relationship between the microstructures and charged species transport in oxides and found that for microcrystalline solid-electrolyte materials with predominant electronic transport, larger grain size often leads to higher ionic conductivity. More recently, Saher et al. [95] investigated the apparent oxygen diffusion and surface exchange coefficients of undoped or Zr-doped $Ba_{0.5}Sr_{0.5}Co_{0.8}Fe_{0.2}O_{3-\delta}$ (BSCoF-5582) for oxygen transport during long term high temperature annealing. They found that the coefficients of all the membranes dropped with the annealing duration, but membranes with larger grain sizes experienced less deterioration probably because less non-conducting secondary phase were formed in the grain boundaries. Hence, factors such as the steps of material synthesis and membrane manufacture procedures as well as the resulting membrane morphologies, such as surface structure and grain size, all impact the reproducibility of the results. On the other hand, controlling the evolution of these oxide microstructures, such as optimizing the grain size [95] and exsolving nano-catalysts [96], can provide new opportunities to enhance the material performances.

Here, we briefly summarize the three methods used to prepare the membranes listed in Table 6. A comparison on the particle properties synthesized by these methods and the corresponding membranes are shown in Table 4. More information about the particle synthesis method can be found in [67] and [92].

Table 4 Comparison among material synthesis and membrane fabrication methods

Material synthesis			
Method	Particle size	Temperature	Purity
Solid state reaction	Large (~100 nm)	High	Low
Co-precipitation	Small (~20 nm)	Low	High
Sol-gel method	Small (~ 20 nm)	Medium	High
Membrane fabrication			
Method	Membrane configuration	Facility required	Typical thickness [67]
Dry-pressing	Planar, tubular (closed-one-end)	Mold/die, press (uniaxial or isostatic)	0.5 – 3 mm
Plastic extrusion	Tubular, monolith	Extrusion machine (propulsion system, die and cutting device)	0.5 – 3 mm
Phase-inversion spinning	Tubular	Spinneret, phase-inversion equipment	0.1 – 0.5 mm
Painting or coating	Thin film, porous layer	Brush, and/or screens	~10 μm

(1) Solid state reaction

Solid state reaction, or the mixed-powders technique, is the most common approach to produce ceramic particles [54]. Oxides, carbonates, hydroxides or salts are weighed according to the cation stoichiometric ratios, mixed and ball-milled up to two days. Organic liquids, such as methanol [97] and isopropyl alcohol [98] are applied to the solid mixture to increase its homogeneity. After milling, the dried mixture is calcined at high temperatures. The calcined temperature depends on the materials. For example, the mixture to synthesize Nb doped $SrCo_{0.8}Fe_{0.2}O_{3-\delta}$ particles was calcined in air at 950^oC for 5 hours [68], while the one for $SrCo_{0.4}Fe_{0.6}O_{3-\delta}$ was calcined in air at 900^oC for 10 hours [99]. During this calcination process, the cations diffuse in the mixture to form the desired stable crystals [100]. The particle size distribution is usually wide and ball-milling is required to make finer ceramic particles for further processing. The homogeneity and purity of the ceramic powders prepared by the solid state reaction method are usually poor [92]. Besides, energy requirements for ball-milling is high as well as for the high temperature calcination.

(2) Co-precipitation

Co-precipitation is one of the oldest methods to prepare crystals with particle sizes on the scale of nanometers. The desired amounts of cation precursors are dissolved and mixed with the precipitating agent. After mixing, a series of processes such as filtration, drying and thermal decomposition are performed. For example, Jeon et al. [101] prepared $LaNiO_{4+\delta}$ (LNO) powders using this method. Stoichiometric fractions of cation precursors, in this case lanthanum acetate hydrate and nickel acetate tetrahydrate, were dissolved in distilled water and mixed thoroughly. The precipitating agent, that is ammonium hydroxide, was added to adjust the pH level to 10 for precipitation. After filtration, washing and drying, the precipitate was calcined at elevated temperature to form the desired LNO crystals, and the calcination temperature could be determined by thermogravimetric analysis [102]. The particle morphology and purities can be well controlled by the pH, mixing rate, thermal decomposition temperature, and cation concentrations in the solution. Doping agents can be added to avoid composition inhomogeneity [54]. As the temperatures for co-precipitation are lower than the solid-state reactions, less energy will be consumed for particle synthesis.

(3) Sol-gel method

The sol-gel method or Pechini method for non-silicate ceramics has been under development since 1948 for preparing functional oxides such as titanate or mixed cation perovskites [54]. It provides excellent composition control and the resulting ceramic particles are of very high purity. Different routes are adopted, such as the all-alkoxide method, alkoxide-salt citrate-type method and hydrous oxide solutions [92]. Generally, an amorphous gel is produced from the cation precursors, e.g., metal nitrates and metal alkoxides, with the addition of a chelating agent, e.g., glycine, citric acid and ethylenediaminetetraacetic acid (EDTA). Polymerization promoters such as ethylene glycol can also be applied to control the gel formation. After the gel is formed, it is dehydrated at low temperature and then calcined at high temperature to form the desired oxides. Sol-gel method has been successfully applied to produce functional oxides with high purity, such as samarium-doped CeO_2 [72] membranes for CO_2 reduction applications.

3.2.2 Membrane fabrication

The membrane fabrication, especially the porous layer fabrication methods impact the membrane performance, by impacting the pore morphologies and transport properties such as porosity, constriction factor and tortuosity. There are generally three steps to fabricate a membrane: shaping, sintering and reprocessing [67]. Various shaping approaches have been used to fabricate the porous supports, e.g., hydrothermal process [103], screen-printing [104], freeze casting [105, 106], and phase-inversion [107]. The Thiele Modulus, ϕ, can be used to evaluate the kinetics properties of the porous layer, and it is defined as the ratio of the reaction rate over the diffusion rate in the porous layer [71, 108],

$$\phi^2 = \frac{r_{surf}}{D_{AB,e}\left(C_{A0}/L_c\right)} = \frac{J_{O_2}L_c}{D_{AB,e}C_{A0}}, \tag{16}$$

Here, r_{surf} is the overall reaction rate on the porous surface, [mol cm^{-2} s^{-1}], $D_{AB,e}$ is the effective diffusivity between gas species A and B, [cm^2 s^{-1}], and C_{A0} is the concentration of gas species A on the membrane surface, [mol cm^{-3}], L_c is characteristic length of the porous layer, [cm], i.e., the layer thickness, and J_{O2} is the oxygen flux, [mol cm^{-2} s^{-1}]. Rachadel et al. [109] found the connections of the pores to be very important to effectively transfer the gas species in and out of the membrane surface, and in some cases when the openings of the pores are narrow, the porous support had a negative impact on the oxygen flux across the membrane. Hence, porous layers with finger-like pores are preferred to decrease the concentration polarization. Fabrication methods such as freeze-casting [105, 106], and phase-inversion [107] can be used to produce these elongated pores as shown in Figure 10.

In the following, four conventional shaping methods are summarized, and compared in Table 4. More information about membrane fabrication methods can be found in [67].

(1) Dry-pressing

Pressing is a straightforward method to prepare membranes with simple geometries such as plates and closed-one-end (COE) tubes. The as-synthesized particles are ground and pressed in a uniaxial or isostatic press in a mold (rubber or stainless steel) into desired tubes or plates [110, 111]. For two-phase membranes, mixing of different phases is required before grounding and pressed, and binders such as polyninyl alcohol can also be added [112]. In order to make a porous surface, graphite or organic particles are mixed with the functional material particles as pore formers [59]. For example, Wu et al. [59] prepared a porous LCaF-91 layer by mixing its powers with graphite powders (<20μm, Sigma-Aldrich®) at 50 vol% with a mortar and pestle for twenty minutes, then compressed the mixture into a flat circular plate at 10 metric ton-force for 1 minute. After sintering at 1450°C for 30 minutes, a porous substrate with pore size on the order of several micrometers was produced.

(2) Plastic extrusion

Plastic extrusion is usually applied to fabricate tubular membranes. First, a mixture with good plasticity, known as a 'slip', consisting of ceramic particles and organic additives, i.e., a solvent, a dispersant, a binder and a plasticizer is prepared [113]. Then the slip undergoes solvent evaporation and extrusion to form tubular membranes. For example, Zhu et al. [114] prepared a 0.3 mm thick tubular $SrCo_{0.4}Fe_{0.5}Zr_{0.1}O_{3-\delta}$ (SCoFZ-451)

membrane for water splitting using a slip with a mixture of 76 wt% SCoFZ-451 powder, 10 wt% polyvinyl alcohol solution, 10 wt% dextrin and 4 wt% tung oil.

(3) Phase-inversion spinning

Phase-inversion spinning is similar to plastic extrusion, as both are derived from polymer fabrications and used to prepare tubular membranes. In this method, ceramics powders are mixed with organic solutions to form a slurry, which is spun through a spinneret to form green tubular membranes [84, 115]. Jiang et al. [84] prepared 0.17 mm thick hollow fiber tubular BCoFZ membranes using this method: they first mixed BCoFZ with a solution of polysulfone in 1-methyl-2-pyrrolidone and ball-milled the mixture for 16 hours; then the slurry was spun through and a green BCoFZ perovskite fiber obtained was cut into 0.5 m pieces and sintered in a hanging geometry at 1320°C for 5 h. After sintering, a thin dense membrane with porous support is ready.

(4) Painting or coating

Painting or coating is an effective approach to fabricate thin film membranes on a porous support, while the porous support is prepared by sintering a mixture of ceramic particles and combustible particles using methods described above. The slurry for painting usually consists of the functional oxide powders, a binder, a plasticizer, poly-vinyl butyral, α-terpineol [116]. After the slurry is painted onto the substrate, the asymmetric membrane is dried and sintered to form a dense thin film on the porous support. Park et al. [116] painted a 0.05 mm thick dense $La_{0.7}Sr_{0.3}Cu_{0.2}Fe_{0.8}O_{3-\delta}$ (LSCuF-7328) thin film membrane on the porous substrates with the same perovskite material. The sample was then dried at 80°C for 1 hour and heated at 1100–1140°C for 10 h in air.
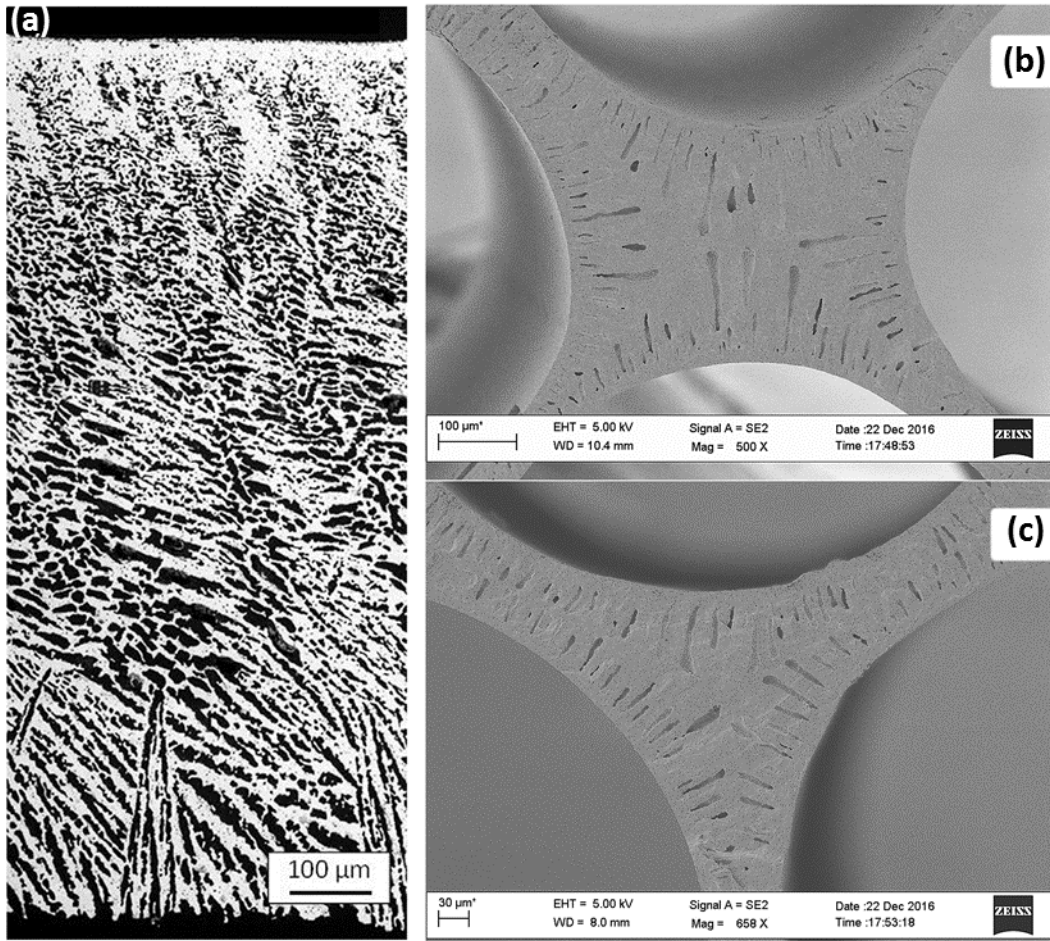
Figure 10 (a) Cross section of the asymmetric $Ba_{0.5}Sr_{0.5}(Co_{0.8}Fe_{0.2})_{0.97}Zr_{0.03}O_{3-\delta}$ membrane with freeze-casting porous support (after oxygen permeation measurement) (Reprinted from [106] with permission of Elsevier), (b) and (c) the microstructure of the multi-bore $La_{0.6}Sr_{0.4}Co_{0.2}Fe_{0.8}O_{3-\delta}$ membranes with porous support by phase-inversion method (Reprinted from [107] with permission of Elsevier)

3.2.3 Test reactor designs and experimental setups

Test reactor designs impact the performance measurements in the lab, especially near the membrane surface. For a button cell reactor which is often used in lab-scale tests, the membrane can experience radial gas concentration variation as shown in Figure 11(a)-(c). Gozalvez-Zafrilla et al. [62] carried out a computational fluid dynamics (CFD) simulation of the oxygen partial pressure on the sweep side (inert sweep) of a membrane reactor for air separation. They found the oxygen concentration varying along the radius, which is impacted by the sweep gas flow rate and the gap between the feeding tube of the sweep gas and the membrane (Figure 11(c)). Larger gap and smaller sweep gas flow rate increase the homogeneity of the gas concentration, but decrease the oxygen flux. In order

to maintain a constant gas concentration on the membrane surface, Ghoniem and colleagues [117-119] built a stagnation flow reactor as shown in Figure 11(d). The planar, finite-gap stagnation flow configuration (Hiemenz flow, Figure 11(e)) has a self-similar flow field near the membrane surface, and the temperature and gas species concentration vary only in the direction normal to the membrane (assuming no gas phase reaction).

When more complex fuels such as methane, ethane and methanol are used on the sweep side, the gas phase reactions cannot be neglected. Wu et al. [59, 71] used a micro-probe to sample the gas close to the surface, and compared them with values measured at the reactor outlet. They found gas phase reactions to contribute greatly to the final products. In water splitting or CO_2 reduction, when methane is used on the sweep side, full oxidation is more favorable near the membrane surface; as gas products travel from the surface to the outlet, H_2O and CO_2 reform the unreacted methane, and the products at the outlet have a H_2/CO ratio closer to the stoichiometric values of partial oxidation products. While the overall performance can be deduced from the inlet and outlet measurements, the surface reaction mechanisms should be derived based on local measurements using micro-probes or Raman spectroscopy.
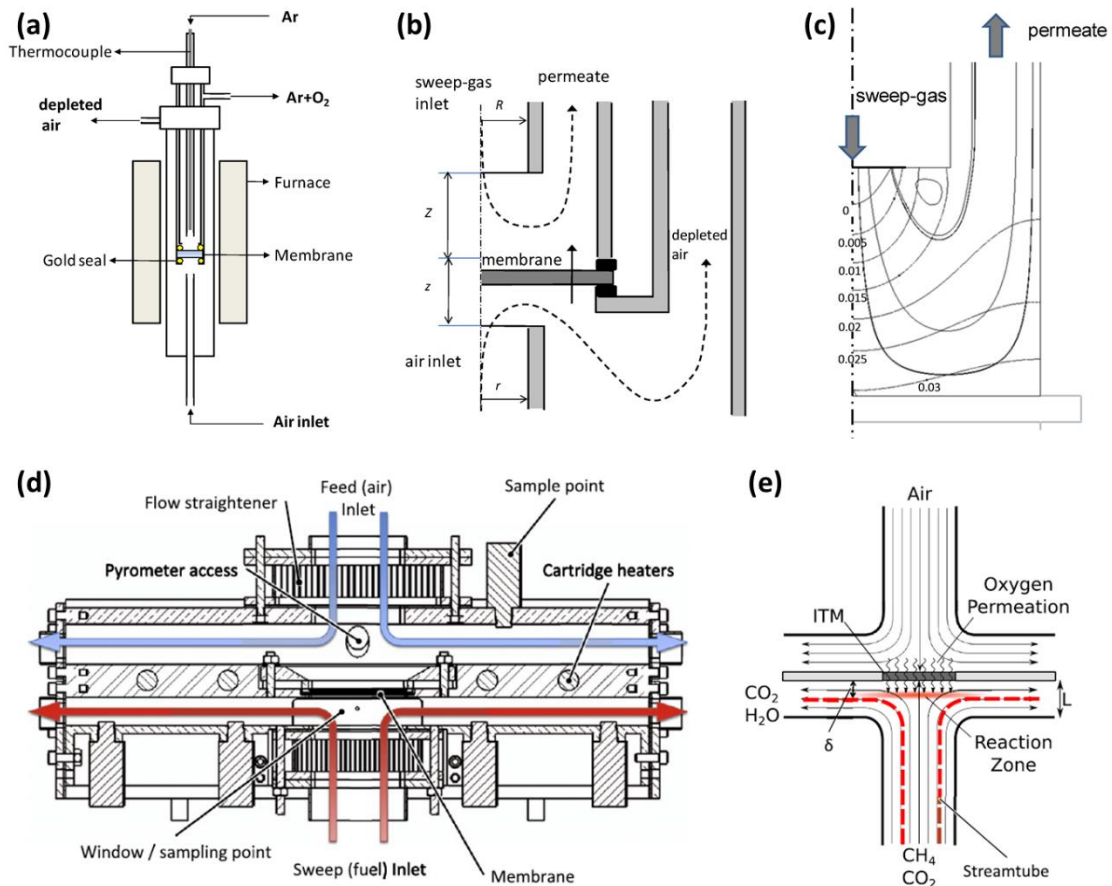
Figure 11 Two types of commonly used reactor configurations are shown: the button-cell and the stagnation membrane reactors. (a) and (b) schematic and zoom-in of a button-cell reactor, (c) flow streamlines and oxygen molar fraction profiles in the permeat side of the reactor (operating conditions in [62]), (d) crsoss-section view of the stagnation flow reactor, (e) flow field inside the reactor, Hiemenz flow. (Reprinted from [62] and [119] with permission of Elsevier)

3.3 Material stability

Oxygen permeable membranes that can work stably in a CO_2 environment have been investigated for air separation or oxy-fuel combustion. A recent detailed review of this topic can be found in Zhang et al. [22]. Carbonates on the sweep side surface were found to decrease the oxygen permeation across the membrane [120]. For example, Tong et al. [121] found that carbonates formed on the BCoFZ membrane surfaces exposed to pure CO_2 environment, but the carbonate decomposed when the membrane was exposed to 1%O_2+99%Ar for an hour at 800ºC. Similarly, Kovalevsky et al [120] found that when the sweep gas was switched from inert gases to CO_2, the oxygen flux through BSCoF-5582

decreased, because of the formation of carbonates on the surface. $BaCo_{1-x-y}Fe_xNb_yO_{3-\delta}$ (BCoFNb) also suffered from carbonate formation that leads to lower oxygen flux with CO_2 sweep [122, 123]. The Ellingham diagrams (shown in Figure 8) is often used to examine the potential of carbonate formation on the membrane surface [85], and the tendency for carbonate formation increases in the order of $Ca^{2+} < Sr^{2+} < Ba^{2+}$.

Membrane stability with CO_2 reduction is summarized in Table 6. From the table, we can see that even though the Ellingham diagram shows that $CaCO_3$ and $SrCO_3$ are ready to decompose under low CO_2 partial pressure and high temperature, carbonates were still found on the surfaces of Sr- and Ca-based perovskites following the experiments. For example, $SrCO_3$, Co_2O_3 and Fe_2O_3 were identified with XRD on the feed surface and $SrZrO_3$ on the sweep surface, after the SCoFZ-451 membrane broke in a 33-hour CO_2 reduction experiment with 20% CO_2 on the feed side and 5% CH_4 on the sweep side at 900ºC [83]. For LCaF-91, impurities such as $FeCO_3$, $CaCO_3$, $Ca_2Fe_2O_5$ were found on the feed surface, but these impurities had hardly any impact on the performances for CO_2 reduction during 106 hours with 100% CO_2 on the feed side, and 1-12% H_2 or CO on the sweep side at 990ºC [58]. These results show the limitation of using the Ellingham diagram based only on carbonate formation and CO_2 chemical potential to discover stable membranes. The gas environment in CO_2 reduction experiments can be more complicated and the carbonate formation mechanism can be related with other factors such as the cation diffusion and oxygen evolution from the surface. For example, Yi et al. [124] examined the carbonate formation on $BaCo_{1-x-y}Fe_xNb_yO_{3-\delta}$ (x = 0.2 - 0.8, y = 0.2) membranes by annealing them in various CO_2 environments. They found that the tendency for carbonate formation increases in the order of: 30% CO_2/Ar < 100% CO_2 < 30% CO_2/O_2. O_2 in the atmosphere increases $BaCO_3$ formation as more Ba^{2+} is diffused to the surface. This Ba^{2+} outward diffusion mechanism was confirmed by a recent DFT study on CO_2 adsorption on $BaZrO_3$ [125]. However, the opposite trend is found on SCoF-82, as the amount of carbonates dropped with increasing O_2 concentrations when the perovskite powders were annealed in O_2/CO_2 mixtures (p_{O2} = 10^{-4} to 0.2 bar) at 950ºC. Since less carbonate is formed in the presence of oxygen, the case with 5% O_2/CO_2 sweep leads to more stable oxygen permeation rates than pure CO_2 sweep case [126]. More careful examinations, especially *in situ* surface characterizations, are required to understand the carbonate formation and CO_2 reduction mechanisms.

On the other hand, during CO_2 reduction, the formation of CO on that side influences carbonate formation by changing the Lewis acidity (electron acceptor) and basicity (electron donor) of the oxide surface [127]. For an oxide, the acidity and basicity are attributed to the surface cations (M^{n+}) and anions (O^{2-}), respectively [128]. The number of acid and basic sites can be probed by the NH_3 and CO_2 adsorption experiments, respectively. Other methods such as infrared (IR) and Raman spectroscopy, X-ray

photoelectron spectroscopy (XPS), low-energy ion scattering (LEIS) and temperature programmed desorption/reduction (TPD/TPR) can also be applied to characterize the surface acid and base sites [129]. Generally, higher oxidation states or higher binding energy for lattice oxygen are related to lower basicity [22], which means less prone to CO_2 adsorption or carbonate formation. For example, the acidity decreases in the order of Nb^{5+} > Co^{4+} > Fe^{4+} > Co^{3+} > Fe^{3+} > Co^{2+} > Fe^{2+}, so the doping of Nb^{5+} in the perovskite structure can decrease the carbonate formation tendency [124]. However, lowering basicity also means increasing the oxygen bonding energy and decreasing the oxygen vacancies available and hence, the oxygen diffusivity of the membrane drops [130, 131]. For example, dopants such as Al^{3+} are added into SCoFZ-451 membranes to increase their resistance towards carbonate formation, but the performance drops compared with undoped membranes [70]. In addition, higher basicity increases CO adsorption capability, which induces carbonate formation from CO. It was found that with increasing basicity along the series MgO, CaO and SrO, the adsorption capacity of CO on the oxide surface increases [132]. Higher operating temperatures or reducing environments leads to lower oxidation states of the oxides or more oxygen vacancies and hence, increases the basicity. As a result, more CO_2/CO adsorption will occur on the oxide surface at higher temperatures or more reducing environment. For example, with increasing the temperature, more basic sites were found on $SrTiO_3$ surfaces with CO_2 adsorption microcalorimetry measurements [133]. Similar results are also shown in $LaMnO_3$ to that with high pretreatment temperatures, more oxygen-deficient surfaces (basic sites) are available, and hence, more CO_2 are adsorbed on the surface [134]. In CO_2 reduction process, the continuous production of CO increases the reducing environment on the feed side, and this will increase the basicity and induce more carbonate formation on the surface. This could be the reason for the carbonate formation observed in some of the Sr- or Ca-based membranes in Table 6, even though they are predicted to be carbonate-free by the Ellingham diagram in Figure 8.

Recent advancements in *in situ* and *operando* material characterization methods can be applied to examine membrane stability during CO_2 reduction. For example, using *in situ* Raman spectroscopy, Cheng and Liu [135] observed sulfur poisoning of Ni-YSZ anodes for solid-oxide fuel cells while cooling from ~500-800°C to room temperature, which could not be revealed by *ex situ* Raman experiments. Hardy et al. [136] examined the composition change of an LSCoF-6428 cathode of a solid-oxide fuel cell using *in situ* XRD, and observed gradual expansion of the lattice structure during operation, which was correlated with Sr and Co losses. So far, there are not any reports on using these *in situ* and *operando* methods to characterize the stability of membranes under CO_2 reduction. Interested readers can find more information on these characterization methods in [137-139].

Even though carbonate formation can decrease the membrane stability, CO_2 adsorption or carbonate formation can be the first step of the CO_2 reduction on the oxygen permeable membranes. More about the reduction mechanisms will be discussed later in this review.

Table 5 List of membrane materials for supporting CO_2 thermochemical reduction

Ref	Materials	Geometry	Thickness* [mm]	Catalyst	pCO_2 [atm]	pSweep† [atm]	T [ºC]	Max CO production [µmol/cm²•s]	Operation period
1. Fluorites									
[80]	6 mol% Y_2O_3 - 94 mol% ZrO_2	Tubular	2	/	1	Ar	1311 – 1509	0.488	/
[26]	10 mol% CaO – 90 mol% ZrO_2	Tubular	2	/	1	CO +CO_2	1427 – 1727	0.62	/
[65]	CeO_2	Tubular	<0.5 mm	/	1	Ar	1450 - 1600	0.024	10 h
2. Perovskites									
[82]			1.5	NiO/Al_2O_3 (sweep)	0.2 – 0.5	CH_4: 0.05 – 0.15	850 – 950	2.68	33 h
[83]	$SrCo_{0.4}Fe_{0.5}Zr_{0.1}O_{3-\delta}$	Disk	1.5 (10 µm)	/	0.2	CH_4: 0.05	800 – 950	1.64	68 h
[69]			1.5	Pd/SCoFZ-451 (feed); Ni/Al_2O_3 (sweep)	0.2	Inert or CH_4: 0.1	850 – 950	2.72	40 h
[70]	3 wt% Al_2O_3-doped	Tubular	0.6	Ni/Al_2O_3 (sweep)	0.2	CH_4 : 0.05 – 0.15	850 –	1.64	62 h

Table 5 List of membrane materials for supporting CO_2 thermochemical reduction

Ref	Materials	Geometry	Thickness* [mm]	Catalyst	pCO$_2$ [atm]	pSweep† [atm]	T [ºC]	Max CO production [μmol/cm²•s]	Operation period
	SrCo$_{0.8}$Fe$_{0.2}$O$_{3-\delta}$						950		
[68]	5 wt% Nb$_2$O$_5$-doped SrCo$_{0.8}$Fe$_{0.2}$O$_{3-\delta}$	Disk	1.0 (20 μm)	LSM-82/ YSZ+Pd (feed); SBFMo-7391+Ni (sweep)	0.05 - 0.5	CH$_4$: 0.05 – 0.125	750 – 900	3.16	500 h (35 h without porous layers)
[73]	La$_{0.6}$Sr$_{0.4}$Co$_{0.2}$Fe$_{0.8}$O$_{3-\delta}$	Tubular	0.6**	/	1	CH$_4$: 1	840 – 1030	0.28	
[58]	La$_{0.9}$Ca$_{0.1}$FeO$_{3-\delta}$	Disk	1.3	/	0.02 - 1	CO: 0.01 – 0.1 H$_2$: 0.01 – 0.1	850 – 1030	0.38	106 h
[71]	La$_{0.9}$Ca$_{0.1}$FeO$_{3-\delta}$	Disk	1.3	20mol% CZO / LCaF-91 (feed) 20mol% (La$_{0.6}$Sr$_{0.4}$)$_{0.95}$ Co$_{0.2}$Fe$_{0.8}$O$_3$/LCaF-91 (sweep)	1	CH$_4$: 0.01 – 0.1	800 - 1030	0.5	/

Table 5 List of membrane materials for supporting CO_2 thermochemical reduction

Ref	Materials	Geometry	Thickness* [mm]	Catalyst	pCO$_2$ [atm]	pSweep† [atm]	T [°C]	Max CO production [μmol/cm^2•s]	Operation period
3. Mixed phase materials									
[72]	$Sm_{0.2}Ce_{0.8}O_{1.9}$ (+Ag)	Disk, with Ag circuit	(a) 1 mm (b) ~20 μm	Pt or Ag (feed), GdNi/Al$_2$O$_3$ (sweep)	0.125 – 0.5	CH$_4$: 0.027 – 0.135	750 – 900	1.6	100h.
[91]	$SrCo_{0.5}FeO_3$	Disk	2	/	0.2	CH$_4$: 0.444	760 – 940	0.25	30 h

* Numbers in the brackets are the porous layer thickness

** Total thickness and the porous layer thickness is not reported

†Numbers followed the gas species show the mole fractions of the fuels

Table 6 Membrane material preparation and stability

	Ref	Materials*	Powder synthesis	Green membrane preparation	Stability
1. Mixed phase materials					
	[72]	samarium-doped CeO_2 (+Ag)	SDC: sol-gel method	Press at ~150 MPa	Constant performance was observed with coke resistance (GdNi catalysts)
	[91]	$SrCo_{0.5}FeO_3$	Solid state reaction	Press at 150 MPa	Not stable. Pinhole and crack were found after 30 h hours operation under reactive flow
2. Single phase materials					
Fluorite	[80]	6 mol% Y_2O_3 - 94 mol% ZrO_2	/	/	/
	[26]	10 mol% CaO – 90 mol% ZrO_2	/	/	/
	[65]	CeO_2	/	Phase-inversion	Reported as stable under the specific experimental condition
Perovskite	[69] [82] [83]	$SrCo_{0.4}Fe_{0.5}Zr_{0.1}O_{3-\delta}$	Solid state reaction	Press at 200 MPa	$SrCO_3$, Co_2O_3 and Fe_2O_3 were found after experiments on surface
	[70]	3 wt% Al_2O_3-doped $SrCo_{0.8}Fe_{0.2}O_{3-\delta}$	Solid state reaction	Plastic extrusion (Catalyst by wet impregnation)	More stable than SCoFZ-451 membrane; $SrCO_3$ observed on the surface; membrane eroded by reducing gases, e.g., CH_4, CO and H_2

[68]	5 wt% Nb_2O_5-doped $SrCo_{0.8}Fe_{0.2}O_{3-\delta}$	Solid state reaction	Press at 400 MPa (Catalysts were sprayed on the dense membrane)	Bare membrane broke at 35 h. But with SBFMo-7391-SCoFNb-LSM-82 /YSZ triple –layer, the membrane ran stably for 500 h, and grain size increased slightly during experiments
[73]	$La_{0.6}Sr_{0.4}Co_{0.2}Fe_{0.8}O_{3-\delta}$	/	Phase-inversion	Amorphous graphite was detected by XRD
[58] [71]	$La_{0.9}Ca_{0.1}FeO_{3-\delta}$	/	/	Carbonates and oxides were found on the feed side surface, while sweep side surface was intact. Yet performance didn't degrade for 106 hours.

*Here only the dense membrane materials are shown. Information about porous layers on either side of the membrane and the operating conditions can be found in Table 5.

4. Chemical kinetics and flux models

As shown in Figure 2(b), there are generally five steps in a membrane supported CO_2 reduction process: two gas-phase diffusion (or gas phase reactive-diffusion in case of fuel sweep) steps and two surface reaction steps on the feed and sweep sides of the membrane, and one oxygen ion and electron bulk diffusion through the membrane. The CO_2 reduction rate per unit membrane surface area, $r_{CO_2,red}$, in [mol m^{-2} s^{-1}] is

$$r_{CO_2,red} = \frac{\dot{n}_{CO_2,in} - \dot{n}_{CO_2,out}}{A_{memb}} = \frac{\dot{n}_{CO,out}}{A_{memb}} \qquad (17)$$

where $\dot{n}_{CO_2,in}$, $\dot{n}_{CO_2,out}$ and $\dot{n}_{CO,out}$ are the molar flow rates of CO_2 at the inlet and outlet, and CO at the outlet of the feed side, respectively, in [mol s^{-1}]. From mass balance, the CO_2 reduction rate is proportional to the oxygen flux,

$$\left| r_{CO_2,red} \right| = 2 \left| J_{O_2} \right| = \left| J_V \right|. \qquad (18)$$

Here, J_{O_2} and J_V are the oxygen fluxes and oxygen vacancy fluxes through the membrane, respectively, in [mol m^{-2} s^{-1}]. At the meantime, the net current density inside the membrane is zero,

$$\sum_j Z_j F J_j = 0, \qquad (19)$$

where Z_j is the charge number, [dimensionless], F is the Faraday constant, [96485 s A mol^{-1}], and J is the flux, [mol m^{-2} s^{-1}].

As the oxygen flux across the membrane is an important rate descriptor of the process, in the following section, we first summarize bulk diffusion and surface reaction kinetics on feed and sweep sides. Next, the kinetics models will be discussed.

4.1 Bulk diffusion
4.1.1 Charged species

For an unpolarized membrane, the material should exhibit ionic and electronic conductivities, i.e., mixed conductivity. Charged species, e.g., lattice oxygen, electrons and/or holes diffuse across the membrane, driven by the chemical potential gradient as shown in Figure 2(b). For a single-phase membrane, there is often one dominant electronic charged species, either electrons or holes, and the membrane is either an *n*-type or *p*-type conductor [76, 140]. However, as it experiences a large oxygen partial pressure difference, e.g., fuel sweep that leads to low partial pressure on the sweep side, there may be a transition of the dominant electronic charged species across the membrane [141]. In order to estimate the bulk distribution of the charged species concentrations, defect reactions mechanisms are required. Here we use the Ca-doped LaFeO$_{3-\delta}$ as an example to illustrate the variation in charged species concentration under different oxygen partial pressures. The non-stoichiometric defect reactions for Ca-doped LaFeO$_{3-\delta}$ are

$$\frac{1}{2}O_2(g) + V_O^{\bullet\bullet} + 2Fe_{Fe}^x \leftrightarrow O_O^x + 2Fe_{Fe}^{\bullet} \tag{20}$$

$$2Fe_{Fe}^x \leftrightarrow Fe_{Fe}^{'} + Fe_{Fe}^{\bullet} \tag{21}$$

Here, the three iron states: $Fe_{Fe}^{'}$, Fe_{Fe}^x, $Fe_{Fe}^{\bullet}$, represent Fe^{2+}, Fe^{3+} and Fe^{4+}, respectively. The site conservation and electro-neutrality equations are,

$$\left[Fe_{Fe}^x\right] + \left[Fe_{Fe}^{'}\right] + \left[Fe_{Fe}^{\bullet}\right] = 1 \tag{22}$$

$$\left[Ca_{La}^{'}\right] + \left[Fe_{Fe}^{'}\right] = 2\left[V_O^{\bullet\bullet}\right] + \left[Fe_{Fe}^{\bullet}\right] \tag{23}$$

where $Ca_{La}^{'}$ is the calcium dopant in a lattice lanthanum site in $LaFeO_{3-\delta}$.

Geary and Adler [142] used coulometric titration cell to derive the equilibrium oxygen nonstoichiometry and charged species concentration based on the current response. Figure 12 shows the charged species concentrations at equilibrium for LCaF-91 at 990ºC calculated based on the parameters reported in [142]. Electron holes dominate the electronic conduction at high oxygen partial pressure, while electrons dominate at low oxygen partial pressures. In other words, the membrane is a *p*-type conductor on the high oxygen partial pressure side, and an *n*-type conductor on the low oxygen partial pressure side. The intrinsic region with the least concentration of electronic charged species is located where $n = p$ when the partial pressure of oxygen is around 10^{-9} atm.
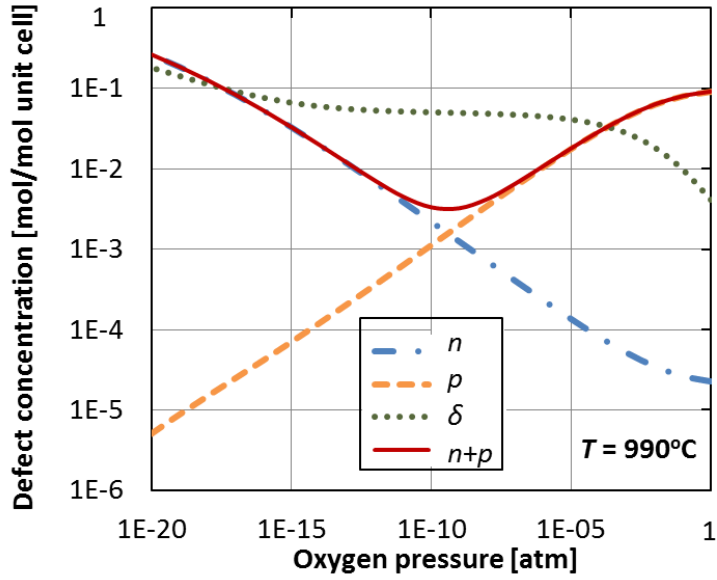
Figure 12 Charged species in LCaF-91 materials under the equilibrium case at 990ºC with oxygen partial pressure increased from 10^{-20} to 1 atm (calculated using the parameters from [142]) $n = Fe'_{Fe}, p = Fe^{\square}_{Fe}$

4.1.2 Conductivity

The total conductivity of a mixed ionic and electronic conductor is,

$$\sigma_{tot} = \sum_j \sigma_j = \sum_j n_j q \mu_j \qquad (24).$$

where σ_j is the conductivity of species j, in [S m^{-1}], n_j is the carrier j density, in [m^{-3}], q is charge of species j in [C], and μ_j is its mobility in [m^2 V^{-1} s^{-1}]. These conductivities depend on temperature and oxygen partial pressure. For example, the ionic conductivity can be described using the Nernst-Einstein relation according to [143]

$$\sigma_i = \frac{4F^2 \left[V_O^{\bullet\bullet} \right] D_V}{RTV_m}, \qquad (25)$$

where $\left[V_O^{\bullet\bullet} \right] = \delta$ the nonstoichiometry of the oxygen vacancy, [dimensionless], D_V the diffusivity of oxygen vacancies, in [m^2 s^{-1}], R the universal gas constant, [8.314 J mol^{-1} K^{-1}], T is temperature, in [K], and V_m is the molar volume, in [m^3 mol^{-1}]. Both $\left[V_O^{\bullet\bullet} \right]$ and D_V depend on the temperature and oxygen partial pressure, as shown in Figure 12 and Figure 13, respectively. The ionic conductivity is simplified according to

$$\sigma_i(T) = \sigma_i^o(T) P_{O_2}^{-n}, \tag{26}$$

where $\sigma_i^o(T)$ is the ionic conductivity at 1 atm oxygen partial pressure and temperature, which can be written in the Arrhenius form.

Similarly, the electronic conductivity can be written as,

$$\sigma_e(T) = \sigma_e^o(T) P_{O_2}^{-n}. \tag{27}$$

where $\sigma_e^o(T)$ is the electronic conductivity at 1 atm oxygen partial pressure and temperature. More complex models for the electronic and ionic conductivities can be found in [54] and references therein.
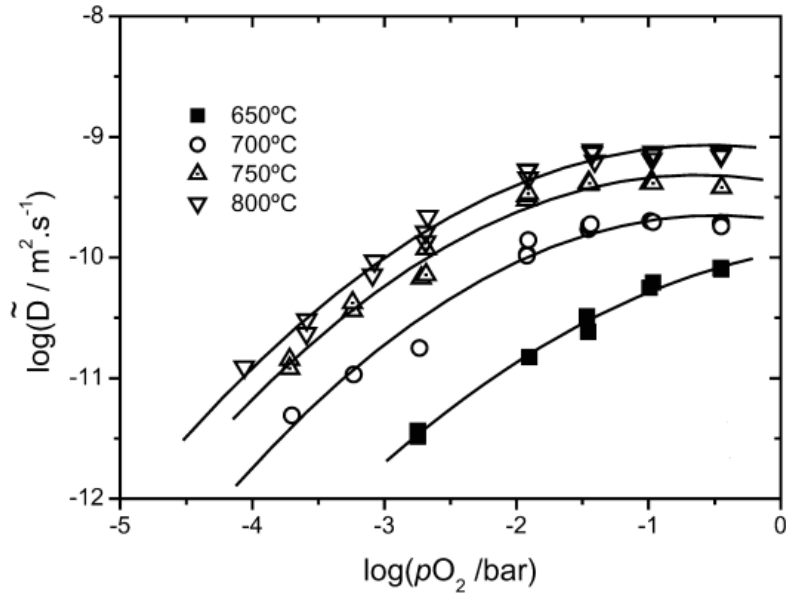
Figure 13 The oxygen vacancy diffusivity of $La_{0.6}Sr_{0.4}Co_{0.2}Fe_{0.8}O_{3-\delta}$ as a function of oxygen partial pressure and temperature (Reprinted from [144] with permission of Springer Nature)

The total conductivity and ionic conductivity of typical oxygen permeable membranes are shown in Figure 14. Most of these values were measured in air ($P_{O2} = 0.21$ atm). The conductivity changes by orders of magnitude between different mixed ionic-electronic conductors. Yet, generally, ionic conductivity is much lower than electronic conductivity in perovskites, while the gadolinium doped ceria (CGO20) and mixed phase $SrFeCo_{0.5}O_x$ exhibit mainly ionic conductivity. To fabricate MIEC materials with desired

conductivity, dopants are added to a single-phase material, or materials with different phases are mixed. Conductivity can affect the surface reactions if any of the steps involve charge transfer.
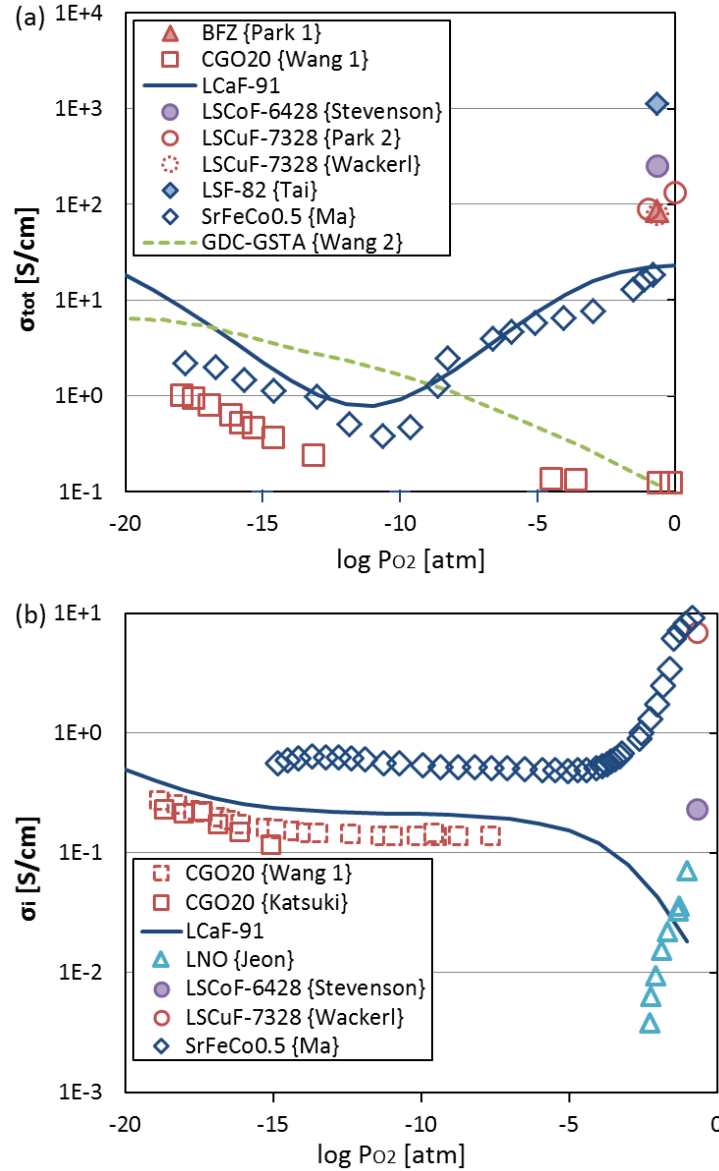
Figure 14 (a) Total conductivities and (b) ionic conductivities of different membrane materials at 900ºC under different oxygen partial pressures (Ref: BFZ{Park 1 [111]}; CGO20 {Wang 1 [145], Katsuki [146]}; LCaF-91 {calculated from (25)}; LNO {Jeon [102]}; LSCoF-6428 {Stevenson [147]}; LSCuF-7328 {Park 2 [148], Wackerl [149]}; LSF-82 {Tai [150]}; SrFeCo$_{0.5-x}$ {Ma [151]}; GDC-GSTA {Wang 2 [152]})

4.2 Surface reaction kinetics

Although many studies have been conducted for membrane-supported CO_2 reduction, surface reaction mechanisms and kinetics are yet to be fully characterized. In addition, the CO_2 reduction mechanisms for the two thermochemical reduction methods (i.e., chemical looping and membrane supported reduction) as both involve the gas-solid heterogeneous reaction between the CO_2 and the oxide.

Oxygen-containing molecules such as H_2O and CO_2 were found to react with the oxygen vacancies, similar to the interaction between oxygen gas and vacancies [85, 153, 154]. Several multi-step mechanisms have been proposed for CO_2 reduction. Argirusis et al [155] proposed a two-step CO_2 decomposition reaction mechanism on a clean Fe-doped $SrTiO_3$ single crystal surface:

$$CO_2(g) \leftrightarrow CO(g) + O_{ads}^{-} + h^{\bullet} \tag{28}$$

$$O_{ads}^{-} + V_O^{\bullet\bullet} \Leftrightarrow O_O^{x} + h^{\bullet} \tag{29}$$

Here $h^{\bullet}$ is the electron hole (or more precisely the net charge in the lattice iron) and O_{ads}^{-} is the adsorbed oxygen species on the perovskite surface.
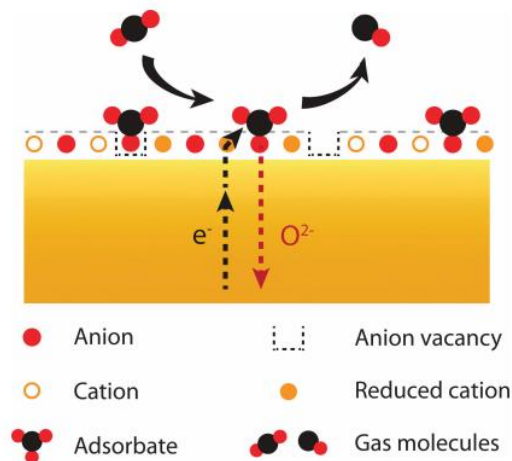
Figure 15 Schematic of the oxygen-ion incorporation pathway on the surface of a mixed ion-electron conducting material (Reprinted from [156] with permission of the PCCP Owner Societies)

Feng et al. [156] proposed a four-step CO_2 reduction mechanism on mixed conducting SDC surface, coupling the charge transfer and the carbonate formation, and considering the species diffusion between the bulk to the surface. In this four-step mechanism, two steps are involved for the interactions between the membrane surface and

CO_2 (as shown in Figure 15): (i) CO_2 reacts with the membrane to form a thin layer of carbonate and (ii) the carbonate decomposes with electron transfer and oxygen incorporate to form CO:

$$CO_{2(g)} + O_{O,s}^{\times} + Ce_{Ce,s}^{'} \ \square \ \left(CO_3\right)_{O,s}^{'} + Ce_{Ce,s}^{\times} \tag{30}$$

$$\left(CO_3\right)_{O,s}^{'} + Ce_{Ce,s}^{'} + V_{O,s}^{\bullet\bullet} \ \square \ CO_{(g)} + 2O_{O,s}^{\times} + Ce_{Ce,s}^{\times} \tag{31}$$
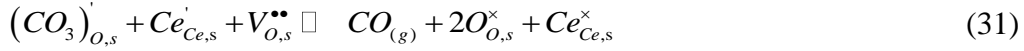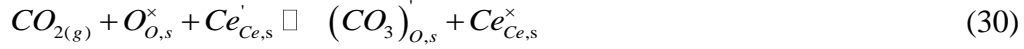
where the subscript 's' denotes surface species of ceria. The other two steps are the charged species exchange between the bulk and the surface in ceria, as

$$2\left(Ce_{Ce,b}^{'} \ \square \ Ce_{Ce,s}^{'}\right) \tag{32}$$

$$V_{O,b}^{\bullet\bullet} \ \square \ V_{O,s}^{\bullet\bullet}. \tag{33}$$

Either monodentate or bidentate carbonates can form on an oxide surface. The former occurs when CO_2 adsorbs on a surface lattice oxygen [157], while the later takes place between CO_2 and a pair of surface sites, i.e., a lattice oxygen and an oxygen vacancy [158]. If the carbonate decomposes, as in reaction (31), CO will be produced. This is observed on $LaFeO_3$ surface using TPD; and the more reduced the surface is, the more CO desorption is observed [158]. However, if the carbonates do not decompose, they may cover the surface and stop further reactions. This is related to membrane instability discussed earlier.

A similar reaction mechanism involving carbonate formation as a sub-step is hypothesized by Voigt et al. [159] based on the experimental results on a sputtered Fe-doped $SrTiO_3$ single crystal surface:

$$2CO_2 + V_O^{\bullet\bullet} + Ti\,''_{Ti} \rightarrow \left(CO_3\right)_O^X + Ti_{Ti}^X + CO \tag{34}$$

or

$$CO_2 + Ti\,''_{Ti} + O_O^X + 2h^{\bullet} \rightarrow \left(CO_3\right)_O^X + Ti_{Ti}^X \tag{35}$$
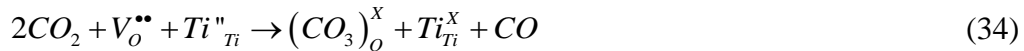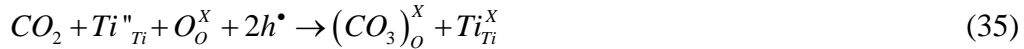
Here $Ti\,''_{Ti}$ and Ti_{Ti}^X are titanium with +2 and +4 valences, respectively. $\left(CO_3\right)_O^X$ is the carbonate occupying an oxygen site.

CO_2 reduction on an MIEC, especially on a mixed phase membrane, can also be modeled similarly to the reaction on a triple phase boundary between Ni catalysts and YSZ electrolyte in a solid oxide electrolysis cell, where the reactions can be written as [160, 161]

$$CO_2(\text{Ni}) + (\text{YSZ}) + 2\,\text{e'} \leftrightarrow CO(Ni) + O^{2-}(YSZ) \tag{36}$$

$$CO(\text{Ni}) + (\text{YSZ}) + 2\,\text{e}' \leftrightarrow C(Ni) + O^{2-}(YSZ) \tag{37}$$
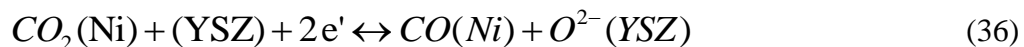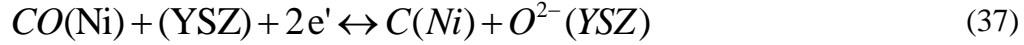
These two reactions are related with charge transfer and occurs once a current is introduced in the electrolysis cell. The rates are written in Arrhenius form [160, 161]. Experiments showed that the carbon deposition reaction in an electrolysis cell is significantly facilitated with the value of the overpotential, and hence, the cell should operate at lower overpotential to decrease carbon deposition on the triple phase boundary between Ni and YSZ [161].

4.3 Kinetics model

Based on the bulk diffusion and surface reaction kinetics models described above, expressions have been developed to express the dependency of the permeation process for oxygen separation, water splitting and CO_2 reduction on the operating conditions. A recent review covers most of the oxygen permeation models for MIEC oxygen permeable membranes [162] where the derivation of these models can be found. In this review, we focus on how to apply these models to describe the CO_2 reduction process. We first describe the mass diffusion in the gas phase and in the solid phase. Then a simplified model for bulk-limiting and a generalized model considering both bulk diffusion and surface reactions are discussed for CO_2 reduction.

In the gas phase diffusion steps, the flux without gas phase reactions, J_j, [mol m^{-2} s^{-1}], is modeled as,

$$J_j^i = h_{m,j}^i \left(C_{b,j}^i - C_{s,j}^i \right) \tag{38}$$

where h_m is mass transfer coefficient, [m s^{-1}], C is the concentration, [mol m^{-3}]. The superscript i is either feed or sweep side. Subscripts b and s represent the gas bulk and surface properties, respectively. The mass transfer coefficient in the gas phase can be calculated from Sherwood number correlations [163] and the species diffusion coefficients [164]. In cases where the gas phase reactions cannot be neglected, such as methane sweep cases, the concentration difference between the gas near and away from the membrane surface can be more significant; the gas phase reactive-diffusion should be considered. In experiments, a capillary probe can be inserted into the reactor to sample the gas species in vicinity of the surface [59, 71, 117-119], as described earlier in section 3.2.3.

The diffusion of charged species in the solid phase can be described by the Nernst-Planck equation [165],

$$J_i = -\frac{\sigma_i}{\left(Z_i F\right)^2}\nabla\tilde{\mu}_i + C_i v \tag{39}$$

where σ is the conductivity [S m^{-1}], Z is the number of charges, [dimensionless], $\tilde{\mu}$ is the electrochemical potential [J mol^{-1}], C is the concentration [mol m^{-3}], v is the convective velocity [m s^{-1}], and the subscript i denotes the charged species i.

For an isothermal 1D stationary system, equation (39) becomes [165]

$$J_i = -\frac{\sigma_i}{\left(Z_i F\right)^2}\left(\frac{d\mu_i}{dx} + Z_i F\frac{d\varphi}{dx}\right) \tag{40}$$

where the electrochemical potential μ_i is the chemical potential, [J mol^{-1}] and φ is electric field, [V].

In the unpolarized membrane configuration, the net current density is zero. Hence,

$$i_{tot} = \sum_j Z_j F J_j = -\sum_j \frac{\sigma_{tot}\cdot t_j}{Z_j F}\left(\frac{d\mu_j}{dx} + Z_j F\frac{d\varphi}{dx}\right) = 0 \tag{41}$$

where t_j is the transference number, [dimensionless]. It is defined as the conductivity of species j over the total conductivity of the system,

$$t_j = \frac{\sigma_j}{\sigma_{tot}} = \frac{\sigma_j}{\sum_k \sigma_k} \tag{42}$$

From (40), (41) and (42), we get

$$J_i = -\frac{\sigma_{tot}\cdot t_i}{\left(Z_i F\right)^2}\left(\frac{d\mu_i}{dx} - Z_i\sum_j\left(\frac{t_j}{Z_j}\cdot\frac{d\mu_j}{dx}\right)\right), \tag{43}$$

which describes the flux in one-dimensional. When the membrane is thick and bulk diffusion is the rate-limiting step, equation (43) can be used to approximate the oxygen permeation. Hence, a critical thickness, t_c, is defined to identify whether the flux across the membrane is surface or transport-limited. In the following, we first describe the oxygen permeation model in the latter case, with either electrons or electron holes as the dominating electronic charged species. Next, a more general oxygen flux model is derived, considering both bulk diffusion and surface reaction kinetics.

In order to select the correct model for oxygen permeation, experiments are performed to parametrize the kinetics of surface reactions and bulk diffusion and compare their significance. Wu and Ghoniem [58] carried out a detailed reaction kinetics study on the LCaF-91 membrane supported CO_2 reduction and compared the resistances of the surface reactions and bulk diffusion. They found that a 1-mm thick LCaF-91 membrane, the rate-limiting step transitions from the feed side CO_2 reduction kinetics to the sweep side fuel oxidation reaction kinetics at higher temperatures, as shown in Figure 16.
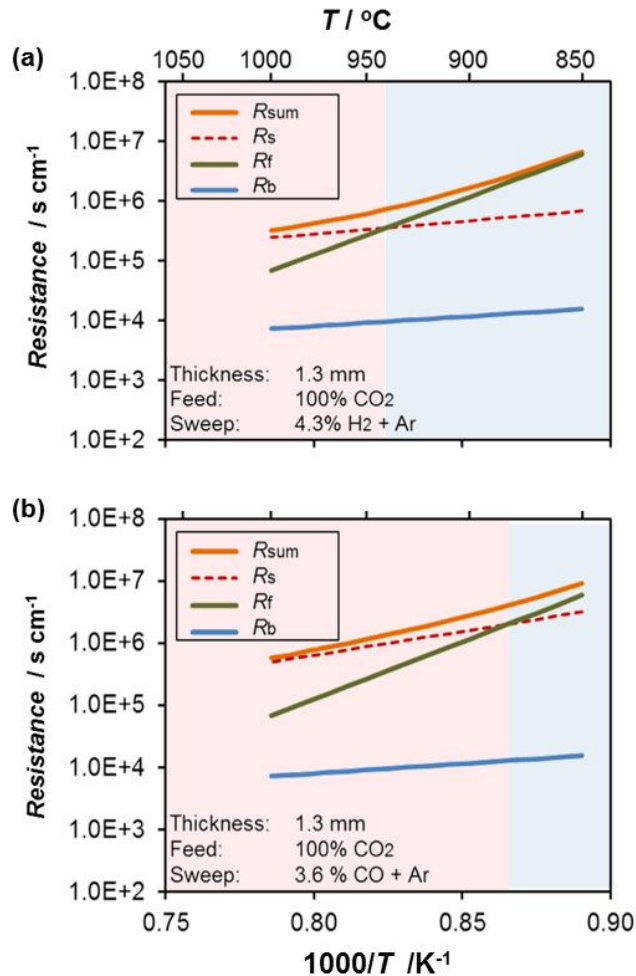
Figure 16 The comparison among the resistance values for the (a) H_2 and (b) CO sweep cases for the 1.3 mm thick LCaF-91 membrane supported CO_2 reduction with 4.3% H_2 or 3.6% CO (balanced with Ar). R_f, R_b, R_s and R_{sum} are the resistances of the feed side CO_2 reduction reaction, the bulk diffusion, the sweep side fuel oxidation and their sum, respectively. (Reprinted from [58] with permission of John Wiley and Sons)

56

4.3.1 Bulk-diffusion limiting

When oxygen permeation is bulk-diffusion limited, we can assume quasi-equilibrium reactions on the surface. In the case that the membrane conducts only electrons and oxygen ions (similar results can be derived for electron hole conductors), the ionic flux in the case of air-feed-inert-sweep becomes: [166]

$$J_i = -\frac{\sigma_{tot} t_i t_e}{2(Z_i F)^2} \frac{d\mu_{O_2}}{dx} = \frac{RT}{(4F)^2 t} \int_{P''_{O_2}}^{P'_{O_2}} \sigma_{tot} t_i t_e \, d\ln P_{O_2} \tag{44}$$

where t is the thickness of the membrane, [m].

For materials in which the electronic conductivity is much higher than the ionic conductivity and assuming the ionic conductivity can be described as constant ($\bar{\sigma}_i$) across the membrane, (44) is simplified to: [167]

$$J_{O_2} = \frac{\bar{\sigma}_i RT}{(4F)^2} \ln\frac{P'_{O_2}}{P''_{O_2}} \tag{45}$$

Similarly, for the case of water splitting with hydrogen sweep, or CO_2 reduction with CO as the sweep gas, assuming the surface reaction is at equilibrium, we have

$$J_i = \frac{RT}{(Z_i F)^2 t} \sigma_{tot} t_i \left(\ln\frac{P'_{H_2O}}{P''_{H_2O}} - \ln\frac{P'_{H_2}}{P''_{H_2}} \right) \tag{46}$$

and

$$J_i = \frac{RT}{(Z_i F)^2 t} \sigma_{tot} t_i \left(\ln\frac{P'_{CO_2}}{P''_{CO_2}} - \ln\frac{P'_{CO}}{P''_{CO}} \right) \tag{47}$$

For fluorites, electron diffusion is typically the limiting rate, and the oxygen flux can be calculated as [34]

$$J_{O_2} = \frac{kT}{4qFt} \sigma_e^0 \exp\left(-\frac{\Delta E_e}{kT}\right) \left(P''^{-1/4}_{O_2} - P'^{-1/4}_{O_2} \right) \tag{48}$$

where k is the Boltzmann constant, $[1.38 \times 10^{-23}$ m^2 kg s^{-2} K$^{-1}]$, q the electron charge, [C], and σ_e^0 and ΔE_e are the pre-exponential constant and activation energy for electron conductivity, respectively.

4.3.2 Generalized transport model

For the cases when the surface reaction rates should be considered, Xu and Thomson [140] developed a generalized oxygen transport model for air separation considering two gas/solid reactions on both surfaces and one oxygen ion bulk diffusion, based on the theoretical model from Lin et al. [167]. Later, Wu and Ghoniem extended this model to other oxygen sources such as H$_2$O [59, 168] and CO$_2$ [58, 71]. Here, we will summarize the case with CO$_2$ reduction. For other cases of membrane supported air separation and water splitting, more detail can be found in [59, 140, 162, 168].

One-step reaction is used to describe the surface reactions. On the feed side,

$$CO_2 + V_O^{\bullet\bullet} \xrightarrow{k_{f,CO_2}/k_{r,CO_2}} O_O^x + 2h^\bullet + CO \tag{49}$$
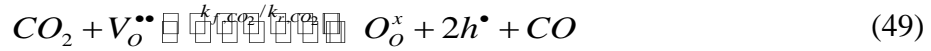
On the sweep side, depending on the sweeping condition, the oxygen evolution or Mars-van Krevelen (MvK) mechanism are used for inert sweep or methane sweep, respectively:

Inert sweep: $$O_O^x + 2h^\bullet \xrightarrow{k_{f,O_2}/k_{r,O_2}} \frac{1}{2}O_2 + V_O^{\bullet\bullet} \tag{50}$$

CH$_4$ sweep: $$O_O^x + 2h^\bullet + CH_4 \xrightarrow{k_{f,CH_4}/k_{r,CH_4}} CO + 2H_2 + V_O^{\bullet\bullet} \tag{51}$$
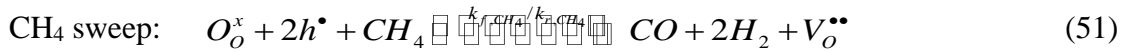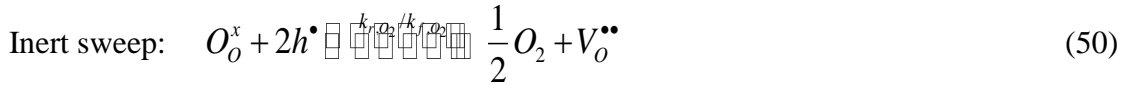
Several assumptions are made to simplify the permeation model:
(1) The backwards reactions are neglected due to the low oxygen flux compared to the total flow rate and hence the low product concentrations compared to the reactants;
(2) Electron hole concentration across the membrane is assumed to be constant as the electronic transference number is much higher than ionic transference number [169, 170]. Therefore, the vacancy flux is viewed as zero-order in electron hole concentrations [140, 171].
(3) The total site concentration for oxygen species C_o is

$$C_O = C_{O_O^x} + C_V \tag{52}$$

where $C_{O_O^x}$ and C_V are the concentrations of lattice oxygen and oxygen vacancies, respectively, [mol m^{-3}]. C_o is assumed to be a constant value (for example, the value is

0.0825 mol cm^{-3}, estimated from the XRD measurements of the stoichiometric LCaF-91 lattice size in air [172]).

Based on these assumptions, the vacancy fluxes are:

Feed side:

$$J'_V = k_{f,CO_2} C'_{CO_2} C'_V \tag{53}$$

Sweep side:

Inert: $$J''_V = \tilde{k}_{r,O_2} \left(C_O - C''_V \right) - k_{f,O_2} C''^{0.5}_{O_2} C''_V \tag{54}$$

CH$_4$: $$J''_V = \tilde{k}_{f,CH_4} C''_{CH_4} \left(C''_O - C''_V \right) \tag{55}$$

Here, J'_V and J''_V are the absolute values of oxygen vacancy fluxes on the feed and sweep side surfaces, respectively, [mol m^{-2} s^{-1}]; C'_i and C''_i are the concentrations of species i on the feed side and sweep side, respectively, [mol m^{-3}]; $\tilde{k}$ is the new reaction constant after lumping the electron hole concentration.

For the oxygen vacancy diffusion flux as in (43), when the ionic conductivity is the limiting step for the bulk diffusion, we obtain the oxygen vacancy diffusion rate in the bulk:

$$J_V = -D_V \frac{\partial C_V}{\partial y} = D_V \frac{C''_V - C'_V}{t} . \tag{56}$$

By equating the oxygen vacancy flux on the feed side surface, (53), through the bulk, (56) and on the sweep side surface, (54) or (55), the flux equation is expressed in the form of the potential difference over the sum of three resistances as [140, 167]

$$J_V = \frac{\Delta P}{R_f + R_b + R_s} \ or \ \frac{C_O}{R_f + R_b + R_s} , \tag{57}$$

where ΔP is the potential difference, [mol m^{-3}], R_f, R_b and R_s are the resistances of the feed-side surface reaction, the bulk diffusion and the sweep-side surface reaction, respectively, [s m^{-1}]. A schematic of resistance network is shown Figure 17, and the resistances under various feed and sweep conditions are summarized in Table 7. Similarly, in cases where a tubular membrane is used, the local oxygen flux can be calculated with respect to the log-mean membrane area, $dA_m = 2\pi r_m dl$ or to the inner surface of the membrane. In the first case, the log-mean radius is used to calculate the log-mean membrane area,

$$r_m = (r_o - r_i) / \ln(r_o - r_i) \tag{58}$$

where r_i and r_o are the inner and outer radius of the tubular membrane, [m] [173]. For the latter case, the resistance equations with respect to the inner surface area is summarized in Table 7 for the oxygen flux per unit length of a tubular membrane.

More elaborate models have been developed to incorporate multi-step surface reaction mechanisms and different charged species diffusions, and used to back out kinetics parameters by fitting model predictions to experimental measurements. These higher fidelity models are useful when modeling membranes subject to a large oxygen partial pressure difference, in which both electronic and ionic conductivity could be on the same order of magnitude and kinetics mechanism must consider all the charged species, e.g., electrons, holes or polarons. For example, Dimitrakopoulos and Ghoniem [60, 141] developed a detailed oxygen permeation model for oxygen production on $La_{0.9}Ca_{0.1}FeO_{3-\delta}$ membranes using a two-step oxygen incorporation reaction mechanism on the surface,

$$\frac{1}{2}O_2 + V_O^{\bullet\bullet} + 2Fe_{Fe}^{\times} \leftrightarrow O_O^{\times} + 2Fe_{Fe}^{\bullet} \tag{59}$$
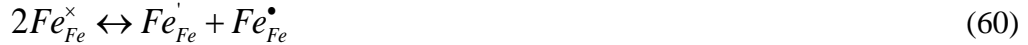
$$2Fe_{Fe}^{\times} \leftrightarrow Fe_{Fe}^{'} + Fe_{Fe}^{\bullet} \tag{60}$$

In the above reactions, $Fe_{Fe}^{'}$, $Fe_{Fe}^{\times}$ and $Fe_{Fe}^{\bullet}$ are the different iron oxidation states, Fe^{2+}, Fe^{3+} and Fe^{4+} in the iron lattice site, respectively. For the charged species diffusion in the membrane, the Planck-Nernst-Poisson (PNP) model is used with the conservation equations of the species and a Poisson equation for the electrostatic potential, as

$$\frac{\partial C_k}{\partial \tau} + \nabla \cdot J_k = 0 \tag{61}$$

where C_k is the molar concentration of species k, [mol m^{-3}], τ is the time, [s], and J_k is the flux of charged species, k, which is given by

$$J_k = -D_k \left(\nabla C_k + \frac{Z_k F}{RT} C_k \nabla \varphi \right) \tag{62}$$

Here, D_k is the diffusion coefficient, [m^2 s^{-1}] and φ is the electrostatic field, [V]. The electrostatic potential is related to the local charge density ρ through the Poisson equation,

$$\nabla \cdot (\varepsilon_r \varepsilon_o \nabla \varphi) = -\rho = -F \sum_{k=1}^{N} (Z_k C_k). \tag{63}$$

where ε_r and ε_o are the relative and vacuum permitivities, respectively, [F m^{-1}]. The local charge density, ρ, is a summation of molar concentrations of both mobile and fixed charged species in the lattice of the membrane, [C m^{-3}]. The PNP model can describe the oxygen permeation in a mixed conducting membrane with multiple charged species [60, 141]. When the charged species in a mixed conductor changes over the oxygen partial pressure (shown in Figure 12), this model can describe the process accurately. This should be even more critical in the case of mixed phase materials where the electronic and ionic conductivity are on similar order of magnitude. Incorporating detailed CO_2 reduction mechanisms into these higher-fidelity transport models has not been attempted yet.
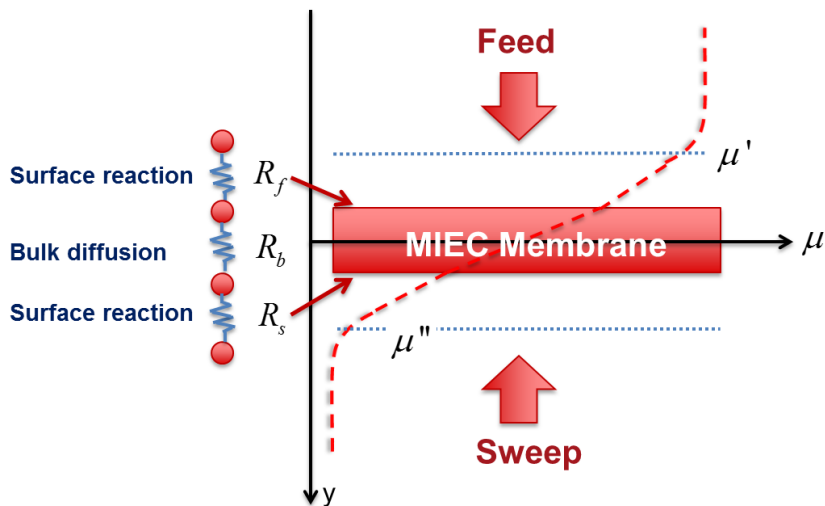
Figure 17. A three-resistance model for oxygen permeation through an inorganic membrane. Feed and sweep sides are at high and low potential, μ' and μ'', respectively (Modified from [168] with permission of the PCCP Owner Societies)

Table 7 Resistance network for membrane-supported CO_2 reduction with various sweep-side mechanisms on an MIEC oxygen permeable membrane [59, 168]

Oxygen source	CO_2

Sweep side mechanism	Inert sweep	Fuel-sweep	Fuel-sweep (tubular)*
ΔP or C_O	$\dfrac{\tilde{k}_{r,o} C_o}{\tilde{k}_{r,o} + k_{f,o} C''^{0.5}_{O_2}}$	C_0	$\dfrac{2C_O}{r_i}$
Surface reaction resistance (feed side), R_f	$\dfrac{1}{k_{f,CO_2} C'_{CO_2}}$		$\dfrac{1}{r_i k_{f,H_2O} C'_{H_2O}}$
Bulk resistance, R_b	$\dfrac{t}{D_V}$		$\dfrac{\ln(r_o/r_i)}{D_V}$
Surface reaction resistance (sweep side), R_s	$\dfrac{1}{\tilde{k}_{r,o} + k_{f,o} C''^{0.5}_{O_2}}$	$\dfrac{1}{\tilde{k}_{fuel} C''_{fuel}}$	$\dfrac{1}{r_o \tilde{k}_{f,CH_4} C''_{CH_4}}$

Here, $k_{f,O}$ and $\tilde{k}_{r,O}$ are the forward and reverse reaction rates for $\frac{1}{2}O_2 + V_O^{\bullet\bullet} \overset{k_{f,O}}{\underset{\tilde{k}_{r,O}}{\rightleftharpoons}} O_O^x + 2h^{\bullet}$, respectively [168]. k_{f,CO_2} is the rate constant for the CO_2 reduction reaction, and $\tilde{k}_{fuel}$ is for fuel oxidation [58]. And r_i and r_o are the inner and outer radiuses of the tubular membrane.

*The oxygen flux per length, [mol m^{-1} s^{-1}] is shown, which is evaluated based on the inner tube surface area

5. CO$_2$-to-fuel systems

As discussed earlier in this review, this membrane process can convert CO$_2$ into CO using thermal energy and chemical potential gradients. A promising application is solar-fuel production in which concentrated solar energy is integrated with a membrane reactor supporting CO$_2$ reduction. The full spectrum solar irradiance can be utilized as the thermal energy input. Kogan [36] designed a porous zirconia membrane reactor integrated with a solar receiver for water splitting, while similar reactor layout is applicable for CO$_2$ reduction. This system is based on two concentrators (as shown in Figure 18) to achieve a radiation concentration of the order of 10,000 and a reactor wall temperature reaching 2250K. Other components were made of ZrO$_2$ and MgO to maintain mechanical and thermal stability at elevated temperatures (the melting points of ZrO$_2$ and MgO are 2715 and 2800°C, respectively).

Three ways to integrate concentrated solar irradiance with a membrane reactor are shown in Figure 19. The first shows solar irradiance directly shining onto the membrane surface, which requires a transparent but also gas tight enclosure [65, 174] . In the second, solar irradiance is adsorbed by the entrance wall, making the reactor shorter to maintain high operating temperatures along the membrane surfaces [175]. The third option shows separation between the heating system and the membrane reactor, where the solar heat is

adsorbed by a heat exchanger to heat up the input gases. In this option, existing solar thermal heating systems can be used and the membrane reactor can be optimized separately. Additionally, electricity from photovoltaics (PVs) or other sources can also be used to generate the elevated operating temperatures by direct resistive heating, similar to the case in a solid oxide electrolysis cells where heat is supplied by internal Joule heating and/or additional resistive heating [176].

On the other hand, as mentioned in Table 3, the two sides of the membrane can operate at different pressures to maximize the chemical potential gradients or to integrate with downstream processes. Pressurized feed side [177, 178] or vacuum sweep side [179] can enhance oxygen permeation rates. A large scale membrane system with pressurized feed side for over 16 tons/day of oxygen production was demonstrated by Air Products and Ceramatec, and robust support layers were added on the thin membrane layer to withstand the high pressure difference [180]. Fraunhofer Institute for Ceramic Technologies and Systems built a pilot plant for pure oxygen production with vacuum sweep; the oxygen production is 10 m^3 (STP) O_2/h (0.34 tons/day), and the energy demand is 0.72 kWh/m^3 (STP) O_2 [181]. Another process developed by Praxair used high pressure fuel sweep to integrate with coal and natural gas power cycles with CCS [182]. Similar membrane systems can be used for CO_2 reduction.

In order to evaluate these different operation options, parametric studies should be conducted to investigate the rate dependence on the operating conditions (e.g., the flow rates, CO_2 concentration and sweep side condition), and the membrane characteristics (e.g., thickness, porous support and catalysts). So far, there have not been many studies on the system optimization and reactor design for CO_2 or H_2O reduction systems.
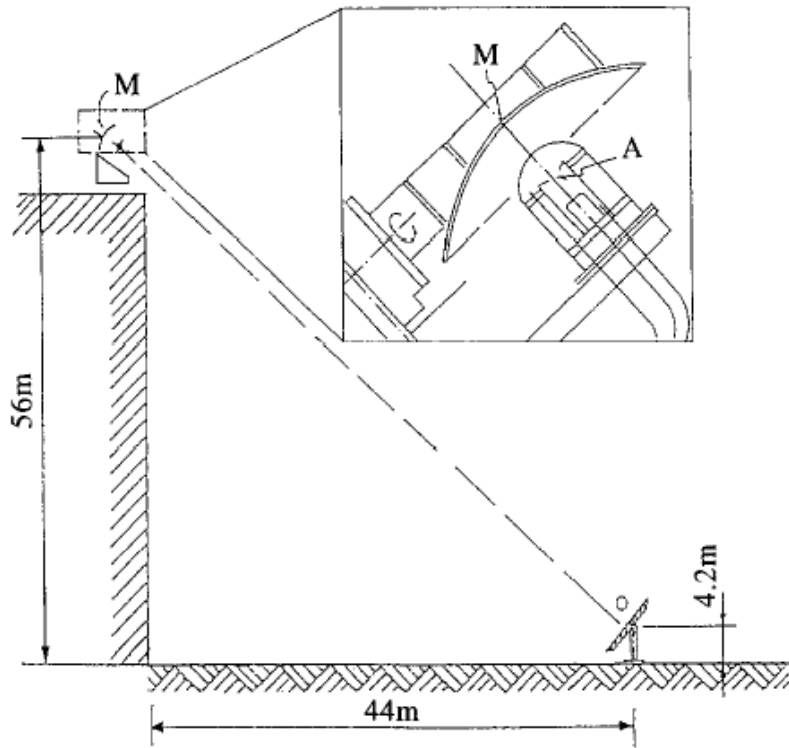
Figure 18 Heliostat, secondary concentrator-reactor configuration proposed by Kogan
(M: mirror, A: Aperture) (Reprinted from [36] with permission of Elsevier)
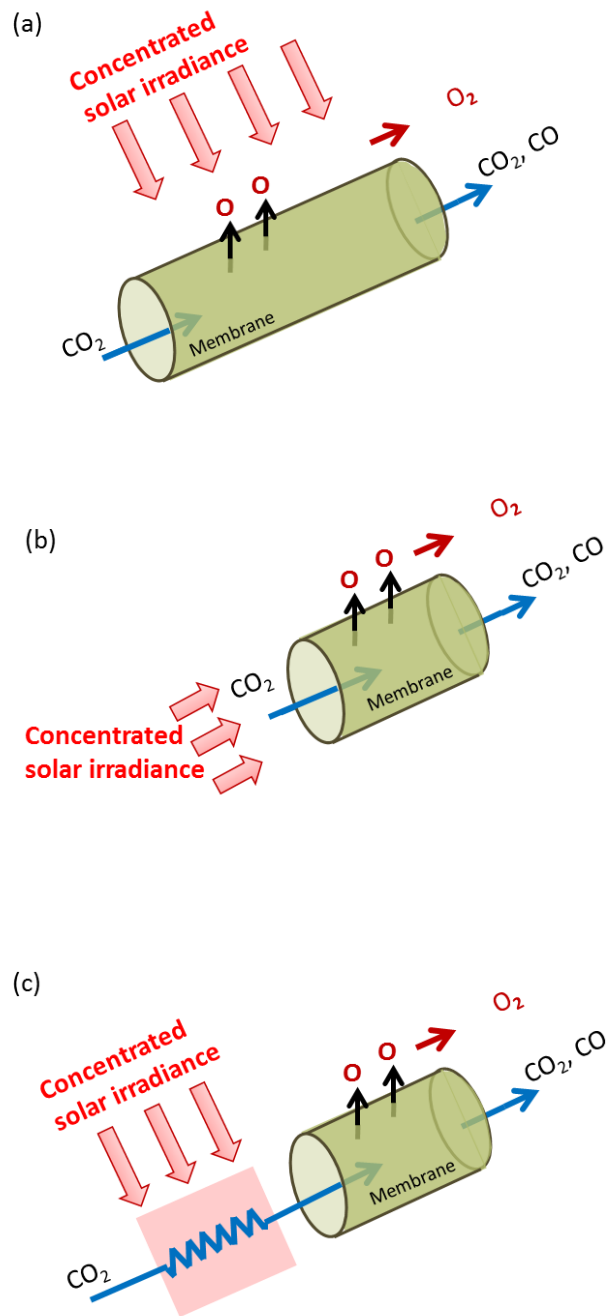
Figure 19 Schematic representations of the integration of concentrated solar irradiation and membrane reactors: (a) The concentrated solar irradiance directly heats the membrane surface [65, 174]. (b) The solar irradiance heats the entrance wall of the membrane reactor [175]. (c) The solar irradiance heats the gas input through a heat exchanger. (A tubular membrane with vacuum sweep is used as an example, but other types of membrane reactors and operating modes can be integrated in a similar manner)

Wang et al. [183] analyzed a membrane-supported water splitting system based on the LSCoF-6428 membranes, and the kinetics were obtained from oxygen permeation results reported in [140]. Depending on the sweep conditions as shown in Figure 2(a), the solar-fuel efficiency, η, of the membrane reactor based on primary energy input is defined as

Vacuum pump or inert gas sweep:

$$\eta = \frac{\sum \dot{n}_{products} \cdot HHV_{products}}{\sum \dot{Q}_{in} + \sum \dot{W} \Big/ \eta_e} \qquad (64)$$

Fuel sweep:

$$\eta = \frac{\sum \dot{n}_{products} \cdot HHV_{products}}{\sum \dot{Q}_{in} + \sum \dot{W} \Big/ \eta_e + \sum \dot{n}_{fuel} \cdot HHV_{fuels}} \qquad (65)$$

where HHV is the higher heating values, [J mol^{-1}], $\dot{n}$ is the molar flow rate, [mol s^{-1}], $\dot{Q}_{in}$ and $\dot{W}$ are the thermal energy and work inputs, [W], and η_e is the efficiency used to convert primary energy into electricity (or solar energy to electricity), [dimensionless]. The energy inputs include the sensible heats of the reacting gases, the enthalpy of reactions, the pump and compressor work, and the separation work in the condenser. The required heat input is divided by the absorption efficiency of the solar cavity receiver, η_{abs}, to obtain the solar heat input. The absorption efficiency of the solar cavity receiver is a function of temperature and concentration level, estimated as a blackbody absorber:

$$\eta_{abs} = 1 - \frac{\sigma \cdot T_H^4}{I \cdot C_{receiver}}, \qquad (66)$$

where σ is the Stefan-Boltzmann constant, [5.670367×10^{-8} kg s^{-3} K^{-4}], T_H is the reactor temperature, [K], I is the solar irradiation on the Earth's surface, set to be 10^3 [W m^{-2}], and $C_{receiver}$ is the concentration level of the receiver, [dimensionless]. For η_e, the efficiency of solar energy to electricity, values around 15% were used. Results show that higher solar-to-fuel efficiency around 89% could be achieved with methane sweep, while the vacuum pump-sweep nonreactive process had an efficiency lower than 20% [183].

A similar analysis comparing different sweep conditions for membrane-supported CO$_2$ reduction was performed by Zhu et al. [174], where they compared a tubular ceria membrane at 1800K with either pump-driven or inert (N$_2$) sweep O$_2$ production. Heat

recovery from the hot gas was considered, and set to be 95%, and η_e was taken to be 40%. The efficiency was defined as

$$\eta = \frac{\sum \dot{n}_{products} \cdot HHV_{products} - \sum \dot{W} \Big/ \eta_e}{\sum \dot{Q}_{in}} . \tag{67}$$

It is found that when a vacuum pump was used on the sweep side to maintain the oxygen partial pressure ~ 10^{-6} MPa, the solar-to-fuel efficiency could be as high as 40%, higher than the inert (N_2) sweep cases with the same sweep side oxygen partial pressure. In another study on a similar ceria tubular membrane reactor with inert sweep [65], the efficiency for an inert sweep case was defined as

$$\eta = \frac{\dot{n}_{CO} \cdot HHV_{CO}}{\dot{Q}_{solar}} . \tag{68}$$

Here $\dot{Q}_{solar}$ accounts for the reaction enthalpy, sensible heat of the reactants, heat losses from re-radiation through the aperture and from the wall, and the power for product separation. Heat recovery was assumed to be 95%, and the Carnot efficiency was used for thermal-to-electricity efficiency. Similar solar-fuel efficiency of around 40% was found when the operating temperature is 1600°C [65].

Other heat sources such as high temperature waste heat in glass or alumina manufacturing plants as well as nuclear heat can be used for the endothermic CO_2 reduction. Fan et al. [91] analyzed the efficiency of a $SrFeCo_{0.5}O_{3-\delta}$ membrane supported CO_2 reduction system integrated with glass furnace for heat recuperative, as shown in Figure 20. The heat utilization efficiency is defined as,

$$\eta = \frac{\sum \dot{Q}_{absorbed}}{\sum \dot{Q}_{LHV}} , \tag{69}$$

where $\sum \dot{Q}_{absorbed}$ is the heat absorbed by the glass manufacturing process, the preheat of air, the membrane reactor and the CO_2 reheat. They found that the efficiency increases from 32.9% to 65.7% by integrating the membrane reactor for CO_2 reduction.

In the efficiency studies reviewed above, the pressure drop in the membrane reactor was neglected. However, as indicated in [184, 185], the pressure drop could be a significant energy penalty in a membrane reactor depending on the membrane design, and should be

considered when evaluating the system efficiency. For example, when the total volume of the membrane reactor is fixed, larger surface-to-volume ratios can lead to higher production but larger pressure drops than smaller ratios [186]. The membrane design (e.g., channel size and length, and the frontal area), the channel numbers, the total reactor volume, the averaged oxygen fluxes, and the pressure drop are all integrated. Hence, higher-fidelity models of the membrane supported CO_2 reduction system, including sensitivity analysis, are required to correlate the membrane design, area requirement, pressure drop in the reactor and system optimization. In addition, techno-economic analysis of CO_2 reduction and fuel production, as well as life-cycle assessments should be also performed to facilitate the commercialization of this technology.
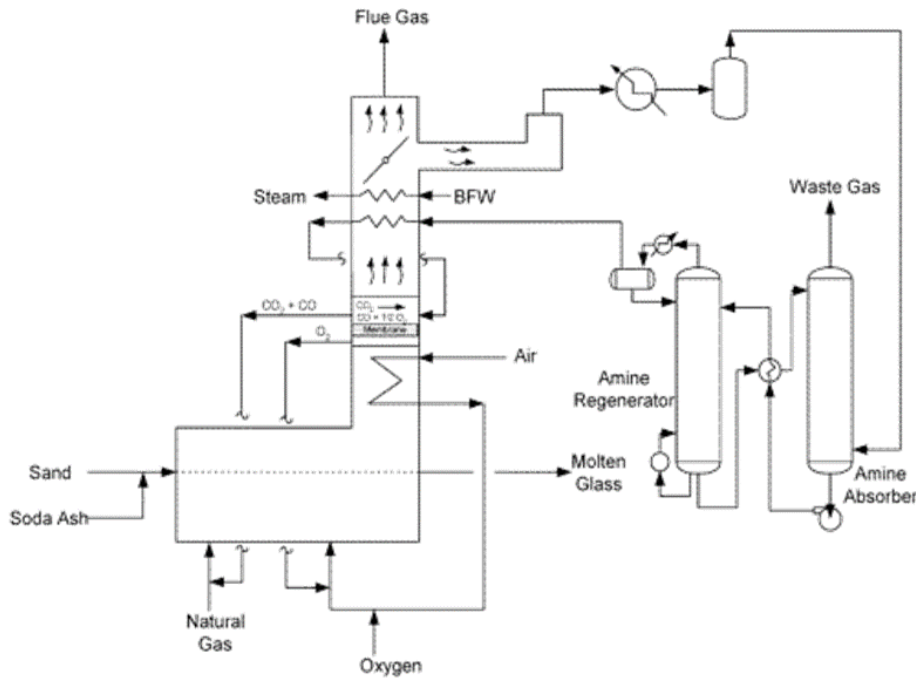
Figure 20 Schematic of a glass furnace with carbon capture and reuse (Reprinted from [91] with permission of the American Chemical Society)

6. Challenges and Future Prospect

Membrane supported CO_2 reduction is a promising technology that can be integrated into different renewable energy sources to reuse the captured CO_2. Based on this review, several challenges have been identified, from the mechanistic understanding of the process to large-scale demonstration. Advancements at different scales are needed to facilitate the commercialization of this technology.

6.1 Materials development

For membrane materials, both physical and chemical properties are important. The mechanical strength and durability of the membranes under high temperature and possibly total pressure difference for process integration is a major physical challenge. In order to decrease the oxygen diffusion barrier and the materials cost, thinner membranes are desired. However, to improve the mechanical strength and overall permeation performance, a porous support is usually added to the dense membrane. An optimal porous support should have low mass diffusion barrier, good mixed conductivity, fast reaction kinetics, high chemical stability, and good thermal compatibility.

For the chemical properties, new materials with faster kinetics and higher stability should be developed, e.g., mixed-phase membrane materials with optimum compositions and catalytic surface modification. A combination of the Ellingham diagram and other descriptors such as the basicity of the materials can help in the discovery of new materials with resistance for carbonate formation. In addition, catalytic porous support and asymmetric structures can improve gas-surface kinetics. To accelerate material development, it is important to determine kinetic parameters, e.g., conductivity and reaction rate constants from high throughput experimental measurements supported by transport models. Automation can be applied to the experimental setups to increase the efficiency and repeatability in data acquisition. Local gas atmosphere near the membrane surface should be investigated to reveal the material properties. Advanced *in situ* material characterization methods, e.g., Raman and X-ray adsorption spectroscopy, should be applied to examine the interaction between the solid materials and the gas species, and therefore reveal the reaction mechanisms, similar to those used in the study of solid oxide electrochemical cells [138]. Additionally, computational material modeling such as density functional theory (DFT) and molecular dynamics (MD) have been used for similar but different processes [187, 188]. Efforts are also needed to screen the thermodynamics properties of various oxide membrane materials such as perovskites, fluorites, spinels and Ruddlesden-Popper phases to support CO_2 reduction. Stable materials for simultaneous water splitting and CO_2 reduction can reduce the cost and complexity of fuel production.

Furthermore, the costs of all the components, i.e., the membranes, supports and catalysts are important parameters for the deployment of such membrane reactor. Hence, materials development should focus on using non-critical earth-abundant materials or decreasing the amounts of material uses in the reactor.

6.2 Reactor design and manufacturing

Physical or numerical models, incorporating fluid mechanics, reaction kinetics, heat and mass diffusion, can support the design of new reactor configurations. More studies should be carried out with both experiments and computational fluid dynamics (CFD) to determine the dependence of the species concentrations, temperature gradients, and CO_2 conversion rates on different reactor designs, such as tubular, planar and monolith reactors, and co-current flow, countercurrent flow and cross-flow configurations. With more datasets available on the reactor performance and its dependence on geometries, operating conditions and integration approaches, artificial intelligence and machine learning tools are also useful in this endeavor.

The development of advanced manufacture techniques, such as 3D printing of functional ceramic materials, high precision machining and automation show new paths for membrane fabrication (both dense and porous parts) with the optimized geometries predicted by the physical or numerical models. Hence, better performances, such as lower gas phase diffusion barrier and higher CO_2 conversion rates, can be achieved compared to the membranes fabricated with traditional methods such as press-and-sinter and extrusion. Additionally, sustainable and green manufacturing techniques are also desired to decrease the waste and carbon footprint in the entire life-cycle of the reactors. Recycle or dispose of the end-of-life reactors should be also studied to improve the sustainability.

6.3 Novel process integration and system analysis

Various processes can be integrated into a membrane reactor to support CO_2 reduction, apart from the oxygen production and syngas production (see Figure 2(a) and Table 5). Oxidation reactions that can use the oxygen stream on the sweep side will enhance the CO_2 reduction by increasing the oxygen chemical potential gradient across the membrane. Examples are methane oxidative coupling to ethylene, ethane and propane oxidative dehydrogenation, ethylene epoxidation to ethylene oxide, and biomass or coal gasification. Regardless of the scenario of carbon emission policies, integration of an important industrial process into the membrane reactor can make this CO_2 reuse technology more favorable economically for large scale applications. Another integration option is having the CO_2 capture process integrated onto the feed side to achieve capture and utilization in one-unit reactor. Demonstration of these novel processes can show the versatility of this membrane process and could potentially improve the economics of CO_2 capture and utilization.

H_2O and CO_2 co-reduction on the feed side of the reactor is also promising [189]. Syngas is produced from the co-reduction, which can be further processed into hydrocarbon fuels. When renewable energy is used as the heat source, this co-reduction

process can be viewed as a sustainable way to recycle the combustion products (H_2O and CO_2) to close the carbon loop. In this process, the competition between the water gas shift reaction and the reduction reactions on either the solid surface or in the gas phase can make the reaction mechanisms more complicated. Yet these competing pathways are similar to those in the H_2O and CO_2 co-electrolysis in solid oxide electrolysis cells [190, 191]. Much can be learned from these two emerging applications.

Furthermore, system-level simulation and techno-economic analysis are required to identify the optimal combination of membrane compositions and operating conditions for efficiency improvement and cost reduction. So far, the membrane performance has been mainly determined on the basis of CO production rate. Yet performance criteria, under which this membrane-supported CO_2 reduction technology can be profitable and widely adopted should be developed based on techno-economic analysis. Moreover, life-cycle assessment should be conducted to investigate the carbon footprint and energy storage potential of the system and their dependence on the CO_2 reduction rates and material stability. These can benefit from the knowledge on materials, kinetics and reactor designs. In turn, these macro-scale analyses can give guidance for materials development and reactor optimization with the considerations of cost and performance.

6.4 Large-scale demonstration

More demonstrations at the laboratory scale and pilot scale are needed to understand the system performance, such as uniformity of the fabricated membranes, the distribution of the catalysts and the temperature profile in the reactor. Eventually, it is important to construct pilot and industrial scale demonstrations of this membrane supported CO_2 reduction technology to translate the knowledge into practice and also gain experience and knowledge related to large-scale operations.

One promising demonstration example is to combine concentrated solar power with the membrane reactor for solar-fuels productions. Depending on the operating conditions, three different integration approaches can be adapted (shown in Figure 19). The temperature profile in the reactor, the CO_2 conversion ratio, the pressure drop inside the reactor, and the overall solar-to-fuel conversion efficiency are the important parameters to be measured.

The stability of membrane materials and catalysts under the non-ideal operating conditions, such as temperature and pressure gradients, are the challenges in large-scale demonstrations. In addition, if the system is located in the downstream of the exhausts from fossil fuel power plants, the material corrosions by H_2S and SO_2 can become a problem [192, 193]. Studies should be carried out to understand the impacts of a mixture of H_2S, SO_2, CO_2 and H_2O on the stability and performance of such membrane reactors.

In addition, when using an intermittent heat source, such as solar heat, it is necessary to understand the system response to dynamics. Due to the constraints on the thermal expansion of the ceramic materials in the membrane reactor, the reactor might need to be kept at high temperatures even when the solar energy is not available. Therefore, more flexible systems that can withstand high ramp rates in temperatures or can incorporate different heat sources when renewable heat is unavailable should be developed.

7. Conclusions

Oxygen permeable membrane supported CO_2 reduction was proposed more than 30 years ago, but it is only during the past decade that this technology has drawn more attention thanks to the interest in CO_2 reuse and solar fuels as an alternative energy storage technique. Most research has focused on improving the reduction rate and the stability of membrane materials. So far, the best performance of CO_2 reduction rate has been ~3.16 $\mu mol\ cm^{-2}\ s^{-1}$ on a 1.0 mm thick Nb_2O_5-doped $SrCo_{0.8}Fe_{0.2}O_{3-\delta}$ perovskite membrane with CO_2 feed and CH_4 sweep at 900°C for 500h of stable operation (catalysts: $La_{0.8}Sr_{0.2}MnO_{3-\delta}$/YSZ+Pd on the CO_2 side and $Sr_{0.7}Ba_{0.3}Fe_{0.9}Mo_{0.1}O_{3-\delta}$ +Ni on the sweep side) [68].

The focus of the review was to connect the knowledge in different length scales in material development, membrane design, reactor and system integration and research in different disciplines such as material science, chemical and mechanical engineering together to facilitate the development of this technology for CO_2 reuse. Much work remains to be done before large scale application can be achieved. For effective comparisons, researchers should report detail including their membrane configurations such as compositions and thickness, porous support and catalysts, porosity and the pore sizes, etc.; operating conditions such as temperature, pressure, and flow rates; and performances including CO production rates (in $\mu mol\ cm^{-2}\ s^{-1}$ instead of $mL\ cm^{-2}\ min^{-1}$ to reduce confusion regarding the conditions) and CO_2 conversion ratio. Additionally, only gas species concentrations closed to the membrane surface should be used to derive the kinetics parameters for surface reactions (measured directly using a capillary probe [119] or calculated from mass diffusion correlations). Furthermore, when using commonly used button-cell reactors, attentions should be given to the concentration distributions along the radial direction of the membrane [62], and the effect of the flow rate and reactor geometry should be carefully considered. Finally, the energy efficiency of the process should be reported. A recommended form of efficiency is based on primary energy, for instance

Vacuum pump or inert gas sweep:

$$\eta = \frac{\sum \dot{n}_{products} \cdot HHV_{products}}{\sum \dot{Q}_{sensible} + \dot{Q}_{rxn} + \sum \dot{Q}_{loss} - \sum \dot{Q}_{recuperation} + \dfrac{\sum \dot{W}}{\eta_e}} \tag{70}$$

Fuel sweep:

$$\eta = \frac{\sum \dot{n}_{products} \cdot HHV_{products}}{\sum \dot{Q}_{sensible} + \dot{Q}_{rxn} + \sum \dot{Q}_{loss} - \sum \dot{Q}_{recuperation} + \sum \dot{n}_{fuel} \cdot HHV_{fuels} + \dfrac{\sum \dot{W}}{\eta_e}} \quad (71)$$

In these expressions, the sensible and reaction heat, the heat loss and recuperation are considered. The work required includes that to overcome the pressure drop in the membrane reactor, to create the vacuum and/or to separate the inert gas and the oxygen.

Finally, this membrane supported CO_2 reduction process can be integrated with other processes to utilize the separated oxygen stream and enhance the oxygen flux. In addition to methane partial oxidation, new processes such as methane oxidative decoupling, ethane oxidative dehydrogenation, and ethylene epoxidation can be integrated into the membrane reactor, and innovative systems can be designed to increase their economic and societal benefits. Integrated CO_2 capture and conversion systems can be a new CCS technology to achieve zero or negative CO_2 emission for a sustainable future.

Reference:

[1] Lindsey R, Dahlman L. Climate Change: Global Temperature. 2018; https://www.climate.gov/news-features/understanding-climate/climate-change-global-temperature. Accessed April 17, 2019.

[2] International Energy Agency, Global Energy & CO_2 Status Report. 2018; http://www.iea.org/publications/freepublications/publication/GECO2017.pdf. Accessed April 17, 2019.

[3] The Keeling Curve. 2018; https://scripps.ucsd.edu/programs/keelingcurve/. Accessed December 6 2018.

[4] United nations conference on climate change. 2015; http://www.cop21paris.org/. Accessed December 4 2018.

[5] Jotzo F, Karplus V, Grubb M, Löschel A, Neuhoff K, Wu L, et al. China's emissions trading takes steps towards big ambitions. Nature Climate Change. 2018;8:265-7.

[6] European Commission, 2050 low-carbon economy. 2018; https://ec.europa.eu/clima/policies/strategies/2050_en. Accessed May 1, 2018.

[7] European Commission, Green Paper. A 2030 framework for climate and energy policies. 2013; https://eur-lex.europa.eu/legal-content/EN/TXT/PDF/?uri=CELEX:52013DC0169&from=EN. Accessed May 1, 2018.

[8] Ghoniem AF. Needs, resources and climate change: Clean and efficient conversion technologies. Prog Energy Combust Sci. 2011;37:15-51.

[9] Freund HJ, Roberts MW. Surface chemistry of carbon dioxide. Surf Sci Rep. 1996;25:225-73.

[10] Beller M, Centi G, Sun L. Chemistry Future: Priorities and Opportunities from the Sustainability Perspective. ChemSusChem. 2017;10:6-13.

[11] Kleij AW, North M, Urakawa A. CO_2 Catalysis. ChemSusChem. 2017;10:1036-8.

[12] Nguyen VN, Blum L. Syngas and Synfuels from H_2O and CO_2: Current Status. Chem Ing Tech. 2015;87:354-75.

[13] Aresta M. Carbon Dioxide Reduction and Uses as a Chemical Feedstock. Activation of Small Molecules. Weinheim: WILEY-VCH; 2006.

[14] Yang Y, Ajmal S, Zheng X, Zhang L. Efficient nanomaterials for harvesting clean fuels from electrochemical and photoelectrochemical CO_2 reduction. Sustainable Energy & Fuels. 2018;2:510-37.

[15] Chen C-Y, Yeh K-L, Aisyah R, Lee D-J, Chang J-S. Cultivation, photobioreactor design and harvesting of microalgae for biodiesel production: A critical review. Bioresour Technol. 2011;102:71-81.

[16] Sadhukhan J, Lloyd JR, Scott K, Premier GC, Yu EH, Curtis T, et al. A critical review of integration analysis of microbial electrosynthesis (MES) systems with waste biorefineries for the production of biofuel and chemical from reuse of CO_2. Renewable and Sustainable Energy Reviews. 2016;56:116-32.

[17] He J, Johnson NJJ, Huang A, Berlinguette CP. Electrocatalytic Alloys for CO_2 Reduction. ChemSusChem. 2018;11:48-57.

[18] Hernandez S, Amin Farkhondehfal M, Sastre F, Makkee M, Saracco G, Russo N. Syngas production from electrochemical reduction of CO_2: current status and prospective implementation. Green Chemistry. 2017;19:2326-46.

[19] Sheng Z, Piyush K, Ujwal Kumar T, Karthik S. A review on photocatalytic CO_2 reduction using perovskite oxide nanomaterials. Nanotechnology. 2018;29:052001.

[20] Ran J, Jaroniec M, Qiao S-Z. Cocatalysts in Semiconductor-based Photocatalytic CO_2 Reduction: Achievements, Challenges, and Opportunities. Adv Mater. 2018;30:1704649.

[21] Luo M, Yi Y, Wang S, Wang Z, Du M, Pan J, et al. Review of hydrogen production using chemical-looping technology. Renewable and Sustainable Energy Reviews. 2018;81:3186-214.

[22] Zhang C, Sunarso J, Liu S. Designing CO_2-resistant oxygen-selective mixed ionic-electronic conducting membranes: guidelines, recent advances, and forward directions. Chem Soc Rev. 2017;46:2941-3005.

[23] Rastogi RP, Pandey A, Larroche C, Madamwar D. Algal Green Energy – R&D and technological perspectives for biodiesel production. Renewable and Sustainable Energy Reviews. 2018;82:2946-69.

[24] Snoeckx R, Bogaerts A. Plasma technology - a novel solution for CO_2 conversion? Chem Soc Rev. 2017;46:5805-63.

[25] Kondratenko EV, Mul G, Baltrusaitis J, Larrazabal GO, Perez-Ramirez J. Status and perspectives of CO_2 conversion into fuels and chemicals by catalytic, photocatalytic and electrocatalytic processes. Energy Environ Sci. 2013;6:3112-35.

[26] Nigara Y, Cales B. Production of Carbon Monoxide by Direct Thermal Splitting of Carbon Dioxide at High Temperature. Bull Chem Soc Jpn. 1986;59:1997-2002.

[27] Jiang Q, Chen Z, Tong J, Yang M, Jiang Z, Li C. Direct thermolysis of CO_2 into CO and O_2. Chem Commun. 2017;53:1188-91.

[28] Zhang HL, Baeyens J, Degrève J, Cáceres G. Concentrated solar power plants: Review and design methodology. Renewable and Sustainable Energy Reviews. 2013;22:466-81.

[29] Traynor AJ, Jensen RJ. Direct solar reduction of CO_2 to fuel: First prototype results. Ind Eng Chem Res. 2002;41:1935-9.

[30] Goodwin D, Malaya N, Moffat H, Speth R. Cantera: An object-oriented software toolkit for chemical kinetics, thermodynamics, and transport processes. 2013; https://code.google.com/p/cantera/. Accessed December 5, 2018.

[31] Smith GP, Golden DM, Frenklach M, Moriarty NW, Eiteneer B, Goldenberg M, et al. GRI-Mech 3.0. http://www.me.berkeley.edu/gri_mech/. Accessed December 5, 2018.

[32] Price RJ, Morse DA, Hardy SL, Fletcher TH, Hill SC, Jensen RJ. Modeling the direct solar conversion of CO_2 to CO and O_2. Ind Eng Chem Res. 2004;43:2446-53.

[33] Baykara SZ. Experimental solar water thermolysis. Int J Hydrogen Energy. 2004;29:1459-69.

[34] Lede J, Lapicque F, Villermaux J, Cales B, Ounalli A, Baumard JF, et al. Production of hydrogen by direct thermal decomposition of water: Preliminary investigations. Int J Hydrogen Energy. 1982;7:939-50.

[35] Jellinek HHG, Kachi H. The catalytic thermal decomposition of water and the production of hydrogen. Int J Hydrogen Energy. 1984;9:677-88.

[36] Kogan A. Direct solar thermal splitting of water and on-site separation of the products—II. Experimental feasibility study. Int J Hydrogen Energy. 1998;23:89-98.

[37] Chueh WC, Falter C, Abbott M, Scipio D, Furler P, Haile SM, et al. High-Flux Solar-Driven Thermochemical Dissociation of CO_2 and H_2O Using Nonstoichiometric Ceria. Science. 2010;330:1797-801.

[38] Venstrom LJ, Petkovich N, Rudisill S, Stein A, Davidson JH. The Effects of Morphology on the Oxidation of Ceria by Water and Carbon Dioxide. Journal of Solar Energy Engineering. 2011;134:011005--8.

[39] Zhao Z, Uddi M, Tsvetkov N, Yildiz B, Ghoniem AF. Enhanced intermediate-temperature CO_2 splitting using nonstoichiometric ceria and ceria-zirconia. PCCP. 2017;19:25774-85.

[40] Gálvez ME, Loutzenhiser PG, Hischier I, Steinfeld A. CO_2 Splitting via Two-Step Solar Thermochemical Cycles with Zn/ZnO and FeO/Fe_3O_4 Redox Reactions: Thermodynamic Analysis. Energy & Fuels. 2008;22:3544-50.

[41] Loutzenhiser PG, Gálvez ME, Hischier I, Stamatiou A, Frei A, Steinfeld A. CO_2 Splitting via Two-Step Solar Thermochemical Cycles with Zn/ZnO and FeO/Fe_3O_4 Redox Reactions II: Kinetic Analysis. Energy & Fuels. 2009;23:2832-9.

[42] Zhang J, Haribal V, Li F. Perovskite nanocomposites as effective CO_2-splitting agents in a cyclic redox scheme. Science Advances. 2017;3.

[43] Bork AH, Kubicek M, Struzik M, Rupp JLM. Perovskite $La_{0.6}Sr_{0.4}Cr_{1-x}Co_xO_{3-\delta}$ solid solutions for solar-thermochemical fuel production: strategies to lower the operation temperature. J Mater Chem A. 2015;3:15546-57.

[44] Zhai S, Rojas J, Ahlborg N, Lim K, Toney MF, Jin H, et al. The use of poly-cation oxides to lower the temperature of two-step thermochemical water splitting. Energy Environ Sci. 2018;11:2172-8.

[45] Cooper T, Scheffe JR, Galvez ME, Jacot R, Patzke G, Steinfeld A. Lanthanum Manganite Perovskites with Ca/Sr A‐site and Al B‐site Doping as Effective Oxygen Exchange Materials for Solar Thermochemical Fuel Production. Energy Technology. 2015;3:1130-42.

[46] Emery AA, Saal JE, Kirklin S, Hegde VI, Wolverton C. High-Throughput Computational Screening of Perovskites for Thermochemical Water Splitting Applications. Chem Mater. 2016;28:5621-34.

[47] Meredig B, Wolverton C. First-principles thermodynamic framework for the evaluation of thermochemical H_2O- or CO_2-splitting materials. Phys Rev B. 2009;80:245119.

[48] Zhao Z, Uddi M, Tsvetkov N, Yildiz B, Ghoniem AF. Redox Kinetics Study of Fuel Reduced Ceria for Chemical-Looping Water Splitting. The Journal of Physical Chemistry C. 2016;120:16271-89.

[49] Jung J, Gamwo IK. Multiphase CFD-based models for chemical looping combustion process: Fuel reactor modeling. Powder Technol. 2008;183:401-9.

[50] Zhao Z, Chen T, Ghoniem AF. Rotary Bed Reactor for Chemical-Looping Combustion with Carbon Capture. Part 1: Reactor Design and Model Development. Energy & Fuels. 2013;27:327-43.

[51] Zhao Z, Chen T, Ghoniem AF. Rotary Bed Reactor for Chemical-Looping Combustion with Carbon Capture. Part 2: Base Case and Sensitivity Analysis. Energy & Fuels. 2013;27:344-59.

[52] Zhao Z, Uddi M, Tsvetkov N, Yildiz B, Ghoniem AF. Redox Kinetics and Nonstoichiometry of $Ce_{0.5}Zr_{0.5}O_{2-\delta}$ for Water Splitting and Hydrogen Production. The Journal of Physical Chemistry C. 2017;121:11055-68.

[53] Zhao ZL, Uddi M, Tsvetkov N, Yildiz B, Ghoniem AF. Redox Kinetics Study of Fuel Reduced Ceria for Chemical-Looping Water Splitting. Journal of Physical Chemistry C. 2016;120:16271-89.

[54] Sunarso J, Baumann S, Serra JM, Meulenberg WA, Liu S, Lin YS, et al. Mixed ionic–electronic conducting (MIEC) ceramic-based membranes for oxygen separation. J Membr Sci. 2008;320:13-41.

[55] Li W, Zhu X, Cao Z, Wang W, Yang W. Mixed ionic-electronic conducting (MIEC) membranes for hydrogen production from water splitting. Int J Hydrogen Energy. 2015;40:3452-61.

[56] Thursfield A, Murugan A, Franca R, Metcalfe IS. Chemical looping and oxygen permeable ceramic membranes for hydrogen production – a review. Energy Environ Sci. 2012;5:7421 - 59.

[57] Cales B, Baumard JF. Oxygen semipermeability and electronic conductivity in calcia-stabilized zirconia. J Mater Sci. 1982;17:3243-8.

[58] Wu XY, Ghoniem AF. Hydrogen‐assisted Carbon Dioxide Thermochemical Reduction on $La_{0.9}Ca_{0.1}FeO_{3-\delta}$ Membranes: A Kinetics Study. ChemSusChem. 2018;11:483-93.

[59] Wu X-Y, Ghoniem AF, Uddi M. Enhancing co-production of H_2 and syngas via water splitting and POM on surface-modified oxygen permeable membranes. AlChE J. 2016;62:4427-35.

[60] Dimitrakopoulos G, Ghoniem AF. A two-step surface exchange mechanism and detailed defect transport to model oxygen permeation through the La0.9Ca0.1FeO3−δmixed-conductor. J Membr Sci. 2016;510:209-19.

[61] Iloeje C, Zhao Z, Ghoniem AF. Analysis of thermally coupled chemical looping combustion-based power plants with carbon capture. Int J Greenh Gas Control. 2015;35:56-70.

[62] Gozálvez-Zafrilla JM, Santafé-Moros A, Escolástico S, Serra JM. Fluid dynamic modeling of oxygen permeation through mixed ionic–electronic conducting membranes. J Membr Sci. 2011;378:290-300.

[63] Marxer D, Furler P, Takacs M, Steinfeld A. Solar thermochemical splitting of CO_2 into separate streams of CO and O_2 with high selectivity, stability, conversion, and efficiency. Energy Environ Sci. 2017;10:1142-9.

[64] Ahmed P, Habib MA, Ben-Mansour R, Kirchen P, Ghoniem AF. CFD (computational fluid dynamics) analysis of a novel reactor design using ion transport membranes for oxy-fuel combustion. Energy. 2014;77:932-44.

[65] Tou M, Michalsky R, Steinfeld A. Solar-Driven Thermochemical Splitting of CO_2 and In Situ Separation of CO and O_2 across a Ceria Redox Membrane Reactor. Joule. 2017;1:146-54.

[66] Takamura H. MIEC Materials. In: Kreysa G, Ota K-i, Savinell RF, editors. Encyclopedia of Applied Electrochemistry. New York, NY: Springer New York; 2014. p. 1297-300.

[67] Zhu X, Yang W. Mixed Conducting Ceramic Membranes: Fundamentals, Materials and Applications. Berlin: Springer-Verlag GmbH Germany; 2017.

[68] Zhang K, Zhang G, Liu Z, Zhu J, Zhu N, Jin W. Enhanced stability of membrane reactor for thermal decomposition of CO_2 via porous-dense-porous triple-layer composite membrane. J Membr Sci. 2014;471:9-15.

[69] Jin W, Zhang C, Chang X, Fan Y, Xing W, Xu N. Efficient catalytic decomposition of CO_2 to CO and O_2 over Pd/mixed-conducting oxide catalyst in an oxygen-permeable membrane reactor. Environmental Science & Technology. 2008;42:3064-8.

[70] Zhang C, Jin W, Yang C, Xu N. Decomposition of CO_2 coupled with POM in a thin tubular oxygen-permeable membrane reactor. Catal Today. 2009;148:298-302.

[71] Wu X-Y, Ghoniem AF. CO_2 reduction and methane partial oxidation on surface catalyzed $La_{0.9}Ca_{0.1}FeO_{3-\delta}$ oxygen ion transport membranes. Proceedings of The Combustion Institute. 2019;37:5517 - 24.

[72] Zhang K, Liu L, Sunarso J, Yu H, Pareek V, Liu S. Highly Stable External Short-Circuit-Assisted Oxygen Ionic Transport Membrane Reactor for Carbon Dioxide Reduction Coupled with Methane Partial Oxidation. Energy & Fuels. 2013;28:349-55.

[73] Michalsky R, Neuhaus D, Steinfeld A. Carbon Dioxide Reforming of Methane using an Isothermal Redox Membrane Reactor. Energy Technology. 2015;3:784-9.

[74] Kim DJ. Lattice Parameters, Ionic Conductivities, and Solubility Limits in Fluorite‐Structure MO_2 Oxide [M = Hf^{4+}, Zr^{4+}, Ce^{4+}, Th^{4+}, U^{4+}] Solid Solutions. J Am Ceram Soc. 1989;72:1415-21.

[75] Garcia-Fayos J, Balaguer M, Baumann S, Serra JM. Dual-phase membrane based on $LaCo_{0.2}Ni_{0.4}Fe_{0.4}O_{3-x}$-$Ce_{0.8}Gd_{0.2}O_{2-x}$ composition for oxygen permeation under CO_2/SO_2-rich gas environments. J Membr Sci. 2018;548:117-24.

[76] Liu Y, Tan X, Li K. Mixed Conducting Ceramics for Catalytic Membrane Processing. Cat Rev. 2006;48:145-98.

[77] Gilev AR, Kiselev EA, Cherepanov VA. Oxygen transport phenomena in $(La,Sr)_2(Ni,Fe)O_4$ materials. J Mater Chem A. 2018;6:5304-12.

[78] Xue J, Li J, Zhuang L, Chen L, Feldhoff A, Wang H. Anion doping CO_2-stable oxygen permeable membranes for syngas production. Chem Eng J. 2018;347:84-90.

[79] Xiong Y-P, Kishimoto H, Yamaji K, Yoshinaga M, Horita T, Brito ME, et al. Electronic conductivity of pure ceria. Solid State Ionics. 2011;192:476-9.

[80] Itoh N, Sanchez MA, Xu W-C, Haraya K, Hongo M. Application of a membrane reactor system to thermal decomposition of CO_2. J Membr Sci. 1993;77:245-53.

[81] Sunarso J, Hashim SS, Zhu N, Zhou W. Perovskite oxides applications in high temperature oxygen separation, solid oxide fuel cell and membrane reactor: A review. Prog Energy Combust Sci. 2017;61:57-77.

[82] Jin W, Zhang C, Zhang P, Fan Y, Xu N. Thermal decomposition of carbon dioxide coupled with POM in a membrane reactor. AIChE J. 2006;52:2545-50.

[83] Zhang C, Chang X, Fan Y, Jin W, Xu N. Improving Performance of a Dense Membrane Reactor for Thermal Decomposition of CO2 via Surface Modification. Ind Eng Chem Res. 2007;46:2000-5.

[84] Jiang H, Wang H, Werth S, Schiestel T, Caro J. Simultaneous Production of Hydrogen and Synthesis Gas by Combining Water Splitting with Partial Oxidation of Methane in a Hollow-Fiber Membrane Reactor. Angew Chem Int Ed. 2008;47:9341-4.

[85] Efimov K, Klande T, Juditzki N, Feldhoff A. Ca-containing CO_2-tolerant perovskite materials for oxygen separation. J Membr Sci. 2012;389:205-15.

[86] Zhang C, Meng X, Sunarso J, Liu L, Xu R, Shao Z, et al. Oxygen permeation behavior through $Ce_{0.9}Gd_{0.1}O_{2-\delta}$ membranes electronically short-circuited by dual-phase $Ce_{0.9}Gd_{0.1}O_{2-\delta}$-Ag decoration. J Mater Chem A. 2015;3:19033-41.

[87] Kniep J, Yin Q, Kumakiri I, Lin YS. Electrical conductivity and oxygen permeation properties of $SrCoFeOx$ membranes. Solid State Ionics. 2010;180:1633-9.

[88] Chen T, Zhao H, Xie Z, Wang J, Lu Y, Xu N. $Ce_{0.8}Sm_{0.2}O_{2-\delta}$–$PrBaCo_2O_{5+\delta}$ dual-phase membrane: Novel preparation and improved oxygen permeability. J Power Sources. 2013;223:289-92.

[89] Lee TH, Park CY, Dorris SE, Balachandran U. Hydrogen Production by Steam Dissociation using Oxygen Transport Membranes. ECS Trans. 2008;13:379-84.

[90] Balachandran U, Lee T, Dorris S. Hydrogen production by water dissociation using mixed conducting dense ceramic membranes. Int J Hydrogen Energy. 2007;32:451-6.

[91] Fan Y, Ren J-y, Onstot W, Pasale J, Tsotsis TT, Egolfopoulos FN. Reactor and Technical Feasibility Aspects of a CO_2 Decomposition-Based Power Generation Cycle, Utilizing a High-Temperature Membrane Reactor. Ind Eng Chem Res. 2003;42:2618-26.

[92] Cousin P, Ross RA. Preparation of mixed oxides: a review. Materials Science and Engineering: A. 1990;130:119-25.

[93] Kammler HK, Mädler L, Pratsinis SE. Flame Synthesis of Nanoparticles. Chemical Engineering & Technology. 2001;24:583-96.

[94] Kharton VV, Marques FMB. Mixed ionic–electronic conductors: effects of ceramic microstructure on transport properties. Curr Opin Solid State Mater Sci. 2002;6:261-9.

[95] Saher S, Meffert M, Störmer H, Gerthsen D, Bouwmeester HJM. Grain-size dependence of the deterioration of oxygen transport for pure and 3 mol% Zr-doped $Ba_{0.5}Sr_{0.5}Co_{0.8}Fe_{0.2}O_{3-\delta}$ induced by thermal annealing. J Mater Chem A. 2017;5:4982-90.

[96] Neagu D, Oh T-S, Miller DN, Menard H, Bukhari SM, Gamble SR, et al. Nano-socketed nickel particles with enhanced coking resistance grown in situ by redox exsolution. Nat Commun. 2015;6:8120.

[97] Naito H, Arashi H. Hydrogen production from direct water splitting at high temperatures using a ZrO_2-TiO_2-Y_2O_3 membrane. Solid State Ionics. 1995;79:366-70.

[98] Park CY, Lee TH, Dorris SE, Balachandran U. Hydrogen production from fossil and renewable sources using an oxygen transport membrane. Int J Hydrogen Energy. 2010;35:4103-10.

[99] Gu X, Jin W, Chen C, Xu N, Shi J, Ma YH. YSZ-$SrCo_{0.4}Fe_{0.6}O_{3-\delta}$ membranes for the partial oxidation of methane to syngas. AlChE J. 2002;48:2051-60.

[100] Schmalzried H. Solid-State Reactions. Angewandte Chemie International Edition in English. 1963;2:251-4.

[101] Jeon S-Y, Im H-N, Singh B, Hwang J-H, Song S-J. A thermodynamically stable La2NiO4+δ/ Gd0.1Ce0.9O1.95 bilayer oxygen transport membrane in membrane-assisted water splitting for hydrogen production. Ceram Int. 2013;39:3893-9.

[102] Jeon SY, Choi MB, Im HN, Hwang JH, Song SJ. Oxygen ionic conductivity of $La_2NiO_{4+\delta}$ via interstitial oxygen defect. J Phys Chem Solids. 2012;73:656-60.

[103] Li S, Cheng J, Gan Y, Li P, Zhang X, Wang Y. Enhancing the oxygen permeation rate of $Ba_{0.5}Sr_{0.5}Co_{0.8}Fe_{0.2}O_{3-\delta}$ membranes by surface loading Co_3O_4 nanorod catalysts. Surf Coat Technol. 2015;276:47-54.

[104] Rotureau D, Viricelle JP, Pijolat C, Caillol N, Pijolat M. Development of a planar SOFC device using screen-printing technology. J Eur Ceram Soc. 2005;25:2633-6.

[105] Deville S. Freeze-Casting of Porous Ceramics: A Review of Current Achievements and Issues. Adv Eng Mater. 2008;10:155-69.

[106] Schulze-Küppers F, Unije UV, Blank H, Balaguer M, Baumann S, Mücke R, et al. Comparison of freeze-dried and tape-cast support microstructure on high-flux oxygen transport membrane performance. J Membr Sci. 2018;564:218-26.

[107] Chi Y, Li T, Wang B, Wu Z, Li K. Morphology, performance and stability of multi-bore capillary $La_{0.6}Sr_{0.4}Co_{0.2}Fe_{0.8}O_{3-\delta}$ oxygen transport membranes. J Membr Sci. 2017;529:224-33.

[108] Froment GF, Wilde JD, Bischoff KB. Chemical Reactor Analysis and Design, 3rd ed. Hoboken, N.J. : Wiley; 2011.

[109] Rachadel PL, Motuzas J, Machado RAF, Hotza D, Diniz da Costa JC. Influence of porous structures on O_2 flux of BSCF asymmetric membranes. Sep Purif Technol. 2017;175:164-9.

[110] Balachandran U, Lee TH, Wang S, Dorris SE. Use of mixed conducting membranes to produce hydrogen by water dissociation. Int J Hydrogen Energy. 2004;29:291-6.

[111] Park CY, Lee TH, Dorris SE, Lu Y, Balachandran U. Oxygen permeation and coal-gas-assisted hydrogen production using oxygen transport membranes. Int J Hydrogen Energy. 2011;36:9345-54.

[112] Evdou A, Nalbandian L, Zaspalis V. Perovskite membrane reactor for continuous and isothermal redox hydrogen production from the dissociation of water. J Membr Sci. 2008;325:704-11.

[113] Balachandran U, Dusek JT, Mieville RL, Poeppel RB, Kleefisch MS, Pei S, et al. Dense ceramic membranes for partial oxidation of methane to syngas. Applied Catalysis A: General. 1995;133:19-29.

[114] Zhu N, Dong X, Liu Z, Zhang G, Jin W, Xu N. Toward highly-effective and sustainable hydrogen production: bio-ethanol oxidative steam reforming coupled with water splitting in a thin tubular membrane reactor. Chem Commun. 2012;48:7137-9.

[115] Schiestel T, Kilgus M, Peter S, Caspary KJ, Wang H, Caro J. Hollow fibre perovskite membranes for oxygen separation. J Membr Sci. 2005;258:1-4.

[116] Park CY, Lee TH, Dorris SE, Balachandran U. $La_{0.7}Sr_{0.3}Cu_{0.2}Fe_{0.8}O_{3-x}$ as Oxygen Transport Membrane for Producing Hydrogen via Water Splitting. ECS Trans. 2008;13:393-403.

[117] Hunt A, Dimitrakopoulos G, Ghoniem AF. Surface oxygen vacancy and oxygen permeation flux limits of perovskite ion transport membranes. J Membr Sci. 2015;489:248-57.

[118] Hunt A, Dimitrakopoulos G, Kirchen P, Ghoniem AF. Measuring the oxygen profile and permeation flux across an ion transport membrane and the development and validation of a multistep surface exchange model. J Membr Sci. 2014;468:62-72.

[119] Kirchen P, Apo DJ, Hunt A, Ghoniem AF. A novel ion transport membrane reactor for fundamental investigations of oxygen permeation and oxy-combustion under reactive flow conditions. Proceedings of the Combustion Institute. 2013;34:3463-70.

[120] Kovalevsky AV, Yaremchenko AA, Kolotygin VA, Snijkers FMM, Kharton VV, Buekenhoudt A, et al. Oxygen permeability and stability of asymmetric multilayer $Ba_{0.5}Sr_{0.5}Co_{0.8}Fe_{0.2}O_{3-\delta}$ ceramic membranes. Solid State Ionics. 2011;192:677-81.

[121] Tong J, Yang W, Zhu B, Cai R. Investigation of ideal zirconium-doped perovskite-type ceramic membrane materials for oxygen separation. J Membr Sci. 2002;203:175-89.

[122] Yi J, Weirich TE, Schroeder M. CO_2 corrosion and recovery of perovskite-type $BaCo_{1-x-y}Fe_xNb_yO_{3-\delta}$ membranes. J Membr Sci. 2013;437:49-56.

[123] Yang Z, Liu Y, Zhu T, Chen Y, Han M, Jin C. Mechanism analysis of CO_2 corrosion on $Ba_{0.9}Co_{0.7}Fe_{0.2}Nb_{0.1}O_{3-\delta}$ cathode. Int J Hydrogen Energy. 2016;41:1997 - 2001.

[124] Yi J, Schroeder M, Weirich T, Mayer J. Behavior of $Ba(Co, Fe, Nb)O_{3-\delta}$ Perovskite in CO_2-Containing Atmospheres: Degradation Mechanism and Materials Design. Chem Mater. 2010;22:6246-53.

[125] Polfus JM, Yildiz B, Tuller HL, Bredesen R. Adsorption of CO_2 and Facile Carbonate Formation on $BaZrO_3$ Surfaces. The Journal of Physical Chemistry C. 2018;122:307-14.

[126] Chen W, Chen C-s, Bouwmeester HJM, Nijmeijer A, Winnubst L. Oxygen-selective membranes integrated with oxy-fuel combustion. J Membr Sci. 2014;463:166-72.

[127] Cordischi D, Indovina V. Electron donor sites and acid-base properties of oxide surfaces, as studied by electron spin resonance spectroscopy. Journal of the Chemical Society, Faraday Transactions 1: Physical Chemistry in Condensed Phases. 1976;72:2341-7.

[128] Sugunan S, Meera V. Acid-base properties and catalytic activity of ABO_3 (perovskite-type) oxides consisting of rare earth and 3d transition metals. React Kinet Catal Lett. 1997;62:327-32.

79

[129] Polo-Garzon F, Wu Z. Acid–base catalysis over perovskites: a review. J Mater Chem A. 2018;6:2877-94.

[130] Zeng Q, Zuo Y-b, Fan C-g, Chen C-s. CO_2-tolerant oxygen separation membranes targeting CO_2 capture application. J Membr Sci. 2009;335:140-4.

[131] Maier J. Acid–Base Centers and Acid–Base Scales in Ionic Solids. Chemistry – A European Journal. 2001;7:4762-70.

[132] Coluccia S, Garrone E, Guglielminotti E, Zecchina A. Infrared study of carbon monoxide adsorption on calcium and strontium oxides. Journal of the Chemical Society, Faraday Transactions 1: Physical Chemistry in Condensed Phases. 1981;77:1063-73.

[133] Polo-Garzon F, Yang S-Z, Fung V, Foo GS, Bickel EE, Chisholm MF, et al. Controlling Reaction Selectivity through the Surface Termination of Perovskite Catalysts. Angew Chem. 2017;129:9952-6.

[134] Hammami R, Batis H, Minot C. Combined experimental and theoretical investigation of the CO_2 adsorption on $LaMnO_{3+y}$ perovskite oxide. Surf Sci. 2009;603:3057-67.

[135] Cheng Z, Liu M. Characterization of sulfur poisoning of Ni–YSZ anodes for solid oxide fuel cells using in situ Raman microspectroscopy. Solid State Ionics. 2007;178:925-35.

[136] Hardy JS, Templeton JW, Edwards DJ, Lu Z, Stevenson JW. Lattice expansion of LSCF-6428 cathodes measured by in situ XRD during SOFC operation. J Power Sources. 2012;198:76-82.

[137] Benck JD, Rettenwander D, Jackson A, Young D, Chiang Y-M. Apparatus for operando x-ray diffraction of fuel electrodes in high temperature solid oxide electrochemical cells. Rev Sci Instrum. 2019;90:023910.

[138] Jouttijärvi S, Asghar MI, Lund PD. Microscopic techniques for analysis of ceramic fuel cells. Wiley Interdisciplinary Reviews: Energy and Environment. 2018;7:e299.

[139] Liu M, Lynch ME, Blinn K, Alamgir FM, Choi Y. Rational SOFC material design: new advances and tools. Mater Today. 2011;14:534-46.

[140] Xu SJ, Thomson WJ. Oxygen permeation rates through ion-conducting perovskite membranes. Chem Eng Sci. 1999;54:3839-50.

[141] Dimitrakopoulos G, Ghoniem AF. Developing a multistep surface reaction mechanism to model the impact of H_2 and CO on the performance and defect chemistry of $La_{0.9}Ca_{0.1}FeO_{3-\delta}$ mixed-conductors. J Membr Sci. 2017;529:114-32.

[142] Geary TC, Adler SB. Oxygen nonstoichiometry and defect chemistry of the mixed conductor $La_{0.9}Ca_{0.1}FeO_{3-\delta}$ at low oxygen partial pressure. Solid State Ionics. 2013;253:88-93.

[143] ten Elshof JE, Bouwmeester HJM, Verweij H. Oxidative coupling of methane in a mixed-conducting perovskite membrane reactor. Applied Catalysis A: General. 1995;130:195-212.

[144] Bouwmeester HJM, Den Otter MW, Boukamp BA. Oxygen transport in $La_{0.6}Sr_{0.4}Co_{1-y}Fe_yO_{3-\delta}$. J Solid State Electrochem. 2004;8:599-605.

[145] Wang S, Kobayashi T, Dokiya M, Hashimoto T. Electrical and Ionic Conductivity of Gd‐Doped Ceria. J Electrochem Soc. 2000;147:3606-9.

[146] Katsuki M, Wang S, Yasumoto K, Dokiya M. The oxygen transport in Gd-doped ceria. Solid State Ionics. 2002;154–155:589-95.

[147] Stevenson JW, Armstrong TR, Carneim RD, Pederson LR, Weber WJ. Electrochemical Properties of Mixed Conducting Perovskites $La_{1-x}M_xCo_{1-y}Fe_yO_{3-\delta}$ (M = Sr, Ba, Ca). J Electrochem Soc. 1996;143:2722-9.

[148] Park CY, Azzarello FV, Jacobson AJ. The oxygen non-stoichiometry and electrical conductivity of $La_{0.7}Sr_{0.3}Cu_{0.2}Fe_{0.8}O_{3-\delta}$. J Mater Chem. 2006;16:3624-8.

[149] Wackerl J, Koppitz T, Peck D-H, Woo S-K, Markus T. Correlation of thermal properties and electrical conductivity of $La_{0.7}Sr_{0.3}Cu_{0.2}Fe_{0.8}O_{3-\delta}$ material for solid oxide fuel cells. J Appl Electrochem. 2009;39:1243-9.

[150] Tai LW, Nasrallah MM, Anderson HU, Sparlin DM, Sehlin SR. Structure and electrical properties of $La_{1-x}Sr_xCo_{1-y}Fe_yO_3$. Part 1. The system $La_{0.8}Sr_{0.2}Co_{1-y}Fe_yO_3$. Solid State Ionics. 1995;76:259-71.

[151] Ma B, Balachandran U, Park JH, Segre CU. Electrical Transport Properties and Defect Structure of $SrFeCo_{0.5}O_x$. J Electrochem Soc. 1996;143:1736-44.

[152] Wang H, Gopalan S, Pal UB. Hydrogen generation and separation using $Gd_{0.2}Ce_{0.8}O_{1.9-\delta}$–$Gd_{0.08}Sr_{0.88}Ti_{0.95}Al_{0.05}O_{3\pm\delta}$ mixed ionic and electronic conducting membranes. Electrochim Acta. 2011;56:6989-96.

[153] Merkle R, Maier J. How Is Oxygen Incorporated into Oxides? A Comprehensive Kinetic Study of a Simple Solid-State Reaction with SrTiO3 as a Model Material. Angew Chem Int Ed. 2008;47:3874-94.

[154] Benson SJ, Waller D, Kilner JA. Degradation of $La_{0.6}Sr_{0.4}Fe_{0.8}Co_{0.2}O_{3-\delta}$ in carbon dioxide and water atmospheres. J Electrochem Soc. 1999;146:1305-9.

[155] Argirusis C, Voigts F, Datta P, Grosse-Brauckmann J, Maus-Friedrichs W. Oxygen incorporation into strontium titanate single crystals from CO2 dissociation. PCCP. 2009;11:3152-7.

[156] Feng ZA, Machala ML, Chueh WC. Surface electrochemistry of CO_2 reduction and CO oxidation on Sm-doped CeO_{2-x}: coupling between Ce^{3+} and carbonate adsorbates. PCCP. 2015;17:12273-81.

[157] Solis BH, Cui Y, Weng X, Seifert J, Schauermann S, Sauer J, et al. Initial stages of CO_2 adsorption on CaO: a combined experimental and computational study. PCCP. 2017;19:4231-42.

[158] Corberán VC, Tejuca LG, Bell AT. Surface reactivity of reduced $LaFeO_3$ as studied by TPD and IR spectroscopies of CO, CO_2 and H_2. J Mater Sci. 1989;24:4437-42.

[159] Voigts F, Argirusis C, Maus-Friedrichs W. The interaction of CO_2 and CO with Fe-doped $SrTiO_3$(100) surfaces. Surf Interface Anal. 2012;44:301-7.

[160] Shi Y, Luo Y, Cai N, Qian J, Wang S, Li W, et al. Experimental characterization and modeling of the electrochemical reduction of CO_2 in solid oxide electrolysis cells. Electrochim Acta. 2013;88:644-53.

[161] Li W, Shi Y, Luo Y, Wang Y, Cai N. Carbon deposition on patterned nickel/yttria stabilized zirconia electrodes for solid oxide fuel cell/solid oxide electrolysis cell modes. J Power Sources. 2015;276:26-31.

[162] Li C, Chew JJ, Mahmoud A, Liu S, Sunarso J. Modelling of oxygen transport through mixed ionic-electronic conducting (MIEC) ceramic-based membranes: An overview. J Membr Sci. 2018;567:228-60.

[163] Deen WM. Analysis of Transport Phenomena, Second Edition. New York: Oxford University Press; 2011.

[164] Fuller EN, Schettler PD, Giddings JC. New method for prediction of binary gas-phase diffusion coefficients. Industrial & Engineering Chemistry. 1966;58:18-27.

[165] Li K. Mixed Conducting Ceramic Membranes for Oxygen Separation. In: Li K, editor. Ceramic Membranes for Separation and Reaction. West Sussex: John Wiley & Sons, Ltd; 2007.

[166] Gellings PJ, Bouwmeester HJM. Ion and mixed conducting oxides as catalysts. Catal Today. 1992;12:1-101.

[167] Lin Y-S, Wang W, Han J. Oxygen permeation through thin mixed-conducting solid oxide membranes. AlChE J. 1994;40:786-98.

[168] Wu XY, Chang L, Uddi M, Kirchen P, Ghoniem AF. Toward enhanced hydrogen generation from water using oxygen permeating LCF membranes. PCCP. 2015;17:10093-107.

[169] Bidrawn F, Lee S, Vohs JM, Gorte RJ. The Effect of Ca, Sr, and Ba Doping on the Ionic Conductivity and Cathode Performance of $LaFeO_3$. J Electrochem Soc. 2008;155:B660-B5.

[170] Hung M-H, Rao MVM, Tsai D-S. Microstructures and electrical properties of calcium substituted $LaFeO_3$ as SOFC cathode. Mater Chem Phys. 2007;101:297-302.

[171] Hong J, Kirchen P, Ghoniem AF. Numerical simulation of ion transport membrane reactors: Oxygen permeation and transport and fuel conversion. J Membr Sci. 2012;407-408:71-85.

[172] Pecchi G, Jiliberto MG, Buljan A, Delgado EJ. Relation between defects and catalytic activity of calcium doped $LaFeO_3$ perovskite. Solid State Ionics. 2011;187:27-32.

[173] Tan X, Li K. Modeling of air separation in a LSCF hollow-fiber membrane module. AlChE J. 2002;48:1469-77.

[174] Zhu L, Lu Y, Shen S. Solar fuel production at high temperatures using ceria as a dense membrane. Energy. 2016;104:53-63.

[175] Sheu EJ, Ghoniem AF. Receiver reactor concept and model development for a solar steam redox reformer. Solar Energy. 2016;125:339-59.

[176] Graves C, Ebbesen SD, Mogensen M, Lackner KS. Sustainable hydrocarbon fuels by recycling CO_2 and H_2O with renewable or nuclear energy. Renewable and Sustainable Energy Reviews. 2011;15:1-23.

[177] Zhu X, Sun S, Cong Y, Yang W. Operation of perovskite membrane under vacuum and elevated pressures for high-purity oxygen production. J Membr Sci. 2009;345:47-52.

[178] Engels S, Markus T, Modigell M, Singheiser L. Oxygen permeation and stability investigations on MIEC membrane materials under operating conditions for power plant processes. J Membr Sci. 2011;370:58-69.

[179] Schulz M, Pippardt U, Kiesel L, Ritter K, Kriegel R. Oxygen permeation of various archetypes of oxygen membranes based on BSCF. AlChE J. 2012;58:3195-202.

[180] Anderson LL, Armstrong PA, Broekhuis RR, Carolan MF, Chen J, Hutcheon MD, et al. Advances in ion transport membrane technology for oxygen and syngas production. Solid State Ionics. 2016;288:331-7.

[181] Kriegel R. Energy demand of oxygen membrane plants. 2014; https://www.ikts.fraunhofer.de/content/dam/ikts/abteilungen/umwelt_und_verfahrenstechnik/hochtemperaturseparation_und_katalyse/hochtemperaturmembranen_und_speicher/energie bedarf_sauerstoff-membrananlage/2013_IKTS_energy_demand_o2_membrane_plants.pdf. Accessed April 18, 2019.

[182] Li J. Praxair's oxygen transport membrane technology for syngas and power applications. 2015; https://www.netl.doe.gov/sites/default/files/event-proceedings/2015/co2captureproceedings/J-Li-Praxair-OTM-Technology.pdf. Accessed April 18, 2019.

[183] Wang H, Hao Y, Kong H. Thermodynamic study on solar thermochemical fuel production with oxygen permeation membrane reactors. International Journal of Energy Research. 2015;39:1790-9.

[184] Mancini ND, Mitsos A. Ion transport membrane reactors for oxy-combustion – Part I: intermediate-fidelity modeling. Energy. 2011;36:4701-20.

[185] Mancini ND, Gunasekaran S, Mitsos A. A Multiple-Compartment Ion-Transport-Membrane Reactive Oxygen Separator. Ind Eng Chem Res. 2012;51:7988-97.

[186] Mancini ND, Mitsos A. Ion transport membrane reactors for oxy-combustion–Part II: Analysis and comparison of alternatives. Energy. 2011;36:4721-39.

[187] Parfitt D, Kordatos A, Filippatos PP, Chroneos A. Diffusion in energy materials: Governing dynamics from atomistic modelling. Applied Physics Reviews. 2017;4:031305.

[188] Muñoz-García AB, Ritzmann AM, Pavone M, Keith JA, Carter EA. Oxygen Transport in Perovskite-Type Solid Oxide Fuel Cell Materials: Insights from Quantum Mechanics. Acc Chem Res. 2014;47:3340-8.

[189] Tou M, Jin J, Hao Y, Steinfeld A, Michalsky R. Solar-driven co-thermolysis of CO_2 and H_2O and in-situ oxygen removal across a non-stoichiometric ceria membrane. Reaction Chemistry & Engineering. 2019.

[190] Gaudillere C, Navarrete L, Serra JM. Syngas production at intermediate temperature through H_2O and CO_2 electrolysis with a Cu-based solid oxide electrolyzer cell. Int J Hydrogen Energy. 2014;39:3047-54.

[191] Graves C, Ebbesen SD, Mogensen M. Co-electrolysis of CO_2 and H_2O in solid oxide cells: Performance and durability. Solid State Ionics. 2011;192:398-403.

[192] Li W, Cao Z, Cai L, Zhang L, Zhu X, Yang W. H_2S-tolerant oxygen-permeable ceramic membranes for hydrogen separation with a performance comparable to those of palladium-based membranes. Energy Environ Sci. 2017;10:101-6.

[193] Cheng S, Søgaard M, Han L, Zhang W, Chen M, Kaiser A, et al. A novel CO_2- and SO_2-tolerant dual phase composite membrane for oxygen separation. Chem Commun. 2015;51:7140-3.